



Review

Recent Progress in the Design, Characterisation and Application of LaAlO₃- and LaGaO₃-Based Solid Oxide Fuel Cell Electrolytes

Elena Filonova ^{1,*} and Dmitry Medvedev ^{2,3,*}

¹ Department of Physical and Inorganic Chemistry, Institute of Natural Sciences and Mathematics, Ural Federal University, 620002 Ekaterinburg, Russia

² Laboratory of Electrochemical Devices Based on Solid Oxide Proton Electrolytes, Institute of High Temperature Electrochemistry, 620660 Ekaterinburg, Russia

³ Hydrogen Energy Laboratory, Ural Federal University, 620002 Ekaterinburg, Russia

* Correspondence: elena.filonova@urfu.ru (E.F.); dmitrymedv@mail.ru (D.M.)

Abstract: Solid oxide fuel cells (SOFCs) are efficient electrochemical devices that allow for the direct conversion of fuels (their chemical energy) into electricity. Although conventional SOFCs based on YSZ electrolytes are widely used from laboratory to commercial scales, the development of alternative ion-conducting electrolytes is of great importance for improving SOFC performance at reduced operation temperatures. The review summarizes the basic information on two representative families of oxygen-conducting electrolytes: doped lanthanum aluminates (LaAlO₃) and lanthanum gallates (LaGaO₃). Their preparation features, chemical stability, thermal behaviour and transport properties are thoroughly analyzed in terms of their connection with the target functional parameters of related SOFCs. The data presented here will serve as a starting point for further studies of La-based perovskites, including in the fields of solid state ionics, electrochemistry and applied energy.

Keywords: SOFCs; solid oxide fuel cells; oxygen-ion electrolytes; perovskite; LaAlO₃; LaGaO₃; LSGM



Citation: Filonova, E.; Medvedev, D. Recent Progress in the Design, Characterisation and Application of LaAlO₃- and LaGaO₃-Based Solid Oxide Fuel Cell Electrolytes. *Nanomaterials* **2022**, *12*, 1991. <https://doi.org/10.3390/nano12121991>

Academic Editors: Hanfeng Liang, Qiu Jiang, Gang Huang and Yi-Zhou Zhang

Received: 11 May 2022

Accepted: 8 June 2022

Published: 9 June 2022

Publisher's Note: MDPI stays neutral with regard to jurisdictional claims in published maps and institutional affiliations.



Copyright: © 2022 by the authors. Licensee MDPI, Basel, Switzerland. This article is an open access article distributed under the terms and conditions of the Creative Commons Attribution (CC BY) license (<https://creativecommons.org/licenses/by/4.0/>).

1. Introduction

The long-term goal of a large body of relevant scientific research is to find a solution to the problem of providing industrial and domestic human needs with renewable and environmentally friendly energy [1,2]. The main fields of sustainable energy concern both the search for renewable energy sources [3–5] and methods for the production of ecological types of energy [6–9], which differ from traditional types based on hydrocarbon fuel [10–12]. The tasks relating to sustainable energy also include the development of technologies for the use of non-renewable energy sources: efficient waste-processing [13–15], the construction of nuclear mini-reactors [16], and the creation of energy devices based on the direct conversion of various types of energy into electrical and thermal energy [17–19]. A well-known device for directly converting the chemical energy of fuels into electrical energy is a fuel cell [19–21]. If the electrolyte in the fuel cell is a ceramic material that is permeable to oxygen ions, it is referred to as a solid oxide fuel cell (SOFC) [21–25].

The advantages of SOFCs are the absence of noble metals in their composition and the flexibility of fuel types [24,26,27], while the disadvantages include high operating temperatures, which lead to chemical interactions between the parts of the SOFCs [28,29] and fast degradation [30–32]. The high temperatures required to operate SOFCs with conventional electrolytes on the basis of yttria-stabilized zirconia (YSZ) lead to the formation of metastable phases, sealing, and thermal and chemical incompatibility with electrode materials [33–35].

One of the ways to solve the described problem is to decrease the operating temperature of SOFCs and develop fuel cells operating at medium- [36–38] and low-temperature

ranges [39,40]. This has resulted in investigations into new classes of electrolytes [41–44] and the development of SOFCs enhanced with nanostructured materials [45,46]. The utilization of nanotechnologies, energy production and energy storage devices is extremely prospective due to their durability, sustainability, long lifetime, and low cost [47]. Among the alternative electrolytes used in low- and intermediate-temperature SOFCs, complex oxides with an ABO_3 -type perovskite structure have attracted specific attention due to their high efficiency in energy conversion [48–50]. Sr, Mg-doped lanthanum gallate ($LaGaO_3$), possessing a high oxide ionic conductivity, which was established originally by Ishihara et al. in 1994 [51], was first used in SOFCs by Feng and Goodenough in 1996 [52]. Later, much more economical materials based on doped lanthanum aluminate $LaAlO_3$ were reported by Fung and Chen in 2011 [53].

It is worth noting that previous generalizing works on lanthanum aluminate were aimed at the synthesis and characterization of $LaAlO_3$ phosphors (published by Kaur et al. in 2013 [54]) and at some properties and applications of $LaAlO_3$ not concerned with SOFCs (observed by Rizwan et al., in 2019) [55]. There is only one overview dedicated to Sr, Mg-doped $LaGaO_3$ oxides as electrolytes for intermediate-temperature solid oxide fuel cells: this was published by Morales et al. in 2016 [56]. The present overview is dedicated to recent progress in the design, characterization and application of electrolyte materials for SOFCs based on the $LaGaO_3$ and $LaAlO_3$ complex oxides with a perovskite structure. Both these phases constitute a family of oxygen-conducting electrolytes, while other La-based perovskites ($LaScO_3$, $LaInO_3$, $LaYO_3$, $LaYbO_3$) exhibit protonic conductivity as well [49]. For this reason, scandates, indates, yttrates, and ytterbates are not considered within the present review.

A schematic image of an ABO_3 perovskite structure is shown in Figure 1a,b. Typically, the size of A-site cations is larger than that of B-site cations, but is roughly close to that of the oxygen ions. The A-site cations are surrounded by 12 oxygen-ions in a cubo-octahedral coordination; the B-site cations are surrounded by 6 oxygen-ions in an octahedral coordination. In an ideal perovskite structure, BO_6 octahedrons are linked at the corners, thus exhibiting the cubic $Pm\bar{3}m$ space group.

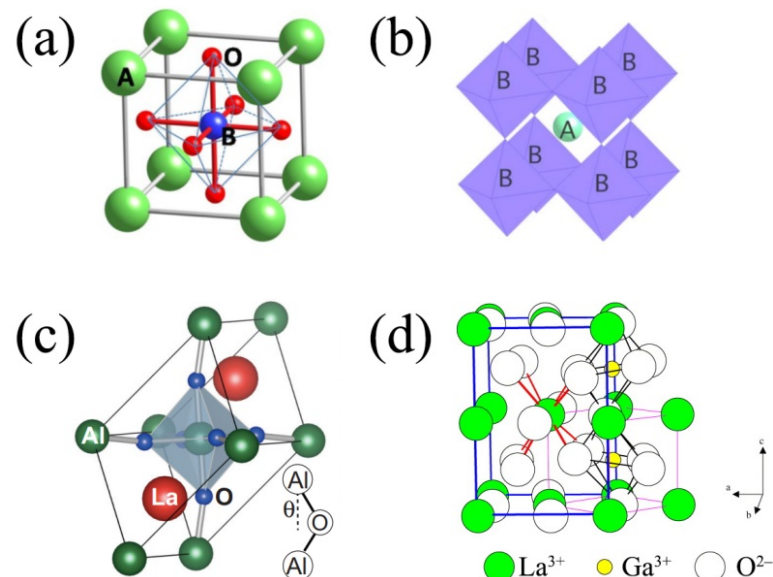


Figure 1. ABO_3 perovskite structure: (a) B-cation centered and (b) A-cation centered representations; the perovskite structure of the ABO_3 complex oxide with the B (a) and A (b) central ions [57]; (c) a rhombohedral crystal structure (for example, $LaAlO_3$). Reproduced from [58] with permission from the American Physical Society, 2016; (d) an orthorhombic crystal structure (for example, $LaGaO_3$) Reproduced from [59] with permission by Elsevier Ltd. (Amsterdam, The Netherlands), 2004.

If the complex oxide structure differs from the ideal perovskite structure by having rhombohedral or orthorhombic distortions due to the BO_6 octahedron arrangement, the stability of this oxide can be evaluated with the Goldsmith tolerance factor t equation [60] as follows:

$$t = \frac{r_A + r_O}{\sqrt{2}(r_B + r_O)}, \quad (1)$$

where r_A , r_B , r_O are the ionic radii of the A-, B-cations, and oxygen ions, respectively. If t is equal to 1, an ideal cubic-type perovskite structure is formed. If t deviates from 1, various distortions occur in the ideal perovskite structure. The first reason for such distortions is the rotation of the BO_6 octahedron without axis deformation, which causes tilting around the large A-cations. Take, for example, the rhombohedral structure of LaAlO_3 at room temperature presented in Figure 1c. The second reason consists of the appearance of the irregularity in the BO_6 octahedrons due to the non-centrality of the B-site cations. Consider, for example, the orthorhombic structure of LaGaO_3 at room temperature presented in Figure 1d.

2. Electrolyte Materials Based on LaAlO_3

2.1. Synthesis, Structure and Morphology

For the synthesis of doped LaAlO_3 oxides, several well-developed techniques are usually used: solid-state reaction technology [61–64], the mechanochemical route [65], co-precipitation [66,67] and organic-nitrate precursor pyrolysis [68–75].

Employing conventional solid-state reaction technology, LaAlO_3 samples can be directly obtained from La_2O_3 and Al_2O_3 . In [61], these initial reactants were ground down, homogenized in a water media, desiccated and pressed into pellets annealed at a temperature range of 780–1100 °C. Such a temperature regime allows for single-phase LaAlO_3 samples to be prepared. A similar technology was used in work [62] to synthesize $\text{LaAl}_{1-x}\text{Zn}_x\text{O}_{3-\delta}$ (here, δ is the oxygen nonstoichiometry; $\delta = x/2$ in the case of oxidation-state stable cations and one charge state difference between the host and impurity cations). As initial reagents, stoichiometric amounts of aluminium and zinc oxides were milled in ethanol. The heat treatment included five 24-h stages at a temperature range of 700–1100 °C. Single-phased LaAlO_3 and $\text{LaAl}_{0.95}\text{Zn}_{0.05}\text{O}_{3-\delta}$ were obtained at 1250 and 1200 °C, respectively.

Fabian et al. [65] synthesised Ca-doped LaAlO_3 powders using the mechanochemical method. Oxide powders of La_2O_3 , $\gamma\text{-Al}_2\text{O}_3$ and CaO in appropriate proportions were milled in a planetary mill at 600 rpm. The prepared powders were pressed into disks with polyethylene glycol as a plasticizer. The LaAlO_3 and $\text{La}_{1-x}\text{Ca}_x\text{AlO}_{3-\delta}$ pellets were sintered at 1700 and 1450 °C, respectively, to achieve a desirable ceramic densification.

LaAlO_3 complex oxides were prepared starting from water solutions of aluminium and lanthanum chlorides with a molar ratio for the metal components of 1:1 [66]. Solutions with high and low concentrations of starting reagents were mixed with an ammonium solution serving as a precipitation agent. The obtained gels were filtered, washed with distilled water and dried twice, at 25 °C for 24 h and at 100 °C for 2 h. The prepared powders were calcined at a temperature range of 600–900 °C for 1 h. The powder obtained from the high-concentration solution was annealed at 900 °C for 2 h in air, then ground in a rotary mill with zirconia balls in dry ethanol, pressed and calcined at 1300–1500 °C for 2 h.

The most widely used technology for the preparation of LaAlO_3 and its doped derivatives is the pyrolysis of organic-nitrate compositions, known as the sol-gel [68,69,74] or autocombustion methods (or self-propagating high-temperature synthesis, and the Pechini method) [70–73,75]. Utilizing different fuels during the pyrolysis process coupled with various annealing temperatures affects the crystallinity, powder dispersity, and ceramics density, determining the functional properties of the obtained LaAlO_3 -based ceramic materials [74,76,77].

LaAlO_3 powders were prepared by Zhang et al. [68] from $\text{La}(\text{NO}_3)_3 \cdot 6\text{H}_2\text{O}$ and $\text{Al}(\text{NO}_3)_3 \cdot 9\text{H}_2\text{O}$: they were dissolved in 2-methoxyethanol and then mixed with citric acid at a molar ratio of 1:1 to the total content of metal ions. The obtained solutions were

heated and dried at 80 °C until gelatinous LaAlO_3 precursors were obtained, which were then calcined at 600–900 °C for 2 h.

To obtain $\text{La}_{0.9}\text{Sr}_{0.1}\text{Al}_{0.97}\text{Mg}_{0.03}\text{O}_{3-\delta}$ powder, $\text{La}(\text{NO}_3)_3 \cdot 6\text{H}_2\text{O}$, $\text{Al}(\text{NO}_3)_3 \cdot 9\text{H}_2\text{O}$, $\text{Mg}(\text{NO}_3)_2 \cdot 6\text{H}_2\text{O}$, $\text{Sr}(\text{NO}_3)_2$, EDTA, $\text{C}_2\text{H}_5\text{NO}_2$ and $\text{NH}_3 \cdot \text{H}_2\text{O}$ were used in [69]. The molar ratio of glycine and EDTA to overall metal-ion content was 1.2:1:1; the ratio of $\text{NH}_3 \cdot \text{H}_2\text{O}$ to EDTA was adjusted to 1.15:1. The aqueous solution of metal nitrates was prepared and heated at 80 °C, and then the EDTA-ammonia solution and glycine were added. The colourless solution was dried, and the obtained brown resin was calcined at 350 °C; it was then ground down and calcined at 600–1000 °C for 3 h. The obtained powders were finally pressed into disks followed by sintering at 1600–1700 °C for 5 h.

According to Adak and Pramanik [70], LaAlO_3 was prepared from a 10% aqueous polyvinyl alcohol precursor that was added to a solution obtained from La_2O_3 (99%) dissolved in nitric acid and $\text{Al}(\text{NO}_3)_3 \cdot 9\text{H}_2\text{O}$. The organic-nitrate mixture was evaporated at 200 °C until dehydration; then, spontaneous decomposition and the formation of a voluminous black fluffy powder occurred. The obtained powders were ground down and annealed at 600–800 °C for 2 h to form a pure phase.

Verma et al. [71] synthesized LaAlO_3 and $\text{La}_{0.9-x}\text{Sr}_{0.1}\text{Ba}_x\text{Al}_{0.9}\text{Mg}_{0.1}\text{O}_{3-\delta}$ ($x = 0.00, 0.01$ and 0.03) samples from initial reagents composed of $\text{La}(\text{NO}_3)_3 \cdot \text{H}_2\text{O}$, $\text{Sr}(\text{NO}_3)_2$, $\text{Ba}(\text{NO}_3)_2$, $\text{Al}(\text{NO}_3)_3 \cdot 6\text{H}_2\text{O}$ and $\text{Mg}(\text{NO}_3)_2 \cdot 6\text{H}_2\text{O}$ initial reagents. $\text{C}_6\text{H}_8\text{O}_7 \cdot \text{H}_2\text{O}$ was used as an organic fuel. The metal nitrates and citric acid were dissolved in distilled water, resulting in the formation of a transparent solution. The pH value required for proper combustion was achieved by the addition of ammonia solution. The self-propagating synthesis method is shown in Figure 2a. The obtained powders were calcined at 700 °C for 4 h, then pressed into pellets and sintered at 1300 °C for 8 h to achieve 92-to-96% relative density, depending on the aluminate composition.

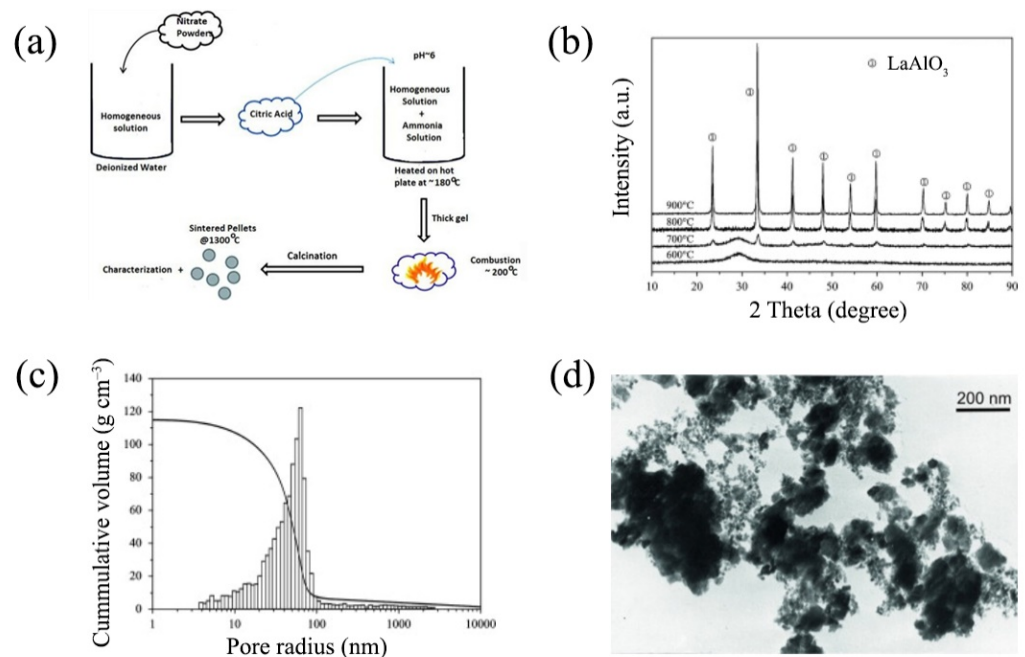


Figure 2. Preparation features of LaAlO_3 -based materials: (a) diagram of auto-combustion synthesis. Reproduced from [71] with permission from Springer Nature (Berlin/Heidelberg, Germany), 2021; (b) XRD patterns for LaAlO_3 powders prepared and calcined at a temperature range of 600–900 °C for 1 h on each stage. Reproduced from [66] with permission by Elsevier Ltd., 2013; (c) pore size distributions of LaAlO_3 powder bodies calcined at 900 °C for 2 h. Reproduced from [66] with permission by Elsevier Ltd., 2013; (d) TEM image of LaAlO_3 powder calcined at 900 °C for 2 h. Reproduced from [66] with permission by Elsevier Ltd., 2013.

The literature shows that the annealing temperature of the precursor powders plays a significant role in complex oxide synthesis: this regulates the density of the final polycrystalline ceramic samples [78]. For practical applications, it is important to obtain LaAlO₃-based samples with a narrow distribution of fine-grained particles. These requirements were fulfilled in [66], where a fully converted LaAlO₃ phase was formed at relatively low temperatures. In more detail, the authors developed a co-precipitation technique enabling the formation of single-phase LaAlO₃ powders after its calcination in air at 900 °C for 2 h (Figure 2b). A narrow particle size distribution for LaAlO₃ powder was achieved in [66], where milling in an ethanol medium was conducted. As shown in Figure 2c, the milled LaAlO₃ powder exhibited mono-modal pore size distribution. The TEM image (Figure 2d) demonstrates that the calcined powder consisted of isometric particles of up to 15 nm in size. The use of a precursor solution with a high concentration of metal chlorides and ammonia allowed for the researchers to realize gel homogeneity and the direct synthesis of LaAlO₃.

A Rietveld analysis of the XRD pattern confirmed the presence of a pure perovskite phase with a rhombohedral structure, referring to the *R-3c* space group. Reference [66] calculated unit cell parameters for the LaAlO₃ sample ($a = 5.3556(1)$ Å and $c = 13.1518(2)$ Å) agreed well with results from neutron powder diffraction [79]. The primitive LaAlO₃ cell consists of two formula units, as shown in Figure 1b. The rotation of AlO₆ octahedra is caused by changes to the θ angle (Al–O–Al). Above 540 °C, a phase transition from the rhombohedral to cubic structure was observed for LaAlO₃ [79]. The cubic lattice of LaAlO₃ with a unit cell parameter of $a = 3.8106(1)$ Å corresponds to the *Pm3m* space group [79] (see Figure 1a).

Concluding the chapter about the synthesis methods of doped LaAlO₃ oxides, from the perspective of their use in SOFCs, the co-precipitation method should be noted as the most optimal synthetic method. The co-precipitation method with a subsequent sintering of samples at 900 °C is well-approved and allows for both single-phase powders with a narrow nano-size particle distribution and ceramic samples with high relative densities to be obtained.

2.2. Functional Properties

LaAlO₃, a basic (undoped) lanthanum aluminate, has very low electrical conductivity, equal to around 1×10^{-6} S cm⁻¹ at 900 °C [75]. La-site doping of LaAlO₃ with strontium enhances electrical conductivity because it improves the oxygen vacancy concentration responsible for oxygen-ion transport (Equation (2), [80]). Al-site modification of LaAlO₃ with acceptor dopants (for example, magnesium) can also increase the total and ionic conductivities (see Figure 3a).

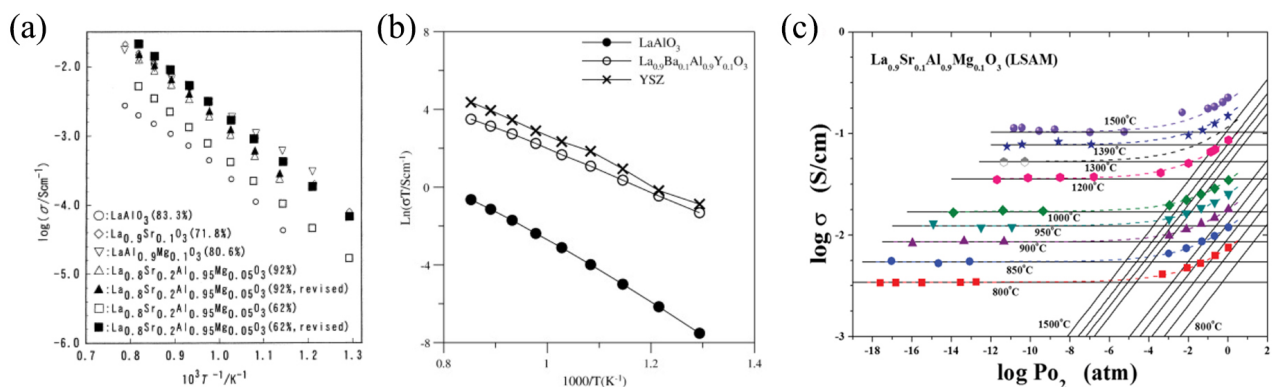
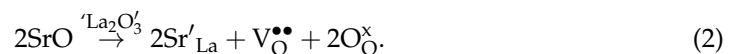


Figure 3. Functional properties of LaAlO₃-doped materials: (a) electrical conductivity of LaAlO₃, La_{0.9}Sr_{0.1}AlO_{3-δ}, LaAl_{0.9}Mg_{0.1}O_{3-δ}, La_{0.8}Sr_{0.2}Al_{0.95}Mg_{0.05}O_{3-δ} samples. Reproduced from [80] with

permission by Elsevier Ltd., 2000; (b) electrical conductivity of LaAlO_3 , $\text{La}_{0.9}\text{Ba}_{0.1}\text{Al}_{0.9}\text{Y}_{0.1}\text{O}_{3-\delta}$, and YSZ as a reference sample. Reproduced from [53] with permission by Elsevier Ltd., 2011; (c) total conductivity of the $\text{La}_{0.9}\text{Ba}_{0.1}\text{Al}_{0.9}\text{Y}_{0.1}\text{O}_{3-\delta}$ ceramic as function of oxygen partial pressures [81].

The possibility of forming good oxygen-ionic conductivity by doping LaAlO_3 oxides has promoted studies on their potential application in SOFCs [53,65,71,82–90]. The co-doping strategy is a beneficial way to further increase ionic conductivity [80,82,83,87]; this is due to the fact that, along with Equation (2), an additional quantity of oxygen vacancies can be formed according to the following mechanism [80]:



According to the results of [53], the simultaneous doping of LaAlO_3 with barium and yttrium drastically enhanced ionic transport. For example, the total conductivity of $\text{La}_{0.9}\text{Ba}_{0.1}\text{Al}_{0.9}\text{Y}_{0.1}\text{O}_{3-\delta}$ at 800 °C was close to that of YSZ ($2 \times 10^{-2} \text{ S cm}^{-1}$), as shown in Figure 3b. There are various ways to tailor the transport properties of LaAlO_3 -based materials. For example, the doping of $(\text{La,Sr})\text{AlO}_3$ with manganese resulted in total conductivity rising due to the substitution of Mn^{3+} ions, which were transformed into Mn^{2+} and Mn^{4+} ions at the Al^{3+} position, enhancing an electronic contribution [75,84]. Therefore, co-doped $(\text{La,Sr})(\text{Al,Mn})\text{O}_3$ is attributed to mixed ionic-electronic conductors (MIEC). The Pr-doping of $(\text{La,Sr})\text{AlO}_3$ had a positive influence on transport properties due to the suppression of grain boundary resistivity [85], and the isovalent substitution of La^{3+} -ions with Sm^{3+} -ions in $(\text{La,Sr})\text{AlO}_{3-\delta}$ resulted in the formation of a pronounced mixed ion-electron conduction [88] due to the generation of more electrons than in the case of the aliovalent substitution of La^{3+} ions with Ba^{2+} ions.

The electrical conductivity values of LaAlO_3 -based ceramic materials are summarized in Table 1. Analysis of these data confirms that the simultaneous modification of both sublattices of LaAlO_3 results in improved conductivity compared to those reached using single doping approaches (see Figure A1). However, it should be noted that the Sr- and Mg-co-doped LaAlO_3 materials exhibit mixed ionic-electronic conduction in air atmospheres over a wide temperature range (800–1400 °C, see Figure 3c), while predominant ionic transport occurs for more reduced atmospheres (for example, wet hydrogen). This is typical behaviour for various La-based perovskites [49] as well as for other perovskite-related ion-conducting electrolytes [91].

Thermal expansion coefficients (TECs) play an important role in material selection when seeking to avoid thermal incompatibilities between various parts of SOFCs. According to da Silva and de Miranda [75], the average TEC values for LaAlO_3 and $\text{La}_{0.8}\text{Sr}_{0.2}\text{AlO}_3$ were equal to around 11.4×10^{-6} and $9.9 \times 10^{-6} \text{ K}^{-1}$, respectively. These data confirm that the TEC values of LaAlO_3 -based materials were close to those of the conventional YSZ electrolyte, i.e., $10.9 \times 10^{-6} \text{ K}^{-1}$ [92].

The chemical compatibility of $\text{La}_{0.9}\text{Sr}_{0.1}\text{Al}_{0.97}\text{Mg}_{0.03}\text{O}_{3-\delta}$ as an electrolyte material with $\text{NiO-Ce}_{0.9}\text{Gd}_{0.1}\text{O}_{2-\delta}$, $\text{Sr}_{0.88}\text{Y}_{0.08}\text{TiO}_{3-\delta}$ and $\text{La}_{0.75}\text{Sr}_{0.25}\text{Cr}_{0.5}\text{Mn}_{0.5}\text{O}_{3-\delta}$ as anode SOFC materials was thoroughly investigated in [87] using XRD analysis and scanning electron microscopy with energy-dispersive X-ray spectroscopy. The obtained results demonstrated that $\text{Sr}_{0.88}\text{Y}_{0.08}\text{TiO}_{3-\delta}$ and $\text{La}_{0.75}\text{Sr}_{0.25}\text{Cr}_{0.5}\text{Mn}_{0.5}\text{O}_{3-\delta}$ interacted with $\text{La}_{0.9}\text{Sr}_{0.1}\text{Al}_{0.97}\text{Mg}_{0.03}\text{O}_{3-\delta}$ due to the interdiffusion of Sr^{2+} , Ti^{4+} , Mn^{3+} and Cr^{3+} cations into the $\text{La}_{0.9}\text{Sr}_{0.1}\text{Al}_{0.97}\text{Mg}_{0.03}\text{O}_{3-\delta}$ lattice. An interaction between $\text{La}_{0.9}\text{Sr}_{0.1}\text{Al}_{0.97}\text{Mg}_{0.03}\text{O}_{3-\delta}$ and $\text{NiO-Ce}_{0.9}\text{Gd}_{0.1}\text{O}_{2-\delta}$ at 1300 °C was not detected, which means that joint utilization is possible.

The XRD patterns of two mixtures, $\text{La}_{0.8}\text{Sr}_{0.2}\text{Ga}_{0.85}\text{Mg}_{0.15}\text{O}_{3-\delta}/\text{La}_{0.9}\text{Sr}_{0.1}\text{AlO}_{3-\delta}$ and $\text{NiO}/\text{La}_{0.9}\text{Sr}_{0.1}\text{AlO}_{3-\delta}$ (annealed at 1450 °C), confirmed that there were no chemical interactions between these components [93]. The authors noted that doped LaAlO_3 materials can serve as additives to the composite electrolytes and the anode-protective layers [93]. In addition, Mn-doped LaAlO_3 phases are considered a constituent part of the composite

electrolytes, providing for the effective electrochemical oxidation of methane via ethylene and ethane [94].

Table 1. Total conductivity and activation energy values for LaAlO₃ ceramic materials. Figure A1 (see the Appendix A) provides a visualization of these data.

Sample	T (°C)	σ (S cm ⁻¹)	E_a (eV)	Ref.
LaAlO ₃	900	6×10^{-4}	1.30	[53]
LaAlO ₃	700	6.7×10^{-4}	0.99	[71]
LaAlO ₃	900	1.1×10^{-6}	1.83	[75]
LaAlO ₃	900	1.4×10^{-3}	1.88	[80]
LaAlO ₃	800	2.0×10^{-4}	1.30	[83]
La _{0.9} Ca _{0.1} AlO _{3-δ}	900	6.0×10^{-3}	1.08	[65]
La _{0.9} Sr _{0.1} AlO _{3-δ}	900	1.1×10^{-2}	1.14	[80]
La _{0.9} Sr _{0.1} AlO _{3-δ}	800	9.0×10^{-3}	0.93	[85]
La _{0.8} Sr _{0.2} AlO _{3-δ}	800	6.2×10^{-3}	1.06	[75]
La _{0.8} Sr _{0.2} AlO _{3-δ}	900	1.5×10^{-2}	1.06	[75]
La _{0.8} Sr _{0.2} AlO _{3-δ}	900	1.1×10^{-2}	1.16	[80]
La _{0.8} Sr _{0.2} AlO _{3-δ}	810	4.3×10^{-3}	1.06	[84]
La _{0.7} Pr _{0.2} Sr _{0.1} AlO _{3-δ}	800	2.3×10^{-2}	0.84	[85]
LaAl _{0.95} Zn _{0.05} O _{3-δ}	700	8.5×10^{-4}	1.05	[62]
LaAl _{0.95} Zn _{0.05} O _{3-δ}	900	1.1×10^{-3}	1.05	[62]
LaAl _{0.9} Mg _{0.1} O _{3-δ}	900	9.6×10^{-3}	1.05	[80]
LaAl _{0.5} Mn _{0.5} O _{3-δ}	800	4.7(2)	0.22	[75]
LaAl _{0.5} Mn _{0.5} O _{3-δ}	900	5.8(2)	0.22	[75]
La _{0.9} Sr _{0.1} Al _{0.9} Mg _{0.1} O _{3-δ}	700	2.6×10^{-3}	1.56	[71]
La _{0.9} Sr _{0.1} Al _{0.9} Mg _{0.1} O _{3-δ}	700	5.3×10^{-4}	1.38	[88]
La _{0.9} Sr _{0.1} Al _{0.9} Mg _{0.1} O _{3-δ}	900	2.0×10^{-2}	0.90	[82]
La _{0.8} Sr _{0.2} Al _{0.95} Mg _{0.05} O _{3-δ}	900	1.3×10^{-2}	1.15	[80]
La _{0.89} Sr _{0.1} Ba _{0.01} Al _{0.9} Mg _{0.1} O _{3-δ}	700	2.6×10^{-3}	1.48	[71]
La _{0.89} Sr _{0.1} Ba _{0.01} Al _{0.9} Mg _{0.1} O _{3-δ} tape	700	6.0×10^{-4}	0.60	[86]
La _{0.89} Sr _{0.1} Ba _{0.01} Al _{0.9} Mg _{0.1} O _{3-δ} pellet	700	4.6×10^{-2}	0.75	[86]
La _{0.87} Sr _{0.1} Ba _{0.03} Al _{0.9} Mg _{0.1} O _{3-δ}	700	1.7×10^{-3}	1.38	[71]
La _{0.8} Sr _{0.2} Al _{0.5} Mn _{0.5} O _{3-δ}	800	8.6(3)	0.15	[75]
La _{0.8} Sr _{0.2} Al _{0.5} Mn _{0.5} O _{3-δ}	900	9.8(2)	0.15	[75]
La _{0.8} Sr _{0.2} Al _{0.7} Mn _{0.3} O _{3-δ}	810	0.75	0.29	[84]
La _{0.8} Sr _{0.2} Al _{0.5} Mn _{0.5} O _{3-δ}	810	10	0.17	[84]
(La _{0.8} Sr _{0.2}) _{0.94} Al _{0.5} Mn _{0.5} O _{3-δ}	810	12	0.14	[84]
La _{0.9} Ba _{0.1} Al _{0.9} Y _{0.1} O _{3-δ}	800	1.8×10^{-2}	0.82	[53]
La _{0.9} Ba _{0.1} Al _{0.9} Y _{0.1} O _{3-δ}	900	3.1×10^{-2}	0.82	[53]
La _{0.87} Sr _{0.1} Sm _{0.03} Al _{0.9} Mg _{0.1} O _{3-δ}	700	1.2×10^{-3}	1.09	[88]
La _{0.85} Sr _{0.1} Sm _{0.05} Al _{0.9} Mg _{0.1} O _{3-δ}	700	1.1×10^{-3}	1.10	[88]

2.3. Applications in SOFCs

There are fragmentary data on the application of lanthanum aluminate electrolytes in SOFCs; see Figure 4.

For example, an SOFC was fabricated with 70% NiO–30% YSZ as an anode, SDC as an interlayer, La_{0.9}Ba_{0.1}Al_{0.9}Y_{0.1}O_{3- δ} (LBAYO) as an electrolyte and LSM as a cathode, and tested in [53]. LBAYO films with thicknesses of 63 and 74 μ m were electrophoretically deposited on the LSM pellets with a diameter of 25 mm and a thickness of 2 mm. The LSM substrates and the deposited LBAYO films were then annealed at 1450 °C for 2 h to achieve full electrolyte densification. The thickness of the LBAYO film varied due to increases in the applied voltage. A NiO/YSZ anode with a thickness of 40 μ m was screen-printed on the LBAYO/LSM sample and then sintered at 1500 °C for 6 h. To avoid chemical interactions between the NiO and the LBAYO film, an SDC buffer layer with a thickness of 10 μ m was additionally screen-printed on the LBAYO film between the electrolyte and the anode. Humidified hydrogen was used as a fuel, while air was used as an oxidant. Figure 4a presents the SEM micrograph of the NiO–YSZ/SDC/LBAYO/LSM

cell, indicating that after the annealing procedure, the LBAYO film was highly densified without cracks with a uniform thickness and a strong adhesion to the LSM substrate. The open-circuit voltage (OCV) values of the fabricated cells were 0.927 and 0.953 V, while the maximum power density values were 0.306 and 0.235 W cm⁻² for the LBAYO electrolyte layers with thicknesses of 63 and 74 μm, respectively (Figure 4b). The authors of the work attributed the sharp decrease in the cells' voltage at a small current to the slow oxygen reduction reaction kinetics for the LSM cathode.

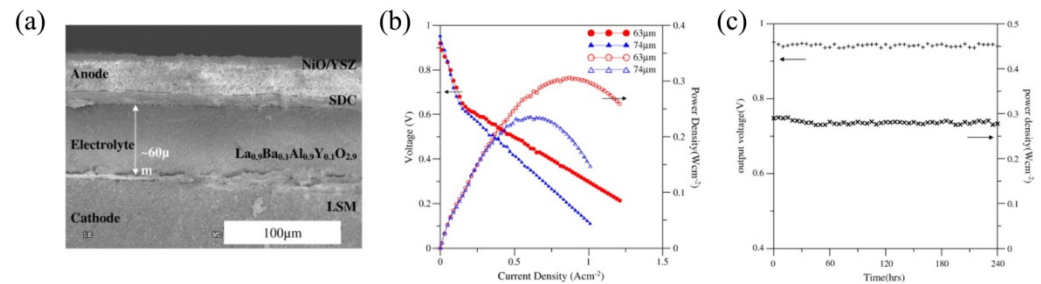


Figure 4. Properties of the NiO-YSZ/SDC/LBAYO/LSM SOFC: (a) SEM micrograph of a cell sintered at 1500 °C for 6 h; (b) current-voltage and current-power dependencies of a cell with an electrolyte thickness of 63 μm tested at different temperatures; (c) time dependencies of OCV and P_{\max} measured at 800 °C for 10 days. These images were reproduced from [53] with permission from Elsevier Ltd., 2011.

The long-term stability experiments demonstrated negligible degradation of the LBAYO electrolyte over 10 days. Figure 4c illustrates the time dependencies of the obtained open circuit voltage (OCV) and the maximum power density (P_{\max}) for a cell tested at 800 °C.

Another Ni-GDC/GDC/La_{0.9}Sr_{0.1}Al_{0.97}Mg_{0.03}O_{3-δ}/GDC/La_{0.75}Sr_{0.25}FeO_{3-δ} electrolyte-supported cell was tested in [87]. For this single cell with a La_{0.9}Sr_{0.1}Al_{0.97}Mg_{0.03}O_{3-δ} electrolyte thickness of 550 μm, the OCV and P_{\max} values at 800 °C were found to be equal to 0.925 V and 19.5 mW cm⁻², respectively.

3. Electrolyte Materials Based on Doped LaGaO₃

3.1. Synthesis, Structure and Morphology

Historically, La_{1-x}Sr_xGa_{1-y}Mg_yO_{3-δ} (LSGM) oxides were the first well-studied doped materials in the LaGaO₃ system. In 1998, Huang, Tichy and Goodenough determined the existence of single-phase La_{1-x}Sr_xGa_{1-y}Mg_yO_{3-0.5(x+y)} perovskites while studying a LaO_{1.5}-SrO-GaO_{1.5}-MgO quasi-quaternary diagram [95] (see Figure 5a). This was possible due to variations in both x and y contents in a composition range of 0.05–0.30 with a step of 0.05. Sr- and Mg- co-doped LaGaO₃ samples were prepared from La₂O₃, SrCO₃, Ga₂O₃, and MgO using solid-state reaction technology. The obtained powders were pressed into pellets and calcined at 1250 °C for 12 h. After remilling and repressing, the final pellets were finally sintered in air at 1470 °C for 24 h and quenched in a furnace at 500 °C.

Similar conventional techniques for synthesizing La_{1-x}Sr_xGa_{1-y}Mg_yO_{3-δ} were used in other studies [96,97]. La_{0.9}Sr_{0.1}Ga_{0.8}Mg_{0.2}O_{3-δ} samples were obtained from La₂O₃, SrCO₃, Ga₂O₃ and MgO sources, which were mixed and sintered in a platinum crucible at 1350 °C for 12 h [96]. The annealed powder was milled with zirconia balls and dried. Then, the powder was pressed into disks and sintered at 1350 °C in air, nitrogen or oxygen atmospheres for various times ranging from 20 min to 5 h. Moure et al. [97] obtained La_{0.8}Sr_{0.2}Ga_{0.85}Mg_{0.15}O_{3-δ} and La_{0.8}Sr_{0.15}Ga_{0.85}Mg_{0.2}O_{3-δ} samples from La₂O₃, SrCO₃, Ga₂O₃ and MgO, which were mechanochemically activated in a Pulverizette 6 Fritsch planetary mill with stainless steel balls. The mixtures were synthesized at 1300 °C for 16 h; then after milling for 2 h and sieving with a 100-μm sieve, the powders were pressed into pellets and finally sintered at 1550 °C to form the desired ceramic samples.

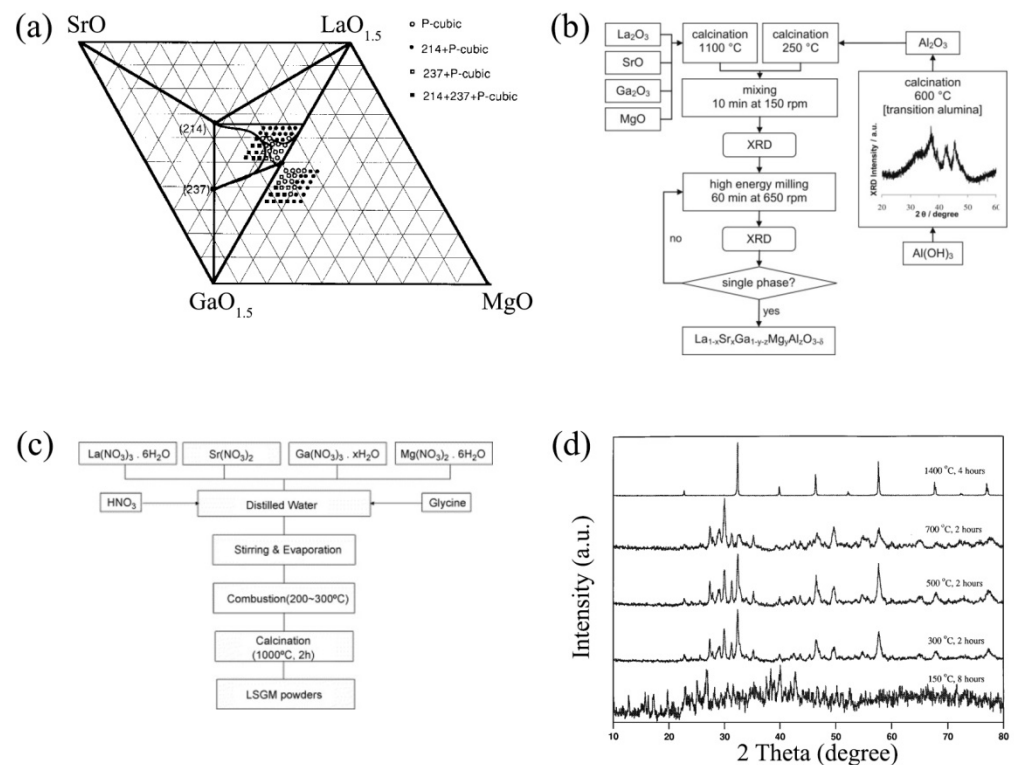


Figure 5. The phase and structure features of LaGaO₃-based materials: (a) phase diagram of a LaO_{1.5}–SrO–GaO_{1.5}–MgO system up to 800 °C, P-cubic = single-phase La_{1-x}Sr_xGa_{1-y}Mg_yO_{3-δ}, 214 = LaSrGaO₄, 237 = LaSrGa₃O₇. Reproduced from [95] with permission from John Wiley & Sons, Inc. (Hoboken, NJ, USA), 1998; (b) the scheme of mechanochemical synthesis for the preparation of La_{1-x}Sr_xGa_{1-y}Mg_yAl_zO_{3-δ}. Reproduced from [98] with permission by Elsevier Masson SAS, 2012; (c) the combustion scheme synthesis for the preparation of La_{1-x}Sr_xGa_{1-y}Mg_yO_{3-δ}. Reproduced from [99] with permission by Elsevier Ltd., 2007; (d) XRD pattern evaluation of La_{0.8}Sr_{0.2}Ga_{0.83}Mg_{0.17}O_{3-δ} precursor powders at various calcination temperatures. Reproduced from [100] with permission from Elsevier Ltd., 1998.

For the synthesis of La_{0.9}Sr_{0.1}Ga_{1-x}Ni_xO_{3-δ}, Colomer and Kilner [101] grinded a mixture of La₂O₃, SrCO₃, Ga₂O₃ and NiO in an agate mortar with acetone medium and then calcined them at 1000 °C for 6 h. After sieving with a 65-μm sieve, milling for 1 h, drying and secondary sieving to 65 μm, the finishing powders were pressed into disks and sintered at 1450–1500 °C for 48 h in air. The authors chose nickel as element for gallium substitution in La_{0.9}Sr_{0.1}GaO_{3-δ} owing to the proposal about achieving a hopping conductivity among the Ni-sites.

Al-substituted La_{0.95}Sr_{0.05}Ga_{0.9}Mg_{0.1}O_{3-δ} and La_{0.9}Sr_{0.1}Ga_{0.8}Mg_{0.2}O_{3-δ} derivatives were prepared using La₂O₃, Ga₂O₃, SrO, MgO and Al₂O₃ [98]. Mechanochemical synthesis was employed in a planetary mill (Retsch PM100, PM200) with tetragonal zirconia balls, according to a scheme presented in Figure 5b. The powders were pressed into disks that were sintered at 1300–1450 °C for 2–24 h.

As can be seen, the aforementioned methods (solid-state reaction synthesis and the mechanochemical route) that were conventionally used for the preparation of La_{1-x}Sr_xGa_{1-y}Mg_yO_{3-δ} and its derivatives have two considerable disadvantages. First, high sintering temperatures (above 1450–1500 °C) are required for full densification of the pressed pellets [51]. This can influence the production cost of the final electrolyte materials. Second, the appearance of Sr₃La₄O₉, SrLaGa₃O₇ and/or SrLaGaO₄ impurity phases in La_{1-x}Sr_xGa_{1-y}Mg_yO_{3-δ} samples was frequently observed. This was due to gallium evaporation [102], which resulted in the deterioration of the gallate material's ionic conductivity [51]. To solve the problems that arise during La_{1-x}Sr_xGa_{1-y}Mg_yO_{3-δ}

preparation, techniques based on co-precipitation [103,104], organic-nitrate precursors combustion [96,99,100,105–109], self-propagating, high-temperature synthesis [110,111] and spray-pyrolysis [112] were developed.

For example, $\text{La}_{0.8}\text{Sr}_{0.2}\text{Ga}_{0.8}\text{Mg}_{0.2}\text{O}_{3-\delta}$ samples were prepared with carbonate co-precipitation from $\text{La}(\text{NO}_3)_3 \cdot 6\text{H}_2\text{O}$, $\text{Sr}(\text{NO}_3)_2$, $\text{Ga}(\text{NO}_3)_3 \cdot x\text{H}_2\text{O}$ and $\text{Mg}(\text{NO}_3)_2 \cdot 6\text{H}_2\text{O}$ starting reagents [103]. The resulting aqueous solution containing La^{3+} , Sr^{2+} , Ga^{3+} and Mg^{2+} cations was gradually dropped into an aqueous $(\text{NH}_4)_2\text{CO}_3$ solution with heating at 70 °C. After 2 h of homogenization with continuous stirring, the formed sediments were washed, dried at 25 °C for 24 h in a N_2 atmosphere, and finally calcined in air at 900–1300 °C for 12 h.

Huang and Goodenough [100] have reported the use of wet synthesis techniques (the sol-gel technique and the Pechini method) for forming single-phase $\text{La}_{0.8}\text{Sr}_{0.2}\text{Ga}_{0.83}\text{Mg}_{0.17}\text{O}_{3-\delta}$ materials. Solutions of $\text{La}(\text{CH}_3\text{COO})_3$, $\text{Sr}(\text{CH}_3\text{COO})_2$ and $\text{Mg}(\text{CH}_3\text{COO})_2$ acetates and $\text{La}(\text{NO}_3)_3$, $\text{Sr}(\text{NO}_3)_2$, $\text{Ga}(\text{NO}_3)_3$ and $\text{Mg}(\text{NO}_3)_2$ nitrates were used in these preparation methods. During synthesis with sol-gel technology, the required amounts of metal acetates and gallium nitrate solutions were mixed by stirring. An ammonia solution was then added, forming a white gel. This was aged at 25 °C for 72 h and heated at 150 °C for 8 h upon full water evaporation. The resulting product was fired at 300, 500 and 700 °C at varying times. Using the Pechini method, $\text{La}_{0.8}\text{Sr}_{0.2}\text{Ga}_{0.83}\text{Mg}_{0.17}\text{O}_{3-\delta}$ samples were prepared from a mixture of the necessary amounts of metal nitrate solutions at 25 °C: citric acid was then added. The citric acid was used to fulfil a mole ratio of citric acid/total cations around 1.5/1. After stirring the precursor solution, ethylene glycol was added in an equal amount to the citric acid. The obtained solution was heated at 150 °C for 12 h and resulted in a polymer-like solid material. This resin was slowly heated to 300 °C and, after several sintering stages, it was finally calcined at 1400 °C for 4 h [100]. The pressed $\text{La}_{0.85}\text{Sr}_{0.15}\text{Ga}_{0.8}\text{Mg}_{0.2}\text{O}_{3-\delta}$ samples were found to be single-phase after they were obtained via the Pechini method and annealed at 1400 °C for 6 h [105].

A $\text{La}_{0.8}\text{Sr}_{0.2}\text{Ga}_{0.85}\text{Mg}_{0.15}\text{O}_{3-\delta}$ sample was also obtained via the glycine-nitrate combustion method [106]. Ga , La_2O_3 , MgO and SrCO_3 powders were dissolved in strong HNO_3 and mixed with water. Glycine was then added with a molar ratio of glycine/nitrate ions equal to 1:1. The glass beaker with the precursor glycine–nitrate solution was heated on a hot plate with spontaneous burning, which resulted in a white powder. Dense samples were formed at a temperature range of 1400–1550 °C for 6 h at each stage [106]. A similar method was used in [107] for the synthesis of $\text{La}_{0.9}\text{Sr}_{0.1}\text{Ga}_{0.8}\text{Mg}_{0.2}\text{O}_{3-\delta}$. The experimental procedure included the heating of the precursor glycine–nitrate solution at 550 °C upon combustion, initial calcination of voluminous oxide powders at 800 °C for 3 h, annealing the powders at 1000 °C and final annealing at 1300 °C for 2 h. It should be noted that the authors of [107] could not achieve single-phase sample. Huang and Goodenough also concluded that a $\text{La}_{0.8}\text{Sr}_{0.2}\text{Ga}_{0.83}\text{Mg}_{0.17}\text{O}_{3-\delta}$ single-phase material cannot be formed via hydrothermal treatment synthesis [100]. A typical diagram of $\text{La}_{1-x}\text{Sr}_x\text{Ga}_{1-y}\text{Mg}_y\text{O}_{3-\delta}$ synthesis via the glycine–nitrate combustion method described in [99] is presented in Figure 5c.

In [110], Ishikawa et al., prepared $\text{La}_{0.9}\text{Sr}_{0.1}\text{Ga}_{0.8}\text{Mg}_{0.2}\text{O}_{3-\delta}$ and $\text{La}_{0.9}\text{Sr}_{0.1}\text{Ga}_{0.7}\text{Mg}_{0.3}\text{O}_{3-\delta}$ samples via self-propagating high-temperature synthesis from La_2O_3 , SrCO_3 , Ga_2O_3 , Mg and NaClO_4 . An initial powder mixture was supplied to a self-propagating synthesis reactor: it was then ignited with a disposable carbon foil in contact with the sample. The obtained powders were washed with water to remove NaCl . The samples were pressed into disks in vacuum and then sintered at a temperature range of 1000–1500 °C for 6 h in air. An alternative process for $\text{La}_{0.9}\text{Sr}_{0.1}\text{Ga}_{0.8}\text{Mg}_{0.2}\text{O}_{3-\delta}$ synthesis based on a preliminarily mechanically activated powder mixture was proposed by Ishikawa et al. [111]. The initial mixture was grinded in a planetary mill with stainless steel balls. The powder sample was pressed into a disk, which was placed in a self-propagating synthesis reactor: the aforementioned algorithm [110] was then used.

The literature points out that temperature of about 1400 °C (or more) is required for the synthesis of single-phase LSGM samples. Figure 5d presents the thermal evolution of the XRD pattern for a $\text{La}_{0.8}\text{Sr}_{0.2}\text{Ga}_{0.83}\text{Mg}_{0.17}\text{O}_{3-\delta}$ precursor powder [100]. The powders calcined at the intermediate temperatures were multiphase, containing $\text{La}_{0.8}\text{Sr}_{0.2}\text{Ga}_{0.83}\text{Mg}_{0.17}\text{O}_{3-\delta}$ and La_2O_3 , $\text{LaSrGa}_3\text{O}_7$ and $\text{La}_2\text{O}_2\text{CO}_3$ impurities. A single-phase $\text{La}_{0.8}\text{Sr}_{0.2}\text{Ga}_{0.83}\text{Mg}_{0.17}\text{O}_{3-\delta}$ sample with a cubic structure was formed during calcination at 1400 °C.

It is worth noting that the crystal structure of the obtained LSGM samples depends on the strontium and manganese dopant contents. Basic LaGaO_3 at room temperature has an orthorhombic structure [113] but varying the doping contents can change the crystal structure symmetry [100,114]. Generally, the substitution of La^{3+} -ions with Sr^{2+} -ions increases the tolerance factor t (Equation (1)), while Ga-with-Mg substitution decreases it. Therefore, the t factor for $\text{La}_{1-x}\text{Sr}_x\text{Ga}_{1-y}\text{Mg}_y\text{O}_{3-\delta}$ is nearly equal to that calculated for undoped LaGaO_3 .

The t factor is equal to 1 for $\text{La}_{0.8}\text{Sr}_{0.2}\text{Ga}_{0.8}\text{Mg}_{0.2}\text{O}_{3-\delta}$, which exhibits an ideal $Pm\bar{3}m$ cubic structure with a unit cell parameter of $a = 3.9146(1)$ Å [114] (Figure 6a). According to [114], the crystal structure of $\text{La}_{0.9}\text{Sr}_{0.1}\text{Ga}_{0.8}\text{Mg}_{0.2}\text{O}_{3-\delta}$ and $\text{La}_{0.9}\text{Sr}_{0.1}\text{Ga}_{0.9}\text{Mg}_{0.1}\text{O}_{3-\delta}$ samples (Figure 5a) was refined in a $I2/a$ monoclinic space group.

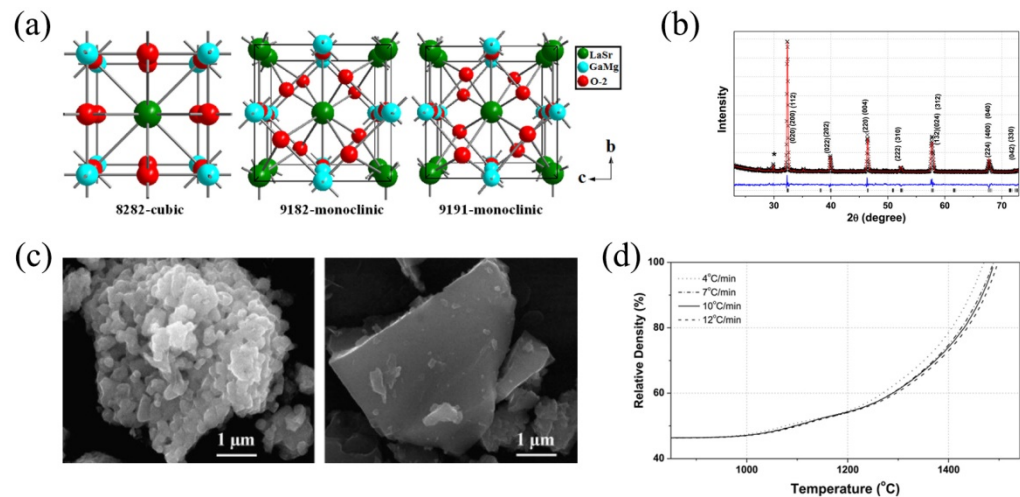


Figure 6. Properties of LaGaO_3 -based phases: (a) the crystal structure of $\text{La}_{0.8}\text{Sr}_{0.2}\text{Ga}_{0.8}\text{Mg}_{0.2}\text{O}_{3-\delta}$ (8282), $\text{La}_{0.9}\text{Sr}_{0.1}\text{Ga}_{0.8}\text{Mg}_{0.2}\text{O}_{3-\delta}$ (9182) and $\text{La}_{0.9}\text{Sr}_{0.1}\text{Ga}_{0.9}\text{Mg}_{0.1}\text{O}_{3-\delta}$ (9191). Reproduced from [114] with permission from John Wiley & Sons, Inc., 2021; (b) observed and Rietveld-refined XRD patterns of $\text{La}_{0.9}\text{Sr}_{0.1}\text{Ga}_{0.8}\text{Mg}_{0.2}\text{O}_{3-\delta}$. Reproduced from [115] with permission by Elsevier Ltd., 2018; (c) an SEM micrograph of a $\text{La}_{0.9}\text{Sr}_{0.1}\text{Ga}_{0.8}\text{Mg}_{0.2}\text{O}_{3-\delta}$ ceramic obtained via mechanically activated and conventional self-propagating synthesis. Reproduced from [111] with permission by Elsevier Ltd., 2009; (d) the temperature dependencies of the relative density of a $\text{La}_{0.9}\text{Sr}_{0.1}\text{Ga}_{0.8}\text{Mg}_{0.2}\text{O}_{3-\delta}$ ceramic material. Reproduced from [115] with permission from Elsevier Ltd., 2018.

The crystal structure of LaGaO_3 and $\text{La}_{0.9}\text{Sr}_{0.1}\text{Ga}_{0.8}\text{Mg}_{0.2}\text{O}_{3-\delta}$ samples was investigated via powder neutron diffraction at 25, 800 and 1000 °C in [116]. According to the Rietveld refinement analysis of the diffraction data collected at 25 °C, an orthorhombic structure was observed for both samples: fitting was provided in the $Pnma$ space group for LaGaO_3 (unit cell parameters were equal to $a = 5.4908(1)$, $b = 7.7925(1)$ and $c = 5.5227(1)$ Å) and in the $Imma$ space group for $\text{La}_{0.9}\text{Sr}_{0.1}\text{Ga}_{0.8}\text{Mg}_{0.2}\text{O}_{3-\delta}$ (unit cell parameters were equal to $a = 5.5179(1)$, $b = 7.8200(1)$ and $c = 5.5394(1)$ Å). The high temperature measurements [116] show that the LaGaO_3 sample possessed a rhombohedral structure in the $R\bar{3}c$ space group (unit cell parameters were equal to $a = 5.5899(1)$ Å and $a = 5.5987(1)$ Å at 800 and 1000 °C, correspondingly), whereas $\text{La}_{0.9}\text{Sr}_{0.1}\text{Ga}_{0.8}\text{Mg}_{0.2}\text{O}_{3-\delta}$ exhibits a cubic structure in the $Pm\bar{3}m$ space group (unit cell parameters were equal to $a = 3.9760(1)$ Å and $a = 3.9866(1)$ Å at 800 and 1000 °C, correspondingly). Similar data at 25 °C (the $Imma$ space group, $a = 5.5056(9)$, $b = 7.8241(7)$, $c = 5.5387(5)$ Å) for a $\text{La}_{0.9}\text{Sr}_{0.1}\text{Ga}_{0.8}\text{Mg}_{0.2}\text{O}_{3-\delta}$

sample obtained via solid-state route and sintered at 1350 °C for 2 h was reported in [115]. However, this sample consisted of an LSGM phase and a LaSrGa₃O₇ impurity phase, as indicated by '*' in Figure 6b. This fact proves the necessity of sintering temperatures of 1400 °C for obtaining single-phase LSGM samples.

Comparative analysis of the microstructural parameters for La_{0.9}Sr_{0.1}Ga_{0.8}Mg_{0.2}O_{3-δ} disks sintered at 1400 °C for 6 h obtained via the self-propagating high-temperature and solid-reaction synthesis techniques showed that the first sample was denser [110]. The relative densities of the samples were 98 and 92%, respectively, despite the fact that the sintering temperature for the first disk was 100 °C lower than that for the second one. Images in Figure 6c show the SEM micrographs of La_{0.9}Sr_{0.1}Ga_{0.8}Mg_{0.2}O_{3-δ} samples obtained via self-propagating synthesis with and without mechanical activation of the starting mixture for 24 h [111]. These SEM images testify that mechanically activated self-propagating synthesis provided the high-grade powders with nano-size particles. The specific surface areas of the samples were 3.36 and 2.06 m² g⁻¹, respectively. Based on both studies, Ishikawa et al. [110,111] concluded that this proved the advantages of using self-propagating high-temperature synthesis (especially with mechanical activation of the starting mixture) in comparison with the solid-reaction method.

The evolution of a La_{0.9}Sr_{0.1}Ga_{0.8}Mg_{0.2}O_{3-δ} sample's density against temperature was provided in by Batista et al. [115]. Based on dilatometry experimental results (Figure 6d), the authors separated the process into three steps: an insignificant increase of relative density at 25–1000 °C; gradual densification at 1000–1300 °C; and, finally, a fast densification above 1300 °C. According to [117], a relative density of over 99% was achieved after calcination at 1450 °C for 6 h.

Summing up the review section, which was devoted to the synthesis methods of Sr, Mg-doped LaGaO₃ oxides as electrolyte materials, the self-propagating high-temperature synthesis with mechanical activation of the starting mixtures can be identified as one of the most optimal techniques. The above-mentioned method can obtain the single-phase La_{0.9}Sr_{0.1}Ga_{0.8}Mg_{0.2}O_{3-δ} powders with high specific surface areas, a narrow distribution of nano-size particles, and high relative densities for the sintered ceramic samples.

3.2. Functional Properties

In 1994, Ishihara et al. [51] were the first to show that the La-substitution of LaGaO₃ with strontium and gallium with magnesium increased the electrical conductivity of doped materials (Figure 7a,b) owing to the formation of oxygen vacancies in La_{1-x}Sr_xGa_{1-y}Mg_yO_{3-δ} [118].

The measurements of Ishihara [51], Stevenson [119] and Goodenough [95] demonstrate that the La_{1-x}Sr_xGa_{1-y}Mg_yO_{3-δ} samples possess maximal electrical conductivity values at $x = 0.15/0.2$ and $y = 0.2$, as can be seen in Table 2. It should be also noted that conductivity of nominally similar materials can be varied over a wide range (see Figure A2). This confirms that the microstructural parameters of ceramics, as well as the presence of insulating impurity phases, considerably affect the transport properties of gallates, encouraging the continuous search for their new synthesis and fabricating techniques.

Hayashi et al. [120] concluded that the electrical conductivity of La_{1-x}Sr_xGa_{1-y}Mg_yO_{3-δ} becomes greater when approaching the tolerance factor of the doped sample to t for LaGaO₃ and decreases when the tolerance factor for the doped samples differed from t for LaGaO₃. It was established that increasing the Sr, Mg-doping levels led to the association of oxygen vacancies [51,119,120]; for this reason, further electrical investigations of the doped-LaGaO₃ oxides were performed on La_{1-x}Sr_xGa_{1-y}Mg_yO_{3-δ} samples with a fixed content of Sr and Mg dopants (nearly 20 mol.%, i.e., $x = y = 0.2$). The literature on the transport properties of La_{1-x}Sr_xGa_{1-y}Mg_yO_{3-δ} ceramic samples is summarised in Table 2. Figure 7c presents the temperature dependencies of conductivity for the La_{0.9}Sr_{0.1}Ga_{0.9}Mg_{0.1}O_{3-δ} (LSGM9191), La_{0.9}Sr_{0.1}Ga_{0.8}Mg_{0.2}O_{3-δ} (LSGM9182) and La_{0.8}Sr_{0.2}Ga_{0.8}Mg_{0.2}O_{3-δ} (LSGM8282) samples obtained in [114]. These data agree with the conclusion that the maximal conductivity for LSGM is achieved at $x = y = 0.2$.

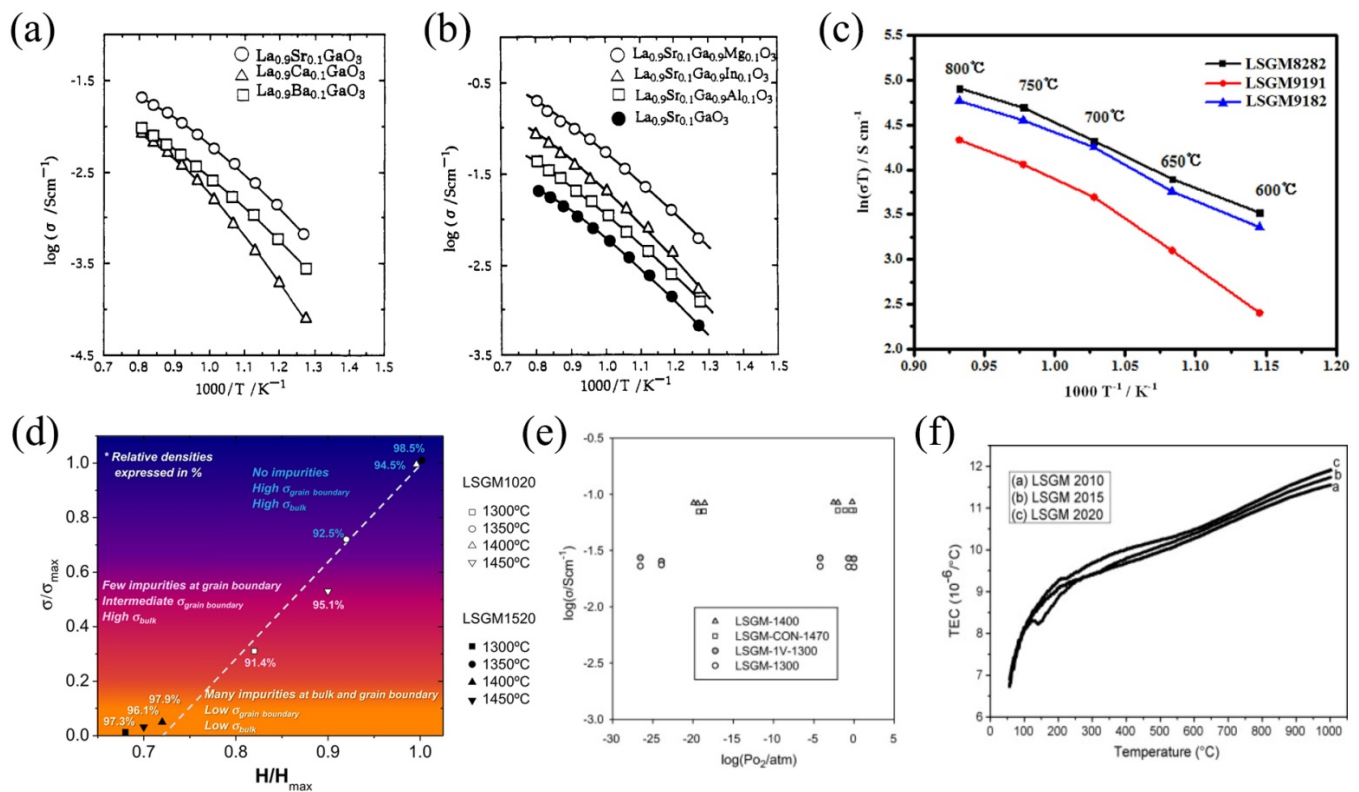


Figure 7. Properties of LaGaO₃-based phases: (a) the crystal structure of La_{0.8}Sr_{0.2}Ga_{0.8}Mg_{0.2}O_{3-δ} (8282), La_{0.9}Sr_{0.1}Ga_{0.8}Mg_{0.2}O_{3-δ} (9182) and La_{0.9}Sr_{0.1}Ga_{0.9}Mg_{0.1}O_{3-δ} (9191). Reproduced from [114] with permission from John Wiley & Sons, Inc., 2021; (b) observed and Rietveld-refined XRD patterns of La_{0.9}Sr_{0.1}Ga_{0.8}Mg_{0.2}O_{3-δ}. Reproduced from [115] with permission from Elsevier Ltd., 2018; (c) an SEM micrograph of a La_{0.9}Sr_{0.1}Ga_{0.8}Mg_{0.2}O_{3-δ} ceramic obtained via mechanically activated and conventional self-propagating synthesis. Reproduced from [111] with permission by Elsevier Ltd., 2009; (d) the temperature dependencies of the relative density of a La_{0.9}Sr_{0.1}Ga_{0.8}Mg_{0.2}O_{3-δ} ceramic material. Reproduced from [115] with permission from Elsevier Ltd., 2018; (e) conductivity of La_{0.8}Sr_{0.2}Ga_{0.8}Mg_{0.2}O_{3-δ} as a function of oxygen partial pressure. Reproduced from [109] with permission from Elsevier Ltd., 2011; (f) the temperature dependencies of TEC for La_{0.8}Sr_{0.2}Ga_{0.9}Mg_{0.1}O_{3-δ} (LSGM2010), La_{0.8}Sr_{0.2}Ga_{0.85}Mg_{0.15}O_{3-δ} (LSGM2015) and La_{0.8}Sr_{0.2}Ga_{0.8}Mg_{0.2}O_{3-δ} (LSGM2020). Reproduced from [121] with permission from Elsevier Ltd., 2009.

Table 2. Total conductivities of LaGaO₃-based materials depending on their compositions, preparation methods and temperatures. Figure A2 provides a visualization of these data.

Sample	Samples Obtaining Method; Annealing Temperature (°C)	T (°C)	σ (S cm ⁻¹)	Ref.
LaGaO ₃	Solid-state route; 1500	950	0.02	[51]
La _{0.9} Sr _{0.1} Ga _{0.9} Mg _{0.1} O _{3-δ}	Solid-state route; 1500	950	0.20	[51]
La _{0.9} Sr _{0.1} Ga _{0.85} Mg _{0.15} O _{3-δ}	Solid-state route; 1500	950	0.27	[51]
La _{0.9} Sr _{0.1} Ga _{0.8} Mg _{0.2} O _{3-δ}	Solid-state route; 1500	950	0.29	[51]
La _{0.9} Sr _{0.1} Ga _{0.7} Mg _{0.3} O _{3-δ}	Solid-state route; 1500	950	0.28	[51]
La _{0.9} Sr _{0.1} Ga _{0.6} Mg _{0.4} O _{3-δ}	Solid-state route; 1500	950	0.10	[51]
La _{0.9} Sr _{0.1} Ga _{0.8} Mg _{0.2} O _{3-δ}	Glycine-combustion method; 1400	1000	0.26	[51]
La _{0.85} Sr _{0.15} Ga _{0.8} Mg _{0.2} O _{3-δ}	Glycine-combustion method; 1400	1000	0.36	[51]
La _{0.8} Sr _{0.2} Ga _{0.85} Mg _{0.15} O _{3-δ}	Glycine-combustion method; 1400	1000	0.31	[51]
La _{0.8} Sr _{0.2} Ga _{0.8} Mg _{0.2} O _{3-δ}	Glycine-combustion method; 1400	1000	0.40	[51]

Table 2. Cont.

Sample	Samples Obtaining Method; Annealing Temperature (°C)	T (°C)	σ (S cm ⁻¹)	Ref.
La _{0.9} Sr _{0.1} Ga _{0.9} Mg _{0.1} O _{3-δ}	Solid-state route; 1470	800	0.116	[95]
La _{0.9} Sr _{0.1} Ga _{0.85} Mg _{0.15} O _{3-δ}	Solid-state route; 1470	800	0.127	[95]
La _{0.9} Sr _{0.1} Ga _{0.8} Mg _{0.2} O _{3-δ}	Solid-state route; 1470	800	0.132	[95]
La _{0.9} Sr _{0.1} Ga _{0.7} Mg _{0.3} O _{3-δ}	Solid-state route; 1470	800	0.096	[95]
La _{0.85} Sr _{0.15} Ga _{0.8} Mg _{0.2} O _{3-δ}	Solid-state route; 1470	800	0.150	[95]
La _{0.8} Sr _{0.2} Ga _{0.85} Mg _{0.15} O _{3-δ}	Solid-state route; 1470	800	0.149	[95]
La _{0.8} Sr _{0.2} Ga _{0.83} Mg _{0.17} O _{3-δ}	Solid-state route; 1470	800	0.17	[95]
La _{0.8} Sr _{0.2} Ga _{0.8} Mg _{0.2} O _{3-δ}	Solid-state route; 1470	800	0.14	[95]
La _{0.7} Sr _{0.3} Ga _{0.8} Mg _{0.2} O _{3-δ}	Solid-state route; 1470	800	0.109	[95]
La _{0.9} Sr _{0.1} Ga _{0.8} Mg _{0.2} O _{3-δ}	Self-propagating high-temperature synthesis; 1500	800	0.11	[110]
La _{0.9} Sr _{0.1} Ga _{0.8} Mg _{0.2} O _{3-δ}	Carbonate co-precipitation; 1400	800	0.045	[104]
La _{0.9} Sr _{0.1} Ga _{0.9} Mg _{0.1} O _{3-δ}	Solid-state route; 1450	800	0.071	[114]
La _{0.9} Sr _{0.1} Ga _{0.8} Mg _{0.2} O _{3-δ}	Solid-state route; 1450	800	0.1095	[114]
La _{0.9} Sr _{0.1} Ga _{0.8} Mg _{0.2} O _{3-δ}	Glycine-combustion method; 1500	800	0.092	[122]
La _{0.9} Sr _{0.1} Ga _{0.8} Mg _{0.2} O _{3-δ}	Glycine-combustion method; 1400	800	0.0395	[123]
La _{0.85} Sr _{0.15} Ga _{0.85} Mg _{0.15} O _{3-δ}	Acrylamide polymerization technique; 1432	800	0.093	[124]
La _{0.85} Sr _{0.15} Ga _{0.8} Mg _{0.2} O _{3-δ}	Mechanochemical route; 1380	600	0.016	[97]
La _{0.85} Sr _{0.15} Ga _{0.8} Mg _{0.2} O _{3-δ}	Glycine-combustion method; 1300	800	0.053	[125]
La _{0.85} Sr _{0.15} Ga _{0.8} Mg _{0.2} O _{3-δ}	EDTA-combustion method; 1300	800	0.06	[125]
La _{0.85} Sr _{0.15} Ga _{0.8} Mg _{0.2} O _{3-δ}	Glycine-combustion method; 1400	800	0.096	[105]
La _{0.85} Sr _{0.15} Ga _{0.8} Mg _{0.2} O _{3-δ}	Pechini method; 1400	800	0.135	[126]
La _{0.8} Sr _{0.2} Ga _{0.8} Mg _{0.2} O _{3-δ}	Carbonate co-precipitation; 1300	600	0.014	[103]
La _{0.8} Sr _{0.2} Ga _{0.8} Mg _{0.2} O _{3-δ}	Glycine-combustion method; 1300	700	0.022	[109]
La _{0.8} Sr _{0.2} Ga _{0.8} Mg _{0.2} O _{3-δ}	Glycine-combustion method; 1400	700	0.085	[109]
La _{0.8} Sr _{0.2} Ga _{0.8} Mg _{0.2} O _{3-δ}	Spray pyrolysis; 1400	500	0.0029	[112]
La _{0.8} Sr _{0.2} Ga _{0.8} Mg _{0.2} O _{3-δ}	Solid-state route; 1450	800	0.126	[127]
La _{0.8} Sr _{0.2} Ga _{0.8} Mg _{0.2} O _{3-δ}	Solid-state route; 1400	800	0.035	[127]
La _{0.8} Sr _{0.2} Ga _{0.8} Mg _{0.2} O _{3-δ}	Hydrothermal urea hydrolysis precipitation; 1400	800	0.056	[127]
La _{0.8} Sr _{0.2} Ga _{0.8} Mg _{0.2} O _{3-δ}	Carbonate co-precipitation; 1400	800	0.137	[128]
La _{0.8} Sr _{0.2} Ga _{0.8} Mg _{0.2} O _{3-δ}	Solid-state route; 1250	727	0.019	[129]
La _{0.8} Sr _{0.2} Ga _{0.8} Mg _{0.2} O _{3-δ}	Sol-gel technique; 1300	450	2.9×10^{-4}	[130]
La _{0.8} Sr _{0.2} Ga _{0.8} Mg _{0.2} O _{3-δ}	Solid-state route; 1400	800	0.132	[131]
La _{0.8} Sr _{0.2} Ga _{0.8} Mg _{0.2} O _{3-δ}	Thin film deposited by vacuum cold spray; 200	750	0.043	[132]
La _{0.8} Sr _{0.2} Ga _{0.8} Mg _{0.2} O _{3-δ}	Step-wise current-limiting flash sintering process; 690	850	0.072	[133]

It was shown in [119] that the ion-transfer numbers were nearly equal to 1. For La_{0.9}Sr_{0.1}Ga_{0.8}Mg_{0.2}O_{3- δ} and La_{0.8}Sr_{0.2}Ga_{0.8}Mg_{0.2}O_{3- δ} ceramic samples, the oxygen-ion transference numbers were found to be equal 1 at 700–1000 °C [107], confirming the presence of electrolyte-type behaviour. Savioli and Watson [134] studied the defect structure of LaGaO₃ upon the use of various doping strategies using DFT calculations. They confirmed that Sr-, Ba-, and Mg-doping should result in the greatest improvements to the ionic conductivity of the LaGaO₃ parent phase, while the Ni²⁺-, Co²⁺-, Fe²⁺-, and Zn²⁺-doping is responsible for the generation of a mixed ionic-electronic conducting behaviour. Sr- and Mg- co-doped LaGaO₃ complex oxides are predominantly oxygen-ionic conductors, for which the electronic conductivity levels are 3–4 magnitudes lower compared to the oxygen-ionic conductivity levels [135].

According to [125], the dependence $\ln(\sigma T)$ vs. $1/T$ had a break at 700 °C for La_{0.85}Sr_{0.15}-Ga_{0.8}Mg_{0.2}O_{3- δ} , which indicates that the activation energy value of oxygen-ion conductivity at a low-temperature range was higher than that at a high-temperature range.

A linear correlation between hardness and total ionic conductivity was revealed in [126] for La_{0.9}Sr_{0.1}Ga_{0.8}Mg_{0.2}O_{3- δ} and La_{0.85}Sr_{0.15}Ga_{0.8}Mg_{0.2}O_{3- δ} samples. It was shown that the electrical and mechanical properties of La_{1-x}Sr_xGa_{1-y}Mg_yO_{3- δ} are strongly defined by microstructural peculiarities and the presence of low-conductive LaSrGaO₄ and LaSrGa₃O₇ impurity phases [123]. The LaSrGaO₄ phase exhibits a tetragonal structure K₂NiF₄-type and crystallizes in the *I4/mmm* space group; its conductivity is found to be around $2 \cdot 10^{-7}$ S cm⁻¹ at 900 °C [136]. The LaSrGa₃O₇ phase belongs to a melilitestructure

described in the $P421m$ space group; its ionic conductivity level is around $2 \cdot 10^{-6} \text{ S cm}^{-1}$ at $800 \text{ }^\circ\text{C}$ [137]. The maximum values of ionic conductivity and hardness were achieved for single-phase $\text{La}_{0.9}\text{Sr}_{0.1}\text{Ga}_{0.8}\text{Mg}_{0.2}\text{O}_{3-\delta}$ (LSGM1020) and $\text{La}_{0.85}\text{Sr}_{0.15}\text{Ga}_{0.8}\text{Mg}_{0.2}\text{O}_{3-\delta}$ (LSGM1520) samples with a high relative density, as shown in Figure 7d. With a significant amount of impurity phases at the grain boundaries, the samples exhibited a gradual decrease in hardness and the grain boundary conductivity, which resulted in a decreasing total conductivity. The data in Table 2 may also be analysed from the aforementioned perspective.

The electrical conductivity of $\text{La}_{0.8}\text{Sr}_{0.2}\text{Ga}_{0.8}\text{Mg}_{0.2}\text{O}_{3-\delta}$ was investigated over a P_{O_2} range of 10^{-27} –1 atm at $700 \text{ }^\circ\text{C}$ [109]. The results of the measurements are presented in Figure 7e for $\text{La}_{0.8}\text{Sr}_{0.2}\text{Ga}_{0.8}\text{Mg}_{0.2}\text{O}_{3-\delta}$ samples, sintered at $1470 \text{ }^\circ\text{C}$ (LSGM-CON-1400), $1400 \text{ }^\circ\text{C}$ (LSGM-1400) and $1300 \text{ }^\circ\text{C}$ (LSGM-1300), and an LSGM sample with 1 wt% V_2O_5 sintered at $1300 \text{ }^\circ\text{C}$ (LSGM-1V-1300). All these samples show an approximately constant conductivity over the measuring p_{O_2} range, implying a realization of the electrolytic conduction behaviour.

The thermal expansion of $\text{La}_{1-x}\text{Sr}_x\text{Ga}_{1-y}\text{Mg}_y\text{O}_{3-\delta}$ was studied by Baskaran et al. [138]. The TEC values measured for the $\text{La}_{0.9}\text{Sr}_{0.1}\text{Ga}_{0.8}\text{Mg}_{0.2}\text{O}_{3-\delta}$ sample were equal to $10 \times 10^{-6} \text{ K}^{-1}$ over a low-temperature range and 13.5 – $14.0 \times 10^{-6} \text{ K}^{-1}$ above $600 \text{ }^\circ\text{C}$. Lee et al. [99] reported about an average TEC of $12.1 \times 10^{-6} \text{ K}^{-1}$ for $\text{La}_{0.8}\text{Sr}_{0.2}\text{Ga}_{0.8}\text{Mg}_{0.2}\text{O}_{3-\delta}$ at a temperature range of 25 – $1000 \text{ }^\circ\text{C}$, which is close to $12.3 \times 10^{-6} \text{ K}^{-1}$ for a $\text{La}_{0.65}\text{Sr}_{0.3}\text{MnO}_{3-\delta}$ electrode at the same temperatures [92].

The expansion behaviour for $\text{La}_{1-x}\text{Sr}_x\text{Ga}_{1-y}\text{Mg}_y\text{O}_{3-\delta}$ is correlated with its crystal structure in the observed temperature range. Therefore, the presence of a phase transition from an orthorhombic phase to a cubic one for $\text{La}_{0.9}\text{Sr}_{0.1}\text{Ga}_{0.8}\text{Mg}_{0.2}\text{O}_{3-\delta}$ [116] and the existence of an ideal perovskite cubic structure for $\text{La}_{0.8}\text{Sr}_{0.2}\text{Ga}_{0.8}\text{Mg}_{0.2}\text{O}_{3-\delta}$ [114] are responsible for the aforementioned variations in their thermal expansion behaviour.

Datta et al. [121] observed that the temperature of phase transition from an orthorhombic to a rhombohedral structure for $\text{La}_{1-x}\text{Sr}_x\text{Ga}_{1-y}\text{Mg}_y\text{O}_{3-\delta}$ increased as Mg content increased at a fixed Sr content, as shown in Figure 7f, and decreased with increasing Sr content at a fixed Mg content. The effect of Sr and Mg co-doping on TEC values was explained for $\text{La}_{1-x}\text{Sr}_x\text{Ga}_{1-y}\text{Mg}_y\text{O}_{3-\delta}$ in terms of the amount of generated oxygen vacancies. It was concluded that TEC values increased as oxygen vacancies increase, regardless of the dopant type. This was the result of the binding energy weakening as a result of oxygen vacancy formation.

Shkerin et al. [139] analysed the structure and phase transitions of $\text{La}_{0.88}\text{Sr}_{0.12}\text{Ga}_{0.82}\text{Mg}_{0.18}\text{O}_{3-\delta}$ using dilatometry, XRD and Raman spectroscopy. According to the obtained data, $\text{La}_{0.88}\text{Sr}_{0.12}\text{Ga}_{0.82}\text{Mg}_{0.18}\text{O}_{3-\delta}$ exhibited two phase transitions of the second order at 502 and $607 \text{ }^\circ\text{C}$. The first transition was attributed to a phase transition from an orthorhombic phase to a cubic one, while the second phase transition was attributed to the ordering of the oxygen vacancies.

Wu et al. [140] studied transport properties of $\text{La}_{0.85}\text{Sr}_{0.15}\text{Ga}_{0.8}\text{Mg}_{0.2}\text{O}_{3-\delta}$ upon the partial or full Sr-substitution with calcium or barium. Their analyses have shown that both types of substitution result in a decrease in ionic conductivity by 20 – 30% . However, at the same time, the Ca-substituted ceramic materials showed higher conductivities compared to the Ba-substituted analogues. This confirms that strontium is an ideal dopant (from the steric and energetic viewpoints) to be introduced into the La-sublattice of LaGaO_3 -based phases.

The chemical compatibility of $\text{La}_{1-x}\text{Sr}_x\text{Ga}_{1-y}\text{Mg}_y\text{O}_{3-\delta}$ was investigated with oxide materials used in SOFCs, cathodes [141–152] and anodes [153–167]: this is presented in the corresponding reviews [28,56,153].

Chemical interactions between a $\text{La}_{0.9}\text{Sr}_{0.1}\text{Ga}_{0.8}\text{Mg}_{0.2}\text{O}_{3-\delta}$ electrolyte and cathode materials such as $\text{La}_{0.65}\text{Sr}_{0.3}\text{MnO}_{3-\delta}$, $\text{La}_{0.7}\text{Sr}_{0.3}\text{CoO}_{3-\delta}$, $\text{La}_{0.65}\text{Sr}_{0.3}\text{FeO}_{3-\delta}$, $\text{La}_{0.65}\text{Sr}_{0.3}\text{NiO}_{3-\delta}$ and $\text{La}_{0.6}\text{Sr}_{0.4}\text{Co}_{0.2}\text{Fe}_{0.8}\text{O}_{3-\delta}$ are demonstrated in [141]. The LSGM/cathode powders were mixed at a weight ratio of $1:1$, pressed into disks and annealed at $1300 \text{ }^\circ\text{C}$ for 3 h in air. The XRD data revealed that impurity phases were not formed in the LSGM mixed with

$\text{La}_{0.65}\text{Sr}_{0.3}\text{MnO}_{3-\delta}$, $\text{La}_{0.7}\text{Sr}_{0.3}\text{CoO}_{3-\delta}$, and $\text{La}_{0.65}\text{Sr}_{0.3}\text{FeO}_{3-\delta}$, but appear in the calcined mixtures with $\text{La}_{0.65}\text{Sr}_{0.3}\text{NiO}_{3-\delta}$ and $\text{La}_{0.6}\text{Sr}_{0.4}\text{Co}_{0.2}\text{Fe}_{0.8}\text{O}_{3-\delta}$. The absence of reactivity between $\text{La}_{0.8}\text{Sr}_{0.2}\text{Ga}_{0.8}\text{Mg}_{0.2}\text{O}_{3-\delta}$ and $\text{La}_{0.8}\text{Sr}_{0.2}\text{MnO}_{3-\delta}$ was also confirmed during calcination at 800 °C [142].

Sydyknazar et al. [143] showed that $\text{La}_{0.83}\text{Sr}_{0.17}\text{Ga}_{0.8}\text{Mg}_{0.2}\text{O}_{3-\delta}$ exhibited good chemical compatibility with a novel cathode material, $\text{Sr}_{0.9}\text{Ba}_{0.1}\text{Co}_{0.95}\text{Ru}_{0.05}\text{O}_{3-\delta}$, after joint calcination at 1100 °C for 12 h. According to the literature, $\text{La}_{0.9}\text{Sr}_{0.1}\text{Ga}_{0.8}\text{Mg}_{0.2}\text{O}_{3-\delta}$ does not react with the following cathodes: $\text{La}_{0.4}\text{Sr}_{0.6}\text{Co}_{0.9}\text{Sb}_{0.1}\text{O}_{3-\delta}$ after heat treatment at 1150 °C for 6 h [144], $\text{SrCo}_{0.8}\text{Fe}_{0.1}\text{Nb}_{0.1}\text{O}_{3-\delta}$ at 950 °C for 10 h [145], $\text{BaCo}_{0.7}\text{Fe}_{0.2}\text{Ta}_{0.1}\text{O}_{3-\delta}$ at 950 °C for 10 h [146] and $\text{Sr}_2\text{Ti}_{0.8}\text{Co}_{0.2}\text{FeO}_{6-\delta}$ after at 950 °C for 10 h [147]. According to Tarancón et al. [148], $\text{La}_{0.8}\text{Sr}_{0.2}\text{Ga}_{0.8}\text{Mg}_{0.2}\text{O}_{3-\delta}$ interacted with a $\text{GdBaCo}_2\text{O}_{5+\delta}$ cathode at temperatures above 900 °C, forming $\text{BaLaGa}_3\text{O}_4$ and $\text{BaLaGa}_3\text{O}_7$ secondary phases.

An analysis of works devoted to Ruddlesden–Popper phases demonstrates that $\text{La}_{0.9}\text{Sr}_{0.1}\text{Ga}_{0.8}\text{Mg}_{0.2}\text{O}_{3-\delta}$ and $\text{Pr}_{2-x}\text{La}_x\text{Ni}_{0.85}\text{Cu}_{0.1}\text{Al}_{0.05}\text{O}_{4+\delta}$ ($x = 0, 0.2, 0.5, 1.0$) have no interactions at 1000 °C for 5 h [149], but $\text{La}_{0.95}\text{Sr}_{0.05}\text{Ga}_{0.9}\text{Mg}_{0.1}\text{O}_{3-\delta}$ reacted with $\text{Nd}_2\text{NiO}_{4+\delta}$ after annealing at 1000 °C for 5 h [150]. Equally, $\text{La}_{0.85}\text{Sr}_{0.15}\text{Ga}_{0.85}\text{Mg}_{0.15}\text{O}_{3-\delta}$ reacted with $\text{Pr}_{2-x}\text{Ca}_x\text{NiO}_{4+\delta}$ after annealing at 900 °C for 10 h ($x = 0, 0.5$) [151] and at 1200 °C for 1 h ($x = 0, 0.3$) [152].

Zhang et al. [154] showed that a $\text{La}_{0.9}\text{Sr}_{0.1}\text{Ga}_{0.8}\text{Mg}_{0.2}\text{O}_{3-\delta}$ electrolyte reacted with the nickel component in a Ni-SDC anode. The chemical interaction between LSGM and the composite was due to the interface diffusion of nickel from the anode to the LSGM electrolyte; this led to the formation of La-based poor-conductive secondary phases, which block oxygen-ion transport. The unit cell design with a buffer layer of SDC was suggested as an effective way of avoiding the problem of interface diffusion [155]. However, chemical reactivity was observed between $\text{La}_{1-x}\text{Sr}_x\text{Ga}_{1-y}\text{Mg}_y\text{O}_{3-\delta}$ and buffer layers of $\text{Gd}_{0.1}\text{Ce}_{0.9}\text{O}_{1.95}$, scandia-doped zirconia [156] and $\text{Gd}_{0.8}\text{Ce}_{0.2}\text{O}_{1.9}$ [157].

An alternate solution to the problem of nickel interface diffusion from a Ni-based anode is to find novel anode materials. A study of the chemical compatibility between $\text{La}_{0.9}\text{Sr}_{0.1}\text{Ga}_{0.8}\text{Mg}_{0.2}\text{O}_{3-\delta}$ and Fe_2O_3 , Co_2O_3 , NiO as anode materials is provided in [158]. Powder mixtures of LSGM with metal oxides at a weight ratio of 1:1 were mixed in ethanol, pressed into pellets and annealed at 1150, 1250 and 1350 °C for 2 h. The obtained XRD data showed that the LSGM reacted with NiO and Co_2O_3 at 1150 °C, while a detectable reaction with Fe_2O_3 occurred only after calcination at 1350 °C.

Du and Sammes [159] reported good chemical compatibility between $\text{La}_{0.8}\text{Sr}_{0.2}\text{Ga}_{0.8}\text{Mg}_{0.2}\text{O}_{3-\delta}$ and an alternative $\text{La}_{0.75}\text{Sr}_{0.25}\text{Cr}_{0.5}\text{Mn}_{0.5}\text{O}_3$ anode at a temperature range of 1100–1500 °C. However, the authors note that a low-conductivity phase formed if the annealing time was more than 6 h or the annealing temperature was greater than 1500 °C.

Good chemical compatibility between LSGM and anodes with a double perovskite structure was shown for: $\text{La}_{0.9}\text{Sr}_{0.1}\text{Ga}_{0.8}\text{Mg}_{0.2}\text{O}_{3-\delta}$ and $\text{Sr}_2\text{TiMoO}_{6-\delta}$ after calcining the samples at 1000 °C for 10 h in an atmosphere of 5% H_2/Ar [160], $\text{La}_{0.8}\text{Sr}_{0.2}\text{Ga}_{0.8}\text{Mg}_{0.2}\text{O}_{3-\delta}$ and $\text{Sr}_2\text{Fe}_{1.5}\text{Mo}_{0.5}\text{O}_{6-\delta}$ after heat treatment at 1200 °C for 24 h in air [161], $\text{La}_{0.88}\text{Sr}_{0.12}\text{Ga}_{0.82}\text{Mg}_{0.18}\text{O}_{3-\delta}$ with $\text{Sr}_2\text{NiMoO}_{6-\delta}$ at 1000 °C for 20 h [162,163] and $\text{Sr}_2\text{Ni}_{0.75}\text{Mg}_{0.25}\text{MoO}_{6-\delta}$ at 1100 °C for 20 h [164] and at 1250 °C for 2 h [163]. The formation of secondary phases between LSGM and double perovskite anodes was observed for $\text{La}_{0.9}\text{Sr}_{0.1}\text{Ga}_{0.8}\text{Mg}_{0.2}\text{O}_{3-\delta}$ and $\text{Sr}_2\text{MgMoO}_{6-\delta}$ after calcining at 1100 °C [165], for $\text{La}_{0.88}\text{Sr}_{0.12}\text{Ga}_{0.82}\text{Mg}_{0.18}\text{O}_{3-\delta}$ and $\text{Sr}_2\text{ZnMoO}_6$ at 1000 °C for 20 h [166] and for $\text{La}_{0.8}\text{Sr}_{0.2}\text{Ga}_{0.8}\text{Mg}_{0.2}\text{O}_{3-\delta}$ at 1300 °C for 10 h with $\text{Sr}_2\text{Ni}_{0.7}\text{Mg}_{0.3}\text{MoO}_{6-\delta}$ [167] and, after heat treatment at 1200 °C for 24 h, with $\text{Sr}_2\text{CoMoO}_{6-\delta}$ [161], $\text{Sr}_2\text{NiMoO}_{6-\delta}$ [161] and $\text{Sr}_2\text{MgMoO}_{6-\delta}$ [168].

According to Takano et al. [165], $\text{La}_{0.9}\text{Sr}_{0.1}\text{Ga}_{0.8}\text{Mg}_{0.2}\text{O}_{3-\delta}$ did not react with $\text{Ce}_{0.8}\text{La}_{0.2}\text{O}_{1.8}$ after annealing at 1300 °C for 1 h; therefore, it was concluded that $\text{La}_{0.9}\text{Sr}_{0.1}\text{Ga}_{0.8}\text{Mg}_{0.2}\text{O}_{3-\delta}$ and $\text{Ce}_{0.8}\text{La}_{0.2}\text{O}_{1.8}$ might be recommended as SOFC electrolyte and buffer materials, respectively, with $\text{Sr}_2\text{MgMoO}_{6-\delta}$ used as the anode material. However, a comprehensive investigation of the chemical compatibility between various compositions of $\text{La}_{1-x}\text{Sr}_x\text{Ga}_{1-y}\text{Mg}_y\text{O}_{3-\delta}$ and lanthanum-doped CeO_2 , provided in [169], showed that only a $\text{La}_{0.9}\text{Sr}_{0.1}\text{Ga}_{0.8}\text{Mg}_{0.2}\text{O}_{3-\delta}/$

$\text{Ce}_{0.6}\text{La}_{0.4}\text{O}_{2-\delta}$ mixture did not result in additional phases after being annealed twice at 1350 °C for 2 h at each stage.

3.3. Applications in SOFCs

The problem of reactivity between the LSGM and SOFC electrode materials during sintering can be solved by reducing sintering temperatures or/and using the SDC buffer layer as a barrier, eliminating lanthanum- and nickel-cation diffusion. Several unit cell designs have been proposed in the literature. Table 3 presents a summary of electrochemical performances for different types of hydrogen-fuelled SOFCs with LSGM-based electrolytes. These data testify that enhanced power densities were achieved for electrolyte-supported SOFCs when the LSGM electrolyte thickness was in a range of 100–300 μm . Buffer layers of doped ceria were used between the electrolyte and anode: $\text{Ce}_{0.8}\text{Sm}_{0.2}\text{O}_{2-\delta}$ [144,145,149,155,160,167], $\text{Ce}_{0.8}\text{Gd}_{0.2}\text{O}_{2-\delta}$ [170] and $\text{Ce}_{0.6}\text{La}_{0.4}\text{O}_{2-\delta}$ [171,172].

Table 3. The performances of SOFCs with $\text{La}_{1-x}\text{Sr}_x\text{Ga}_{1-y}\text{Mg}_y\text{O}_{3-\delta}$ electrolytes. Figure A3 provides a visualization of these data.

Anode	Buffer Layer/ Electrolyte (Thickness, μm)/ Buffer Layer	Cathode	T (°C)	Power Density (mW cm^{-2})	Ref.
Ni- $\text{Ce}_{0.8}\text{Sm}_{0.2}\text{O}_{2-\delta}$	$\text{La}_{0.8}\text{Sr}_{0.2}\text{Ga}_{0.83}\text{Mg}_{0.17}\text{O}_{3-\delta}$ (265)	$\text{La}_{0.6}\text{Sr}_{0.4}\text{O}_{3-\delta}$	800	290	[52]
Ni- $\text{La}_{0.8}\text{Sr}_{0.2}\text{Ga}_{0.83}\text{Mg}_{0.17}\text{O}_{2.815}$	$\text{La}_{0.8}\text{Sr}_{0.2}\text{Ga}_{0.83}\text{Mg}_{0.17}\text{O}_{3-\delta}$ (395)	$\text{La}_{0.6}\text{Sr}_{0.4}\text{O}_{3-\delta}$	800	363	[52]
Ni- $\text{Ce}_{0.8}\text{Sm}_{0.2}\text{O}_{2-\delta}$	$\text{Ce}_{0.8}\text{Sm}_{0.2}\text{O}_{2-\delta} / \text{La}_{0.9}\text{Sr}_{0.1}\text{Ga}_{0.8}\text{Mg}_{0.2}\text{O}_{3-\delta}$ (300)	$\text{La}_{0.4}\text{Sr}_{0.6}\text{Co}_{0.9}\text{Sb}_{0.1}\text{O}_{3-\delta}$ - $\text{Ce}_{0.8}\text{Sm}_{0.2}\text{O}_{2-\delta}$	700	432	[144]
Ni- $\text{Ce}_{0.8}\text{Sm}_{0.2}\text{O}_{2-\delta}$	$\text{Ce}_{0.8}\text{Sm}_{0.2}\text{O}_{2-\delta} / \text{La}_{0.9}\text{Sr}_{0.1}\text{Ga}_{0.8}\text{Mg}_{0.2}\text{O}_{3-\delta}$ (100)	$\text{SrCo}_{0.8}\text{Fe}_{0.1}\text{Nb}_{0.1}\text{O}_{3-\delta}$	800	756	[145]
Ni- $\text{Ce}_{0.8}\text{Sm}_{0.2}\text{O}_{2-\delta}$	$\text{Ce}_{0.8}\text{Sm}_{0.2}\text{O}_{2-\delta} / \text{La}_{0.9}\text{Sr}_{0.1}\text{Ga}_{0.8}\text{Mg}_{0.2}\text{O}_{3-\delta}$ (100)	$\text{SrCo}_{0.8}\text{Fe}_{0.1}\text{Nb}_{0.1}\text{O}_{3-\delta}$ - $\text{Ce}_{0.9}\text{Gd}_{0.1}\text{O}_{2-\delta}$	800	829	[145]
Ni- $\text{Ce}_{0.8}\text{Sm}_{0.2}\text{O}_{2-\delta}$	$\text{La}_{0.9}\text{Sr}_{0.1}\text{Ga}_{0.8}\text{Mg}_{0.2}\text{O}_{3-\delta}$ (300)	$\text{BaCo}_{0.7}\text{Fe}_{0.2}\text{Ta}_{0.1}\text{O}_{3-\delta}$	800	460	[146]
Ni- $\text{Ce}_{0.8}\text{Sm}_{0.2}\text{O}_{2-\delta}$	$\text{Ce}_{0.8}\text{Sm}_{0.2}\text{O}_{2-\delta} / \text{La}_{0.9}\text{Sr}_{0.1}\text{Ga}_{0.8}\text{Mg}_{0.2}\text{O}_{3-\delta}$ (300)	$\text{Pr}_2\text{Ni}_{0.85}\text{Cu}_{0.1}\text{Al}_{0.05}\text{O}_{4+\delta}$	700	392	[149]
Ni- $\text{Ce}_{0.8}\text{Sm}_{0.2}\text{O}_{2-\delta}$	$\text{La}_{0.8}\text{Sr}_{0.2}\text{Ga}_{0.83}\text{Mg}_{0.17}\text{O}_{3-\delta}$ (500)	$\text{La}_{0.6}\text{Sr}_{0.4}\text{O}_{3-\delta}$	800	270	[155, 173]
Ni- $\text{Ce}_{0.8}\text{Sm}_{0.2}\text{O}_{2-\delta}$	$\text{Ce}_{0.8}\text{Sm}_{0.2}\text{O}_{2-\delta} / \text{La}_{0.8}\text{Sr}_{0.2}\text{Ga}_{0.83}\text{Mg}_{0.17}\text{O}_{3-\delta}$ (500)	$\text{La}_{0.6}\text{Sr}_{0.4}\text{O}_{3-\delta}$	800	550	[155, 173]
Ni- $\text{Ce}_{0.8}\text{Sm}_{0.2}\text{O}_{2-\delta}$	$\text{La}_{0.87}\text{Sr}_{0.13}\text{Ga}_{0.85}\text{Mg}_{0.15}\text{O}_{3-\delta}$ (3.8)	$\text{La}_{0.87}\text{Sr}_{0.13}\text{Ga}_{0.85}\text{Mg}_{0.15}\text{O}_{3-\delta}$	750	1420	[174]
Ni- $\text{Ce}_{0.8}\text{Y}_{0.2}\text{O}_{2-\delta}$	$\text{La}_{0.9}\text{Sr}_{0.1}\text{Ga}_{0.8}\text{Mg}_{0.2}\text{O}_{3-\delta}$ (45)	$\text{La}_{0.6}\text{Sr}_{0.4}\text{Fe}_{0.8}\text{Co}_{0.2}\text{O}_{3-\delta}$	700	500	[175]
Ni- $\text{Ce}_{0.6}\text{La}_{0.4}\text{O}_{2-\delta}$	$\text{La}_{0.8}\text{Sr}_{0.2}\text{Ga}_{0.8}\text{Mg}_{0.2}\text{O}_{3-\delta}$ (30)	$\text{La}_{0.6}\text{Sr}_{0.4}\text{Fe}_{0.8}\text{Co}_{0.2}\text{O}_{3-\delta}$	700	780	[176]
Ni- $\text{Ce}_{0.6}\text{La}_{0.4}\text{O}_{2-\delta}$	$\text{Ce}_{0.6}\text{La}_{0.4}\text{O}_{2-\delta} / \text{La}_{0.8}\text{Sr}_{0.2}\text{Ga}_{0.83}\text{Mg}_{0.17}\text{O}_{3-\delta}$ (500)	$\text{SrCo}_{0.8}\text{Fe}_{0.2}\text{O}_{3-\delta}$	800	900	[177]
Ni- $\text{Ce}_{0.9}\text{Gd}_{0.1}\text{O}_{2-\delta}$	$\text{Ce}_{0.55}\text{La}_{0.45}\text{O}_{2-\delta} / \text{La}_{0.9}\text{Sr}_{0.1}\text{Ga}_{0.8}\text{Mg}_{0.2}\text{O}_{3-\delta}$ (75)	$\text{La}_{0.9}\text{Sr}_{0.1}\text{O}_{3-\delta}$ - $\text{Ce}_{0.55}\text{La}_{0.45}\text{O}_{2-\delta}$	800	1100	[178]
Ni- $\text{Ce}_{0.9}\text{Gd}_{0.1}\text{O}_{2-\delta}$	$\text{Ce}_{0.55}\text{La}_{0.45}\text{O}_{2-\delta} / \text{La}_{0.9}\text{Sr}_{0.1}\text{Ga}_{0.8}\text{Mg}_{0.2}\text{O}_{3-\delta}$ (50)	$\text{La}_{0.6}\text{Sr}_{0.4}\text{O}_{3-\delta}$	800	1565	[179]
Ni- $\text{Ce}_{0.9}\text{Gd}_{0.1}\text{O}_{2-\delta}$	$\text{Ce}_{0.55}\text{La}_{0.45}\text{O}_{2-\delta} / \text{La}_{0.9}\text{Sr}_{0.1}\text{Ga}_{0.8}\text{Mg}_{0.2}\text{O}_{3-\delta}$ (50) / $\text{Ce}_{0.55}\text{La}_{0.45}\text{O}_{2-\delta}$	$\text{La}_{0.6}\text{Sr}_{0.4}\text{O}_{3-\delta}$	800	871	[179]
Ni- $\text{Ce}_{0.8}\text{Gd}_{0.2}\text{O}_{2-\delta}$	$\text{Ce}_{0.8}\text{Gd}_{0.2}\text{O}_{2-\delta} / \text{La}_{0.9}\text{Sr}_{0.1}\text{Ga}_{0.8}\text{Mg}_{0.2}\text{O}_{3-\delta}$ (75)	$\text{Ba}_{0.5}\text{Sr}_{0.5}\text{Co}_{0.8}\text{Fe}_{0.2}\text{O}_{3-\delta}$	700	760	[180]
Ni-Fe	$\text{Ce}_{0.8}\text{Sm}_{0.2}\text{O}_{2-\delta} / \text{La}_{0.9}\text{Sr}_{0.1}\text{Ga}_{0.8}\text{Mg}_{0.2}\text{O}_{3-\delta}$ (6)	$\text{Sm}_{0.5}\text{Sr}_{0.5}\text{O}_{3-\delta}$	700	1790	[181]
Ni- $\text{Ce}_{0.6}\text{La}_{0.4}\text{O}_{2-\delta}$	$\text{Ce}_{0.6}\text{La}_{0.4}\text{O}_{2-\delta} / \text{La}_{0.9}\text{Sr}_{0.1}\text{Ga}_{0.8}\text{Mg}_{0.2}\text{O}_{3-\delta}$ (9) / $\text{Ce}_{0.6}\text{La}_{0.4}\text{O}_{1.8}$	$\text{La}_{0.9}\text{Sr}_{0.1}\text{Ga}_{0.8}\text{Mg}_{0.2}\text{O}_{3-\delta}$ - $\text{La}_{0.6}\text{Sr}_{0.4}\text{Fe}_{0.8}\text{Co}_{0.2}\text{O}_{3-\delta}$	700	910	[182]
Ni- $\text{Ce}_{0.8}\text{Sm}_{0.2}\text{O}_{2-\delta}$	$\text{Ce}_{0.6}\text{La}_{0.4}\text{O}_{2-\delta} / \text{La}_{0.9}\text{Sr}_{0.1}\text{Ga}_{0.8}\text{Mg}_{0.2}\text{O}_{3-\delta}$ (11) / $\text{Ce}_{0.6}\text{La}_{0.4}\text{O}_{1.8}$	$\text{La}_{0.9}\text{Sr}_{0.1}\text{Ga}_{0.8}\text{Mg}_{0.2}\text{O}_{3-\delta}$ - $\text{La}_{0.6}\text{Sr}_{0.4}\text{Fe}_{0.8}\text{Co}_{0.2}\text{O}_{3-\delta}$	800	1230	[183]
Ni- $\text{Ce}_{0.8}\text{Gd}_{0.2}\text{O}_{2-\delta}$	$\text{Ce}_{0.8}\text{Gd}_{0.2}\text{O}_{2-\delta} / (\text{La}_{0.9}\text{Sr}_{0.1})_{0.97}\text{Ga}_{0.9}\text{Mg}_{0.1}\text{O}_{3-\delta}$ (120)	$\text{La}_{0.6}\text{Sr}_{0.4}\text{Fe}_{0.8}\text{Co}_{0.2}\text{O}_{3-\delta}$	800	540	[170]
Ni- $\text{Ce}_{0.8}\text{Sm}_{0.2}\text{O}_{2-\delta}$	$\text{La}_{0.9}\text{Sr}_{0.1}\text{Ga}_{0.8}\text{Mg}_{0.2}\text{O}_{3-\delta}$ (3.4)	$\text{La}_{0.9}\text{Sr}_{0.1}\text{Ga}_{0.8}\text{Mg}_{0.2}\text{O}_{3-\delta}$ - $\text{La}_{0.6}\text{Sr}_{0.4}\text{Fe}_{0.8}\text{Co}_{0.2}\text{O}_{3-\delta}$	750	736	[184]
Ni- $\text{Ce}_{0.8}\text{Gd}_{0.2}\text{O}_{2-\delta}$	$\text{La}_{0.8}\text{Sr}_{0.2}\text{Ga}_{0.8}\text{Mg}_{0.2}\text{O}_{3-\delta}$ (50)	$\text{La}_{0.6}\text{Sr}_{0.4}\text{Fe}_{0.8}\text{Co}_{0.2}\text{O}_{3-\delta}$	700	831	[185]
Ni-Fe	$\text{Ce}_{0.6}\text{La}_{0.4}\text{O}_{2-\delta} / \text{La}_{0.9}\text{Sr}_{0.1}\text{Ga}_{0.8}\text{Mg}_{0.2}\text{O}_{3-\delta}$ (200)	$\text{Sm}_{0.5}\text{Sr}_{0.5}\text{O}_{3-\delta}$	800	1350	[171]
Pd-Sr ₂ TiMoO _{6-δ}	$\text{Ce}_{0.8}\text{Sm}_{0.2}\text{O}_{2-\delta} / \text{La}_{0.9}\text{Sr}_{0.1}\text{Ga}_{0.8}\text{Mg}_{0.2}\text{O}_{3-\delta}$ (300)	$\text{NdBaCo}_{0.67}\text{Fe}_{0.67}\text{Cu}_{0.67}\text{O}_{5+\delta}$	850	1009	[160]
Sr ₂ NiMoO _{6-δ}	$\text{La}_{0.88}\text{Sr}_{0.12}\text{Ga}_{0.82}\text{Mg}_{0.18}\text{O}_{3-\delta}$ (700) / $\text{Ce}_{0.8}\text{Sm}_{0.2}\text{O}_{2-\delta}$	$\text{La}_{0.7}\text{Sr}_{0.3}\text{Fe}_{0.9}\text{Co}_{0.1}\text{O}_{3-\delta}$	800	61	[163]
Sr ₂ NiMoO _{6-δ}	$\text{La}_{0.9}\text{Sr}_{0.1}\text{Ga}_{0.8}\text{Mg}_{0.2}\text{O}_{3-\delta}$ (300)	$\text{Ba}_{0.5}\text{Sr}_{0.5}\text{Co}_{0.8}\text{Fe}_{0.2}\text{O}_{3-\delta}$	800	595	[186]
Sr ₂ MgMoO _{6-δ}	$\text{Ce}_{0.8}\text{Sm}_{0.2}\text{O}_{2-\delta} / \text{La}_{0.8}\text{Sr}_{0.2}\text{Ga}_{0.8}\text{Mg}_{0.2}\text{O}_{3-\delta}$ (700)	$\text{SmBaCo}_2\text{O}_{5+\delta}$	800	39	[167]

Table 3. Cont.

Anode	Buffer Layer/ Electrolyte (Thickness, μm)/ Buffer Layer	Cathode	T ($^{\circ}\text{C}$)	Power Density (mW cm^{-2})	Ref.
$\text{Sr}_2\text{MgMoO}_{6-\delta}$	$\text{Ce}_{0.8}\text{Gd}_{0.2}\text{O}_{2-\delta} / \text{La}_{0.8}\text{Sr}_{0.2}\text{Ga}_{0.8}\text{Mg}_{0.2}\text{O}_{3-\delta}$ (600)	$\text{La}_{0.6}\text{Sr}_{0.4}\text{Fe}_{0.8}\text{Co}_{0.2}\text{O}_{3-\delta}$	800	330	[168]
$\text{Sr}_2\text{Ni}_{0.75}\text{Mg}_{0.25}\text{MoO}_{6-\delta}$	$\text{La}_{0.88}\text{Sr}_{0.12}\text{Ga}_{0.82}\text{Mg}_{0.18}\text{O}_{3-\delta}$ (700)/ $\text{Ce}_{0.8}\text{Sm}_{0.2}\text{O}_{2-\delta}$	$\text{La}_{0.7}\text{Sr}_{0.3}\text{Fe}_{0.9}\text{Co}_{0.1}\text{O}_{3-\delta}$	800	429	[163]
$\text{Sr}_2\text{Ni}_{0.75}\text{Mg}_{0.25}\text{MoO}_{6-\delta}$	$\text{La}_{0.88}\text{Sr}_{0.12}\text{Ga}_{0.82}\text{Mg}_{0.18}\text{O}_{3-\delta}$ (500)/ $\text{Ce}_{0.8}\text{Sm}_{0.2}\text{O}_{2-\delta}$	$\text{La}_2\text{NiO}_{4+\delta}$	800	276	[187]
$\text{Sr}_2\text{Ni}_{0.75}\text{Mg}_{0.25}\text{MoO}_{6-\delta}$	$\text{La}_{0.88}\text{Sr}_{0.12}\text{Ga}_{0.82}\text{Mg}_{0.18}\text{O}_{3-\delta}$ (500)/ $\text{Ce}_{0.8}\text{Sm}_{0.2}\text{O}_{2-\delta}$	$\text{La}_{1.5}\text{Ca}_{0.5}\text{Ni}_{0.67}\text{Fe}_{0.33}\text{O}_{4+\delta}$	800	273	[187]
$\text{Sr}_2\text{Ni}_{0.7}\text{Mg}_{0.3}\text{MoO}_{6-\delta}$	$\text{Ce}_{0.8}\text{Sm}_{0.2}\text{O}_{2-\delta} / \text{La}_{0.8}\text{Sr}_{0.2}\text{Ga}_{0.8}\text{Mg}_{0.2}\text{O}_{3-\delta}$ (700)	$\text{SmBaCo}_2\text{O}_{5+\delta}$	800	160	[167]
$\text{Sr}_2\text{Ni}_{0.3}\text{Mg}_{0.7}\text{MoO}_{6-\delta}$	$\text{Ce}_{0.8}\text{Sm}_{0.2}\text{O}_{2-\delta} / \text{La}_{0.8}\text{Sr}_{0.2}\text{Ga}_{0.8}\text{Mg}_{0.2}\text{O}_{3-\delta}$ (700)	$\text{SmBaCo}_2\text{O}_{5+\delta}$	800	119	[167]
$\text{Ba}_{0.5}\text{Sr}_{0.5}\text{Mo}_{0.1}\text{Fe}_{0.9}\text{O}_{3-\delta}$	$\text{La}_{0.8}\text{Sr}_{0.2}\text{Ga}_{0.8}\text{Mg}_{0.2}\text{O}_{3-\delta}$ (150)	$\text{Ba}_{0.5}\text{Sr}_{0.5}\text{Mo}_{0.1}\text{Fe}_{0.9}\text{O}_{3-\delta}$	800	2280	[188]
$\text{SrFe}_{0.75}\text{Mo}_{0.25}\text{O}_{3-\delta}$	$\text{La}_{0.9}\text{Sr}_{0.1}\text{Ga}_{0.8}\text{Mg}_{0.2}\text{O}_{3-\delta}$ (30)	$\text{SrFe}_{0.75}\text{Mo}_{0.25}\text{O}_{3-\delta}$	800	703	[189]
$\text{PrBa}(\text{Fe}_{0.8}\text{Sc}_{0.2})_2\text{O}_{5+\delta}$	$\text{La}_{0.9}\text{Sr}_{0.1}\text{Ga}_{0.8}\text{Mg}_{0.2}\text{O}_{3-\delta}$ (275)	$\text{PrBa}(\text{Fe}_{0.8}\text{Sc}_{0.2})_2\text{O}_{5+\delta}$	800	713	[190]
$\text{Sr}_2\text{Fe}_{1.5}\text{Mo}_{0.5}\text{O}_{6-\delta}$	$\text{La}_{0.9}\text{Sr}_{0.1}\text{Ga}_{0.8}\text{Mg}_{0.2}\text{O}_{3-\delta}$ (10)	$\text{Sr}_2\text{Fe}_{1.5}\text{Mo}_{0.5}\text{O}_{6-\delta}$	700	880	[191]
$\text{La}_{0.9}\text{Sr}_{0.1}\text{Ga}_{0.8}\text{Mg}_{0.2}\text{O}_{2.85}$	$\text{Ce}_{0.8}\text{Gd}_{0.2}\text{O}_{2-\delta} / \text{La}_{0.9}\text{Sr}_{0.1}\text{Ga}_{0.8}\text{Mg}_{0.2}\text{O}_{3-\delta}$ (320)/ $\text{Ce}_{0.8}\text{Gd}_{0.2}\text{O}_{1.9}$	$\text{La}_{0.9}\text{Sr}_{0.1}\text{Ga}_{0.8}\text{Mg}_{0.2}\text{O}_{3-\delta}$	800	500	[192]
$\text{Pr}_{0.6}\text{Sr}_{0.4}\text{Fe}_{0.8}\text{Ni}_{0.2}\text{O}_{3-\delta}$	$\text{La}_{0.8}\text{Sr}_{0.2}\text{Ga}_{0.8}\text{Mg}_{0.2}\text{O}_{3-\delta}$ (520)	$\text{Pr}_{0.6}\text{Sr}_{0.4}\text{Fe}_{0.8}\text{Ni}_{0.2}\text{O}_{3-\delta}$	800	540	[193]
$\text{PrBaMn}_{1.5}\text{Fe}_{0.5}\text{O}_{5+\delta}$	$\text{La}_{0.82}\text{Sr}_{0.18}\text{Ga}_{0.83}\text{Mg}_{0.17}\text{O}_{3-\delta}$ (300)	$\text{PrBaMn}_{1.5}\text{Fe}_{0.5}\text{O}_{5+\delta}$	800	540	[193]
$\text{La}_{0.5}\text{Sr}_{0.5}\text{Fe}_{0.9}\text{Nb}_{0.1}\text{O}_{3-\delta}$	$\text{Ce}_{0.8}\text{Sm}_{0.2}\text{O}_{2-\delta} / \text{La}_{0.9}\text{Sr}_{0.1}\text{Ga}_{0.8}\text{Mg}_{0.2}\text{O}_{3-\delta}$ (200)/ $\text{Ce}_{0.8}\text{Sm}_{0.2}\text{O}_{1.9}$	$\text{La}_{0.5}\text{Sr}_{0.5}\text{Fe}_{0.9}\text{Nb}_{0.1}\text{O}_{3-\delta}$	750	630	[194]
$\text{La}_{0.54}\text{Sr}_{0.36}\text{Co}_{0.2}\text{Fe}_{0.6}\text{Nb}_{0.2}\text{O}_{3-\delta}$	$\text{Ce}_{0.8}\text{Sm}_{0.2}\text{O}_{2-\delta} / \text{La}_{0.9}\text{Sr}_{0.1}\text{Ga}_{0.8}\text{Mg}_{0.2}\text{O}_{3-\delta}$ (200)/ $\text{Ce}_{0.8}\text{Sm}_{0.2}\text{O}_{1.9}$	$\text{La}_{0.54}\text{Sr}_{0.36}\text{Co}_{0.2}\text{Fe}_{0.6}\text{Nb}_{0.2}\text{O}_{3-\delta}$	800	539	[195]
$\text{Sr}_2\text{TiFe}_{0.9}\text{Mo}_{0.1}\text{O}_{6-\delta}$	$\text{La}_{0.8}\text{Sr}_{0.2}\text{Ga}_{0.83}\text{Mg}_{0.17}\text{O}_{3-\delta}$ (243)	$\text{Sr}_2\text{TiFe}_{0.9}\text{Mo}_{0.1}\text{O}_{6-\delta}$	800	444	[196]
$\text{Sr}_2\text{Fe}_{1.4}\text{Nb}_{0.1}\text{Mo}_{0.5}\text{O}_{6-\delta}$	$\text{Ce}_{0.6}\text{La}_{0.4}\text{O}_{2-\delta} / \text{La}_{0.8}\text{Sr}_{0.2}\text{Ga}_{0.83}\text{Mg}_{0.17}\text{O}_{3-\delta}$ (300)	$\text{Sr}_2\text{Fe}_{1.4}\text{Nb}_{0.1}\text{Mo}_{0.5}\text{O}_{6-\delta}$	800	531	[197]
$\text{Sr}_{0.95}\text{Ti}_{0.3}\text{Fe}_{0.63}\text{Ni}_{0.07}\text{O}_{3-\delta}$		$\text{La}_{0.65}\text{Sr}_{0.4}\text{Co}_{0.2}\text{Fe}_{0.8}\text{O}_{3-\delta}$ - $\text{Gd}_{0.1}\text{Ce}_{0.9}\text{O}_{2-\delta}$	800	1000	[172]

Considering the details in Figure A3, one can see that the SOFCs' power density tends to increase with a decrease in the electrolyte's thickness (due to a corresponding decline in the ohmic resistance) despite the existence/absence of CeO_2 -based buffer layers. Nevertheless, the performance of the compared SOFCs varies greatly, even for close electrolyte thicknesses, indicating that other functional components (cermets, oxygen electrodes) have a significant effect on the achievable output characteristics.

A diagram of a typical LSGM-supported cell with a barrier layer between the anode and the electrolyte, using a $\text{Ni-Fe/Ce}_{0.6}\text{La}_{0.4}\text{O}_{2-\delta} / \text{La}_{0.9}\text{Sr}_{0.1}\text{Ga}_{0.8}\text{Mg}_{0.2}\text{O}_{3-\delta} / \text{Sm}_{0.5}\text{Sr}_{0.5}\text{O}_{3-\delta}$ cell, is presented in Figure 8a. In [171], it was shown that the OCV values were equal to 1.07 and 1.15 V at 800 $^{\circ}\text{C}$ and 700 $^{\circ}\text{C}$, respectively, and there was no significant difference in the thickness of the $\text{Ce}_{0.6}\text{La}_{0.4}\text{O}_{1.8}$ interlayer. This LSGM-supported cell yielded up to 2200 and 1350 mW cm^{-2} at 850 and 800 $^{\circ}\text{C}$, respectively. The typical I - V curve and power densities at different temperatures for the LSGM-supported cell are shown in Figure 8b, which is based on the $\text{Ni-Ce}_{0.8}\text{Gd}_{0.2}\text{O}_{2-\delta} / \text{Ce}_{0.8}\text{Gd}_{0.2}\text{O}_{2-\delta} / (\text{La}_{0.9}\text{Sr}_{0.1})_{0.97}\text{Ga}_{0.9}\text{Mg}_{0.1}\text{O}_{3-\delta} / \text{La}_{0.6}\text{Sr}_{0.4}\text{Fe}_{0.8}\text{Co}_{0.2}\text{O}_{3-\delta}$ cell tested in [170]. The maximum power density of the aforementioned cell reached 540 mW cm^{-2} at 800 $^{\circ}\text{C}$, while the maximum power density of a cell containing a $\text{La}_{0.9}\text{Sr}_{0.1}\text{Ga}_{0.9}\text{Mg}_{0.1}\text{O}_{2.9}$ electrolyte reached 450 mW cm^{-2} at 800 $^{\circ}\text{C}$. The electrode polarization resistance values of the $\text{La}_{0.9}\text{Sr}_{0.1}\text{Ga}_{0.9}\text{Mg}_{0.1}\text{O}_{3-\delta}$ and $(\text{La}_{0.9}\text{Sr}_{0.1})_{0.97}\text{Ga}_{0.9}\text{Mg}_{0.1}\text{O}_{3-\delta}$ based cells were equal to 0.34 and 0.30 Ωcm^2 at 800 $^{\circ}\text{C}$, respectively.

Table 3 shows that, for electrode-supported SOFCs with thin-film LSGM electrolytes, a barrier layer between the electrolyte and the electrodes is not necessary [174–176,184,185]. An anode-supported cell containing a $\text{La}_{0.9}\text{Sr}_{0.1}\text{Ga}_{0.8}\text{Mg}_{0.2}\text{O}_{3-\delta}$ film deposited on an anode supported substrate using radio-frequency magnetron sputtering was fabricated in [174]. The anode substrate was composed of a $\text{Ni-Sm}_{0.2}\text{Ce}_{0.8}\text{O}_{2-\delta}$ functional layer and a Ni collector layer; an LSGM- $\text{La}_{0.6}\text{Sr}_{0.4}\text{Co}_{0.2}\text{Fe}_{0.8}\text{O}_{3-\delta}$ composite layer was used as a cathode. The obtained SOFC revealed no cracking, delamination or discontinuity, as shown in Figure 8c. The polarization resistance of an anode-supported cell containing a $\text{La}_{0.9}\text{Sr}_{0.1}\text{Ga}_{0.8}\text{Mg}_{0.2}\text{O}_{3-\delta}$ film decreased from 0.41 to 0.05 Ωcm^2 as the temperature increased from 600 to 800 $^{\circ}\text{C}$. The OCV and P_{max} values were in the range of 0.85–0.95 V and 650–1420 mW cm^{-2} , respectively, at a temperature range of 600–750 $^{\circ}\text{C}$.

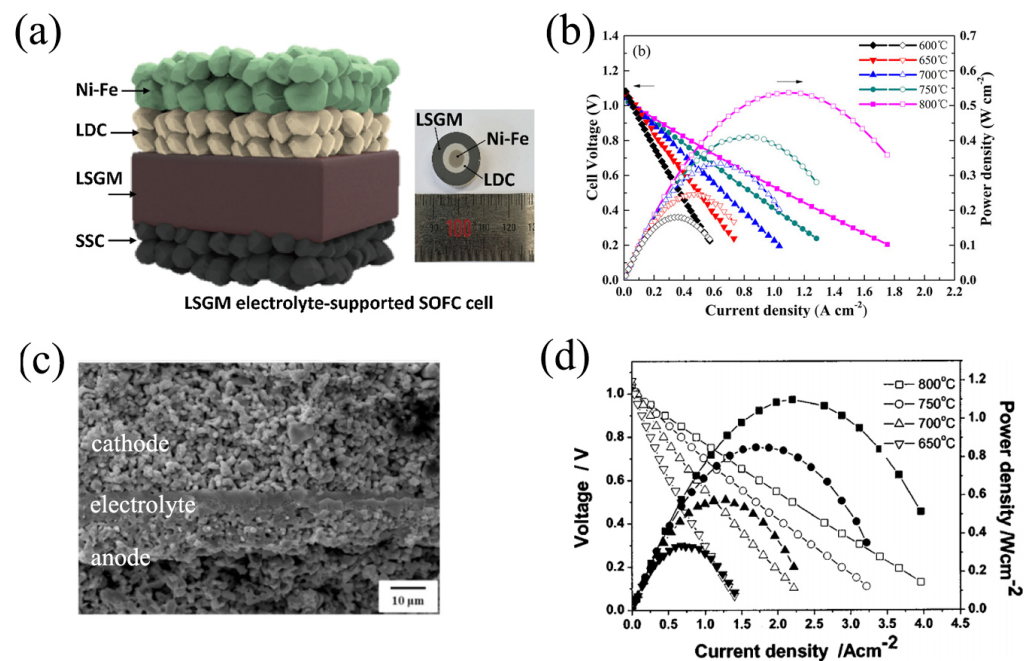


Figure 8. Design and performances of LaGaO₃-based SOFCs: (a) schematic illustration of Ni-Fe/Ce_{0.6}La_{0.4}O_{2-δ}/La_{0.9}Sr_{0.1}Ga_{0.8}Mg_{0.2}O_{3-δ}/Sm_{0.5}Sr_{0.5}O_{3-δ}. Reproduced from [171] with permission from Elsevier Ltd., 2021; (b) *I*-*V* and power density curves of the electrolyte-supported cell with an LSGM electrolyte at different temperatures. Reproduced from [170] with permission from John Wiley & Sons, Inc., 2018; (c) SEM micrograph of an anode-supported cell with an LSGM electrolyte. Reproduced from [174] with permission from Elsevier Ltd., 2002; (d) *I*-*V* and power density curves of an anode-supported cell with a Ce_{0.6}La_{0.4}O_{1.8}-LSGM bi-layered electrolyte at different temperatures. Reproduced from [178] with permission from The Electrochemical Society, 2004.

Combining the two approaches for SOFC design can be found in [178–181]. Bi et al. deposited a Ce_{0.6}La_{0.4}O_{2-δ}/LSGM bi-layer film on a Ni-Ce_{0.9}Gd_{0.1}O_{2-δ} anode. Therefore, the cell design allowed for high OCVs (1.02 and 1.043 V at 800 °C) and high power density values (1100 and 1565 mW cm⁻² at 800 °C) to be achieved at a LDC/LSGM bi-layer thickness of 100 and 65 μm, respectively [178,179]. The *I*-*V* and power density curves for a Ni-Ce_{0.6}La_{0.4}O_{2-δ}/Ce_{0.6}La_{0.4}O_{2-δ}/LSGM(100 μm)/La_{0.9}Sr_{0.1}O_{3-δ}-Ce_{0.55}La_{0.45}O_{2-δ} cell at different temperatures, are shown in Figure 8d [178]. Ju et al. [181] reached a paramount performance of 1790 mW cm⁻² at 700 °C for a SOFC based on an LSGM film with a thickness of 6 μm: this used an SDC buffer layer with a thickness of 500 nm, which was deposited on a Ni-Fe porous anode support. After a thermal cycle going from 700 to 25 °C, the fabricated cell showed an OCV of 1.1 V and *P*_{max} of 1620 mW cm⁻², which was almost the same as the first cycles.

According to a number of investigations [179,182,183,198], the most effective design for SOFCs composed of barrier layers is the LDC/LSGM/LDC tri-layered electrolyte. Bi et al. reported [179] that an anode-supported SOFC with an LDC/LSGM/LDC tri-layered electrolyte film significantly increased when using a cell with an LDC/LSGM bi-layered electrolyte film with the same thickness [178]. Guo et al. [183], depositing an LDC/LSGM/LDC tri-layer with thickness of 30 μm on a Ni-Ce_{0.8}Sm_{0.2}O_{2-δ} anode, fabricated a cell with a 75 mL min⁻¹ H₂ flow rate that generated 1230 W cm⁻² at 800 °C. The specific ohmic resistance across the LDC/LSGM/LDC tri-layer electrolyte film was measured to be equal to 0.086 Ω cm² at 800 °C. The obtained data showed that the polarization resistance was higher than the ohmic resistance at temperatures below 700 °C. A long-term stability experiment was performed on the aforementioned cell with a current density of 1000 mA cm⁻² and a 30 mL min⁻¹ H₂ flow rate at 800 °C. The results of 95 h-test demonstrated that the maximum power density values decreased from 1.08 to 0.81 W cm⁻².

The authors of [183] suggest that there was little diffusion of the transition metal from the electrodes to the electrolyte during the test.

Serious efforts have been made to replace traditional cermet anodes with single-phase oxide materials: this is in an attempt to avoid chemical interactions. Complex oxides with double perovskite ($\text{Sr}_2\text{MMoO}_{6-\delta}$ ($M = \text{Mg, Ti, Ni, Fe}$) [160,162,167,168,186,187,191,196]), layered [190,193] and perovskite [172,189] structures were successfully tested as alternative anode materials for SOFCs with LSGM electrolytes. A buffer layer of doped ceria was used to avoid chemical interactions between an LSGM electrolyte and double perovskites [160,167,168], as well as between an LSGM electrolyte and an oxide cathode [163,187,199]. The composite electrodes $\text{Sr}_2\text{Fe}_{1.5}\text{Mo}_{0.5}\text{O}_{6-\delta}$ - $\text{La}_{0.9}\text{Sr}_{0.1}\text{Ga}_{0.8}\text{Mg}_{0.2}\text{O}_{3-\delta}$ [191], $\text{Sr}_2\text{CoMoO}_{6-\delta}$ - $\text{La}_{0.9}\text{Sr}_{0.1}\text{Ga}_{0.8}\text{Mg}_{0.2}\text{O}_{3-\delta}$ and $\text{Sr}_2\text{Co}_{0.9}\text{Mn}_{0.1}\text{NbO}_{6-\delta}$ - $\text{La}_{0.9}\text{Sr}_{0.1}\text{Ga}_{0.8}\text{Mg}_{0.2}\text{O}_{3-\delta}$ [200] have been proposed to solve the thermo-mechanical incompatibility between an electrolyte and an electrode due to a mismatch in the materials' thermal expansion [174,182–184,191,200–203].

An analysis of recent studies illustrates that LSGM can be used as a base matrix for the formation of both composite electrodes and new composite electrolytes [200,204–210]. Xu et al. [200] fabricated a cell based on a $\text{La}_{0.9}\text{Sr}_{0.1}\text{Ga}_{0.8}\text{Mg}_{0.2}\text{O}_{3-\delta}$ - $\text{Ce}_{0.8}\text{Gd}_{0.2}\text{O}_{1.9}$ electrolyte, with $\text{Sr}_2\text{CoMoO}_{6-\delta}$ - $\text{La}_{0.9}\text{Sr}_{0.1}\text{Ga}_{0.8}\text{Mg}_{0.2}\text{O}_{3-\delta}$ as the anode and $\text{Sr}_2\text{Co}_{0.9}\text{Mn}_{0.1}\text{NbO}_{6-\delta}$ - $\text{La}_{0.9}\text{Sr}_{0.1}\text{Ga}_{0.8}\text{Mg}_{0.2}\text{O}_{3-\delta}$ as the cathode. For this cell, obtained with a 95 wt.% $\text{La}_{0.9}\text{Sr}_{0.1}\text{Ga}_{0.8}\text{Mg}_{0.2}\text{O}_{3-\delta}$ -5 wt.% $\text{Ce}_{0.8}\text{Gd}_{0.2}\text{O}_{2-\delta}$ electrolyte, the OCV, P_{\max} and current density values at 800 °C were equal to 1.08 V, 192 mW cm^{-2} , and 720 mA cm^{-2} , respectively [200].

The electrochemical investigations in [211–215] for LSGM-based SOFCs confirm that these cells can operate in both fuel cell and electrolysis cell modes. Reversible cells were fabricated in [215] with NiO-YSZ-substrate as an anode, $\text{La}_{0.9}\text{Sr}_{0.1}\text{Ga}_{0.8}\text{Mg}_{0.2}\text{O}_{3-\delta}$ film as an electrolyte and $\text{Sm}_{0.5}\text{Sr}_{0.5}\text{CoO}_{3-\delta}$ as an air electrode. It was established that the infiltration of cerium nitrate into the substrate was an effective means of increasing cell performance. The maximum power density of this cell at 3 M Ce nitrate infiltration achieved 950 mW cm^{-2} at 600 °C.

4. Conclusions

Complex oxides based on LaGaO_3 offer a convenient basis for the design of oxygen-conducting electrolytes that can be employed in intermediate-temperature solid oxide fuel cells (SOFCs). A rational combination of appropriate dopants incorporated at various sublattices of LaGaO_3 allows superior transport properties to be achieved for co-doped derivatives ($\text{La}_{1-x}\text{Sr}_x\text{Ga}_{1-y}\text{Mg}_y\text{O}_{3-\delta}$, LSGM). LSGM materials are considered one of the most conductive oxygen-ionic electrolytes, enabling a decrease in SOFC operation temperatures by 100–300 °C compared to YSZ-based SOFCs. As a result, very high SOFC performances (from 0.5 to 1.5 W cm^{-2} at 700 °C) were reported for lab-type electrochemical cells. However, to efficiently place laboratory studies on a manufacturing scale, several issues remain, including the development of simple and low-cost technologies for electrolyte preparation (including thin-film forms), searching for strategies to improve the chemical stability of LSGM with other SOFC components (especially with nickel) and the design of new electrochemically active electrodes. In this regard, the present review serves as the starting point for further research in fields such as solid-state chemistry, physical chemistry, electrochemistry and the technology of LaGaO_3 -based materials and electrochemical cells.

Author Contributions: Conceptualization, E.F. and D.M.; investigation, E.F. and D.M.; writing—original draft preparation, E.F. and D.M.; writing—review and editing, E.F. and D.M.; visualization, E.F. and D.M.; project administration, E.F.; funding acquisition, D.M. All authors have read and agreed to the published version of the manuscript.

Funding: This research was funded by to the Ministry of Education and Science of the Russian Federation, contract no. 075-03-2021-051/5.

Data Availability Statement: Not applicable.

Conflicts of Interest: The authors declare no conflict of interest.

Appendix A

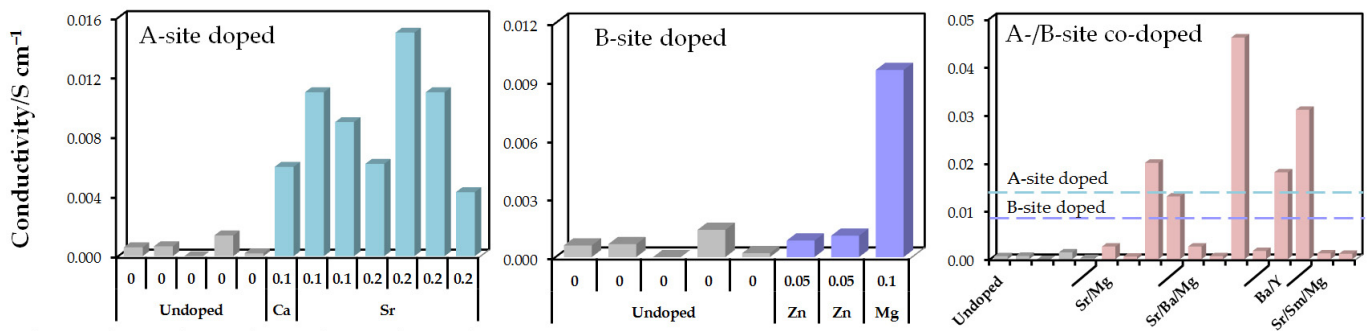


Figure A1. Total conductivity of the LaAlO₃ ceramic materials at 700–900 °C depending on doping strategies. These data are taken from Table 1.

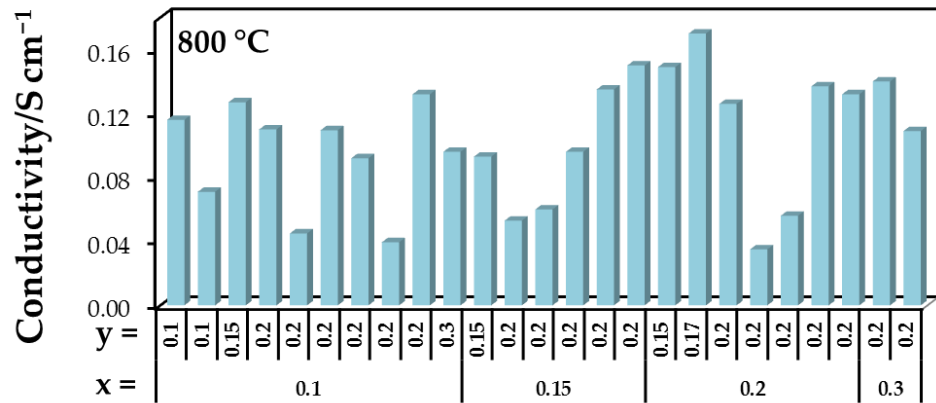


Figure A2. Total conductivity of the La_{1-x}Sr_xGa_{1-y}Mg_yO_{3-δ} ceramic materials at 800 °C. These data are taken from Table 2.

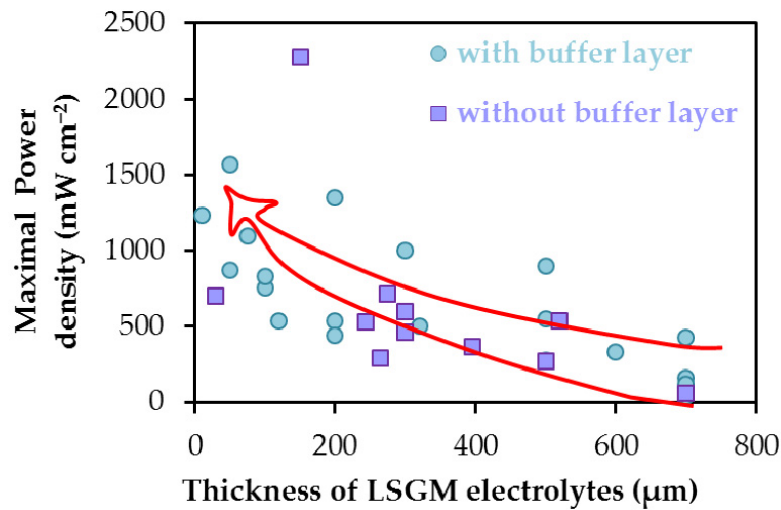


Figure A3. Maximum power densities of SOFCs based on the LSGM-based electrolytes at 800 °C. These data are taken from Table 3.

References

1. Holden, E.; Linnerud, K.; Rygg, B.J. A review of dominant sustainable energy narratives. *Renew. Sustain. Energy Rev.* **2021**, *144*, 110955. [\[CrossRef\]](#)
2. Chu, W.; Calise, F.; Duić, N.; Østergaard, P.A.; Vicidomini, M.; Wang, Q. Recent advances in technology, strategy and application of sustainable energy systems. *Energies* **2020**, *13*, 5229. [\[CrossRef\]](#)
3. Østergaard, P.A.; Duic, N.; Noorollahi, Y.; Mikulcic, H.; Kalogirou, S. Sustainable development using renewable energy technology. *Renew. Energy* **2020**, *146*, 2430–2437. [\[CrossRef\]](#)
4. Kolosok, S.; Bilan, Y.; Vasylieva, T.; Wojciechowski, A.; Morawski, M. A scoping review of renewable energy, sustainability and the environment. *Energies* **2021**, *14*, 4490. [\[CrossRef\]](#)
5. Erixno, O.; Rahim, N.A.; Ramadhani, F.; Adzman, N.N. Energy management of renewable energy-based combined heat and power systems: A review. *Sustain. Energy Technol. Assess.* **2022**, *51*, 101944. [\[CrossRef\]](#)
6. Martínez, M.L.; Vázquez, G.; Pérez-Maqueo, O.; Silva, R.; Moreno-Casasola, P.; Mendoza-González, G.; López-Portillo, J.; MacGregor-Fors, I.; Heckel, G.; Hernández-Santana, J.R.; et al. A systemic view of potential environmental impacts of ocean energy production. *Renew. Sustain. Energy Rev.* **2021**, *149*, 111332. [\[CrossRef\]](#)
7. Pradhan, S.; Chakraborty, R.; Mandal, D.K.; Barman, A.; Bose, P. Design and performance analysis of solar chimney power plant (SCPP): A review. *Sustain. Energy Technol. Assess.* **2021**, *47*, 101411. [\[CrossRef\]](#)
8. Nazir, M.S.; Ali, N.; Bilal, M.; Iqbal, H.M.N. Potential environmental impacts of wind energy development: A global perspective. *Curr. Opin. Environ. Sci. Health.* **2020**, *13*, 85–90. [\[CrossRef\]](#)
9. Soltani, M.; Moradi Kashkooli, F.; Souri, M.; Rafiei, B.; Jabarifar, M.; Gharali, K.; Nathwani, J.S. Environmental, economic, and social impacts of geothermal energy systems. *Renew. Sustain. Energy Rev.* **2021**, *140*, 110750. [\[CrossRef\]](#)
10. Yuan, X.; Su, C.-W.; Umar, M.; Shao, X.; Lobont, O.-R. The race to zero emissions: Can renewable energy be the path to carbon neutrality? *J. Environ. Manag.* **2022**, *308*, 114648. [\[CrossRef\]](#)
11. Tomkins, P.; Müller, T.E. Evaluating the carbon inventory, carbon fluxes and carbon cycles for a long-term sustainable world. *Green Chem.* **2019**, *21*, 3994–4013. [\[CrossRef\]](#)
12. Nurdiawati, A.; Urban, F. Towards deep decarbonisation of energy-intensive industries: A review of current status, technologies and policies. *Energies* **2021**, *14*, 2408. [\[CrossRef\]](#)
13. Bolatkhan, K.; Kossalbayev, B.D.; Zayadan, B.K.; Tomo, T.; Veziroglu, T.N.; Allakhverdiev, S.I. Hydrogen production from phototrophic microorganisms: Reality and perspectives. *Int. J. Hydrogen Energy* **2019**, *44*, 5799–5811. [\[CrossRef\]](#)
14. Barba, F.J.; Gavahian, M.; Es, I.; Zhu, Z.; Chemat, F.; Lorenzo, J.M.; Mousavi Khaneghah, A. Solar radiation as a prospective energy source for green and economic processes in the food industry: From waste biomass valorization to dehydration, cooking, and baking. *J. Clean. Prod.* **2019**, *220*, 1121–1130. [\[CrossRef\]](#)
15. Wijayasekera, S.C.; Hewage, K.; Siddiqui, O.; Hettiaratchi, P.; Sadiq, R. Waste-to-hydrogen technologies: A critical review of techno-economic and socio-environmental sustainability. *Int. J. Hydrogen Energy* **2022**, *47*, 5842–5870. [\[CrossRef\]](#)
16. Testoni, R.; Bersano, A.; Segantin, S. Review of nuclear microreactors: Status, potentialities and challenges. *Prog. Nucl. Energy* **2021**, *138*, 103822. [\[CrossRef\]](#)
17. Timmer, M.A.G.; De Blok, K.; Van Der Meer, T.H. Review on the conversion of thermoacoustic power into electricity. *J. Acoustic. Soc. Am.* **2018**, *143*, 841–857. [\[CrossRef\]](#)
18. Selvan, K.V.; Hasan, M.N.; Mohamed Ali, M.S. Methodological reviews and analyses on the emerging research trends and progresses of thermoelectric generators. *Int. J. Energy Res.* **2019**, *43*, 113–140. [\[CrossRef\]](#)
19. Cigolotti, V.; Genovese, M.; Fragiaco, P. Comprehensive review on fuel cell technology for stationary applications as sustainable and efficient poly-generation energy systems. *Energies* **2021**, *14*, 4963. [\[CrossRef\]](#)
20. Mishra, P.; Saravanan, P.; Packirisamy, G.; Jang, M.; Wang, C. A subtle review on the challenges of photocatalytic fuel cell for sustainable power production. *Int. J. Hydrogen Energy* **2021**, *46*, 22877–22906. [\[CrossRef\]](#)
21. Minh, N.Q. Solid oxide fuel cell technology-features and applications. *Solid State Ion.* **2004**, *174*, 271–277. [\[CrossRef\]](#)
22. Bilal Hanif, M.; Motola, M.; Qayyum, S.; Rauf, S.; Khalid, A.; Li, C.-J.; Li, C.-X. Recent advancements, doping strategies and the future perspective of perovskite-based solid oxide fuel cells for energy conversion. *Chem. Engin. J.* **2022**, *428*, 132603. [\[CrossRef\]](#)
23. Peng, J.; Huang, J.; Wu, X.-L.; Xu, Y.-W.; Chen, H.; Li, X. Solid oxide fuel cell (SOFC) performance evaluation, fault diagnosis and health control: A review. *J. Power Sources* **2021**, *505*, 230058. [\[CrossRef\]](#)
24. Zarabi Golkhatmi, S.; Asghar, M.I.; Lund, P.D. A review on solid oxide fuel cell durability: Latest progress, mechanisms, and study tools. *Renew. Sustain. Energy Rev.* **2022**, *161*, 112339. [\[CrossRef\]](#)
25. Jacobson, A.J. Materials for solid oxide fuel cells. *Chem. Mater.* **2010**, *22*, 660–674. [\[CrossRef\]](#)
26. Saadabadi, S.A.; Thallam Thattai, A.; Fan, L.; Lindeboom, R.E.F.; Spanjers, H.; Aravind, P.V. Solid oxide fuel cells fuelled with biogas: Potential and constraints. *Renew. Energy* **2019**, *134*, 194–214. [\[CrossRef\]](#)
27. Yang, B.C.; Koo, J.; Shin, J.W.; Go, D.; Shim, J.H.; An, J. Direct alcohol-fueled low-temperature solid oxide fuel cells: A review. *Energy Technol.* **2019**, *7*, 5–19. [\[CrossRef\]](#)
28. Zhang, L.; Chen, G.; Dai, R.; Lv, X.; Yang, D.; Geng, S. A review of the chemical compatibility between oxide electrodes and electrolytes in solid oxide fuel cells. *J. Power Sources* **2021**, *492*, 229630. [\[CrossRef\]](#)
29. Brandon, N.P.; Skinner, S.; Steele, B.C.H. Recent advances in materials for fuel cells. *Ann. Rev. Mater. Res.* **2003**, *33*, 182–213. [\[CrossRef\]](#)

30. Zhou, Z.; Nadimpalli, V.K.; Pedersen, D.B.; Esposito, V. Degradation mechanisms of metal-supported solid oxide cells and countermeasures: A review. *Materials* **2021**, *14*, 3139. [[CrossRef](#)]
31. Sreedhar, I.; Agarwal, B.; Goyal, P.; Agarwal, A. An overview of degradation in solid oxide fuel cells-potential clean power sources. *J. Solid State Electrochem.* **2020**, *24*, 1239–1270. [[CrossRef](#)]
32. Yang, Z.; Guo, M.; Wang, N.; Ma, C.; Wang, J.; Han, M. A short review of cathode poisoning and corrosion in solid oxide fuel cell. *Int. J. Hydrogen Energy* **2017**, *42*, 24948–24959. [[CrossRef](#)]
33. Zakaria, Z.; Abu Hassan, S.H.; Shaari, N.; Yahaya, A.Z.; Boon Kar, Y. A review on recent status and challenges of yttria stabilized zirconia modification to lowering the temperature of solid oxide fuel cells operation. *Int. J. Energy Res.* **2020**, *44*, 631–650. [[CrossRef](#)]
34. Hanif, M.B.; Rauf, S.; Motola, M.; Babar, Z.U.D.; Li, C.-J.; Li, C.-X. Recent progress of perovskite-based electrolyte materials for solid oxide fuel cells and performance optimizing strategies for energy storage applications. *Mat. Res. Bull.* **2022**, *146*, 111612. [[CrossRef](#)]
35. Atkinson, A.; Sun, B. Residual stress and thermal cycling of planar solid oxide fuel cells. *Mater. Sci. Technol.* **2007**, *23*, 1135–1143. [[CrossRef](#)]
36. Brett, D.J.L.; Atkinson, A.; Brandon, N.P.; Skinner, S.J. Intermediate temperature solid oxide fuel cells. *Chem. Soc. Rev.* **2008**, *37*, 1568–1578. [[CrossRef](#)]
37. Tarancón, A. Strategies for lowering solid oxide fuel cells operating temperature. *Energies* **2009**, *2*, 1130–1150. [[CrossRef](#)]
38. Kilner, J.A.; Burriel, M. Materials for intermediate-temperature solid-oxide fuel cells. *Ann. Rev. Mater. Res.* **2014**, *44*, 365–393. [[CrossRef](#)]
39. Yang, D.; Chen, G.; Zhang, L.; Chen, Z.; Zhang, R.; Asghar, M.I.; Lund, P.D. Low temperature ceramic fuel cells employing lithium compounds: A review. *J. Power Sources* **2021**, *503*, 230070. [[CrossRef](#)]
40. Su, H.; Hu, Y.H. Progress in low-temperature solid oxide fuel cells with hydrocarbon fuels. *Chem. Eng. J.* **2020**, *402*, 126235. [[CrossRef](#)]
41. Kharton, V.V.; Marques, F.M.B.; Atkinson, A. Transport properties of solid oxide electrolyte ceramics: A brief review. *Solid State Ion.* **2004**, *174*, 135–149. [[CrossRef](#)]
42. Mahato, N.; Banerjee, A.; Gupta, A.; Omar, S.; Balani, K. Progress in material selection for solid oxide fuel cell technology: A review. *Prog. Mater. Sci.* **2015**, *72*, 141–331. [[CrossRef](#)]
43. Wang, F.; Lyu, Y.; Chu, D.; Jin, Z.; Zhang, G.; Wang, D. The electrolyte materials for SOFCs of low-intermediate temperature: Review. *Mater. Sci. Technol.* **2019**, *35*, 1551–1562. [[CrossRef](#)]
44. Shi, H.; Su, C.; Ran, R.; Cao, J.; Shao, Z. Electrolyte materials for intermediate-temperature solid oxide fuel cells. *Prog. Nat. Sci. Mater. Int.* **2020**, *30*, 764–774. [[CrossRef](#)]
45. Abdalla, A.M.; Hossain, S.; Azad, A.T.; Petra, P.M.I.; Begum, F.; Eriksson, S.G.; Azad, A.K. Nanomaterials for solid oxide fuel cells: A review. *Renew. Sustain. Energy Rev.* **2018**, *82*, 353–368. [[CrossRef](#)]
46. Fan, L.; Zhu, B.; Su, P.-C.; He, C. Nanomaterials and technologies for low temperature solid oxide fuel cells: Recent advances, challenges and opportunities. *Nano Energy* **2018**, *45*, 148–176. [[CrossRef](#)]
47. Ellingsen, L.A.W.; Hung, C.R.; Bettez, G.M.; Singh, B.; Chen, Z.; Whittingham, M.S.; Strømman, A.H. Nanotechnology for environmentally sustainable electromobility. *Nat. Nanotechnol.* **2016**, *11*, 1039–1051. [[CrossRef](#)]
48. Zhigachev, A.O.; Rodaev, V.V.; Zhigacheva, D.V.; Lyskov, N.V.; Shchukina, M.A. Doping of scandia-stabilized zirconia electrolytes for intermediate-temperature solid oxide fuel cell: A review. *Ceram. Int.* **2021**, *47*, 32490–32504. [[CrossRef](#)]
49. Kasyanova, A.V.; Rudenko, A.O.; Lyagaeva, Y.G.; Medvedev, D.A. Lanthanum-containing proton-conducting electrolytes with perovskite structures. *Membr. Membr. Technol.* **2021**, *3*, 73–97. [[CrossRef](#)]
50. Artini, C. Crystal chemistry, stability and properties of interlanthanide perovskites: A review. *J. Eur. Ceram. Soc.* **2017**, *37*, 427–440. [[CrossRef](#)]
51. Ishihara, T.; Matsuda, H.; Takita, Y. Doped LaGaO₃ perovskite type oxide as a new oxide ionic conductor. *J. Am. Chem. Soc.* **1994**, *116*, 3801–3803. [[CrossRef](#)]
52. Feng, M.; Goodenough, J.B.; Huang, K.; Milliken, C. Fuel cells with doped lanthanum gallate electrolyte. *J. Power Sources* **1996**, *63*, 47–51. [[CrossRef](#)]
53. Fung, K.Z.; Chen, T.Y. Cathode-supported SOFC using a highly conductive lanthanum aluminate-based electrolyte. *Solid State Ion.* **2011**, *188*, 64–68. [[CrossRef](#)]
54. Kaur, J.; Singh, D.; Dubey, V.; Suryanarayana, N.S.; Parganiha, Y.; Jha, P. Review of the synthesis, characterization, and properties of LaAlO₃ phosphors. *Res. Chem. Intermed.* **2013**, *40*, 2737–2771. [[CrossRef](#)]
55. Rizwan, M.; Gul, S.; Iqbal, T.; Mushtaq, U.; Farooq, M.H.; Farman, M.; Bibi, R.; Ijaz, M. A review on perovskite lanthanum aluminate (LaAlO₃), its properties and applications. *Mat. Res. Express* **2019**, *6*, 112001. [[CrossRef](#)]
56. Morales, M.; Roa, J.J.; Tartaj, J.; Segarra, M. A review of doped lanthanum gallates as electrolytes for intermediate temperature solid oxides fuel cells: From materials processing to electrical and thermo-mechanical properties. *J. Eur. Ceram. Soc.* **2016**, *36*, 1–16. [[CrossRef](#)]
57. Fu, D.; Itoh, M. Ferroelectricity in silver perovskite oxides. In *Ferroelectrics-Material Aspects*; Lallart, M., Ed.; InTech: Houston, TX, USA, 2011; ISBN 978-953-307-332-3. [[CrossRef](#)]

58. Shen, J.X.; Schleife, A.; Janotti, A.; Van de Walle, C.G. Effects of La 5d and 4f states on the electronic and optical properties of LaAlO₃. *Phys. Rev. B* **2016**, *94*, 205203. [CrossRef]
59. Chen, T.Y.; Fung, K.Z. A and B-site substitution of the solid electrolyte LaGaO₃ and LaAlO₃ with the alkaline-earth oxides MgO and SrO. *J. Alloys Compd.* **2004**, *368*, 106–115. [CrossRef]
60. Goldschmidt, V.M. Die Gesetze der Krystallochemie. *Die Nat.* **1926**, *14*, 477–485. [CrossRef]
61. Popova, V.F.; Tugova, E.A.; Zvereva, I.A.; Gusarov, V.V. Phase equilibria in the LaAlO₃-LaSrAlO₄ system. *Glass Phys. Chem.* **2004**, *30*, 564–567. [CrossRef]
62. Egorova, A.V.; Belova, K.G.; Animitsa, I.E.; Morkhova, Y.A.; Kabanov, A.A. Effect of zinc doping on electrical properties of LaAlO₃ perovskite. *Chim. Technol. Acta* **2021**, *8*, 20218103. [CrossRef]
63. Azaiz, A.; Kadari, A.; Alves, N.; Faria, L.O. Influence of carbon doping on the thermoluminescence properties of LaAlO₃ crystal grown by solid state reaction method. *Int. J. Microstruct. Mater. Prop.* **2020**, *15*, 156–167. [CrossRef]
64. Beheshti, M.; Malekfar, R. A novel approach for the synthesis of lanthanum aluminate nanoparticles using thermal shock assisted solid-state method as a microwave absorber layer. *Mater. Chem. Phys.* **2021**, *270*, 124848. [CrossRef]
65. Fabián, M.; Arias-Serrano, B.I.; Yaremchenko, A.A.; Kolev, H.; Kaňuchová, M.; Briančin, J. Ionic and electronic transport in calcium-substituted LaAlO₃ perovskites prepared via mechanochemical route. *J. Eur. Ceram. Soc.* **2019**, *39*, 5298–5308. [CrossRef]
66. Brylewski, T.; Bučko, M.M. Low-temperature synthesis of lanthanum monoaluminate powders using the co-precipitation-calcination technique. *Ceram. Int.* **2013**, *39*, 5667–5674. [CrossRef]
67. Jin, X.; Zhang, L.; Luo, H.; Fan, X.; Jin, L.; Liu, B.; Li, D.; Qiu, Z.; Gan, Y. Preparation of Eu³⁺ doped LaAlO₃ phosphors by coprecipitation-molten salt synthesis. *Integr. Ferroelectr.* **2018**, *188*, 1–11. [CrossRef]
68. Zhang, X.Y.; Zhang, T.; Qi, X.W.; Qi, J.Q.; Sun, G.F.; Chen, H.H.; Zhong, R.X. Preparation and characterization of LaAlO₃ via sol-gel process. *Adv. Mater. Res.* **2013**, *624*, 26–29. [CrossRef]
69. Qin, G.; Huang, X.; Chen, J.; He, Z. Synthesis of Sr and Mg double-doped LaAlO₃ nanopowders via EDTA-glycine combined process. *Powder Technol.* **2013**, *235*, 880–885. [CrossRef]
70. Adak, A.K.; Pramanik, P. Synthesis and characterization of lanthanum aluminate powder at relatively low temperature. *Mater. Lett.* **1997**, *30*, 269–273. [CrossRef]
71. Verma, O.N.; Singh, S.; Singh, V.K.; Najim, M.; Pandey, R.; Singh, P. Influence of Ba doping on the electrical behaviour of La_{0.9}Sr_{0.1}Al_{0.9}Mg_{0.1}O_{3-δ} system for a solid electrolyte. *J. Electron. Mater.* **2021**, *50*, 1010–1021. [CrossRef]
72. Rivera-Montalvo, T.; Morales-Hernandez, A.; Barrera-Angeles, A.A.; Alvarez-Romero, R.; Falcony, C.; Zarate-Medina, J. Modified Pechini's method to prepare LaAlO₃:RE thermoluminescent. *Mater. Radiat. Phys. Chem.* **2017**, *140*, 68–73. [CrossRef]
73. Garcia, A.B.S.; Bispo-Jr, A.G.; Lima, S.A.M.; Pires, A.M. Effects of the Pechini's modified synthetic route on structural and photophysical properties of Eu³⁺ or Tb³⁺-doped LaAlO₃. *Mat. Res. Bull.* **2021**, *143*, 111462. [CrossRef]
74. Silveira, I.S.; Ferreira, N.S.; Souza, D.N. Structural, morphological and vibrational properties of LaAlO₃ nanocrystals produced by four different methods. *Ceram. Int.* **2021**, *47*, 27748–27758. [CrossRef]
75. da Silva, C.A.; de Miranda, P.E.V. Synthesis of LaAlO₃ based materials for potential use as methane-fueled solid oxide fuel cell anodes. *Int. J. Hydrogen Energy* **2015**, *40*, 10002–10015. [CrossRef]
76. Lee, G.; Kim, I.; Yang, I.; Ha, J.-M.; Na, H.B.; Jung, J.C. Effects of the preparation method on the crystallinity and catalytic activity of LaAlO₃ perovskites for oxidative coupling of methane. *Appl. Surf. Sci.* **2018**, *429*, 55–61. [CrossRef]
77. Stathopoulos, V.N.; Kuznetsova, T.; Lapina, O.; Khabibulin, D.; Pandis, P.K.; Krieger, T.; Chesalov, Y.; Gulyalev, R.; Krivensov, V.; Larina, T.; et al. Evolution of bulk and surface structures in stoichiometric LaAlO₃ mixed oxide prepared by using starch as template. *Mater. Chem. Phys.* **2018**, *207*, 423–434. [CrossRef]
78. Lessing, P.A. Mixed-cation oxide powders via polymeric precursors. *Am. Ceram. Soc. Bull.* **1989**, *68*, 1002–1007.
79. Howard, C.J.; Kennedy, B.J.; Chakoumakos, B.C. Neutron powder diffraction study of rhombohedral rare-earth aluminates and the rhombohedral to cubic phase transition. *J. Phys. Condens. Matter* **2000**, *12*, 349–365. [CrossRef]
80. Nguyen, T.L.; Dokiya, M.; Wang, S.; Tagawa, H.; Hashimoto, T. The effect of oxygen vacancy on the oxide ion mobility in LaAlO₃-based oxides. *Solid State Ion.* **2000**, *130*, 229–241. [CrossRef]
81. Park, J.Y.; Park, H.J. High temperature electrical properties of Sr- and Mg-doped LaAlO₃. *J. Korean Cryst. Growth. Cryst. Technol.* **2019**, *29*, 187–191. [CrossRef]
82. Park, J.Y.; Choi, G.M. Electrical conductivity of Sr and Mg doped LaAlO₃. *Solid State Ion.* **2002**, *154–155*, 535–540. [CrossRef]
83. Chen, T.Y.; Fung, K.Z. Comparison of dissolution behavior and ionic conduction between Sr and/or Mg doped LaGaO₃ and LaAlO₃. *J. Power Sources* **2004**, *132*, 1–10. [CrossRef]
84. Fu, Q.X.; Tietz, F.; Lersch, P.; Stöver, D. Evaluation of Sr- and Mn-substituted LaAlO₃ as potential SOFC anode materials. *Solid State Ion.* **2006**, *177*, 1059–1069. [CrossRef]
85. Villas-Boas, L.A.; De Souza, D.P.F. The effect of Pr co-doping on the densification and electrical properties of Sr-LaAlO₃. *Mater. Res.* **2013**, *16*, 982–989. [CrossRef]
86. Verma, O.N.; Jha, P.A.; Melkeri, A.; Singh, P. A comparative study of aqueous tape and pellet of (La_{0.89}Ba_{0.01})Sr_{0.1}Al_{0.9}Mg_{0.1}O_{3-δ} electrolyte material. *Phys. B Condens. Matter* **2017**, *521*, 230–238. [CrossRef]
87. Guo-Heng, Q.; Xiao-Wei, H.; Zh, H.U. Chemical compatibility and electrochemical performance between LaAlO₃-based electrolyte and selected anode materials. *Wuli Huaxue Xuebao/Acta Phys.-Chim. Sin.* **2013**, *29*, 311–318. [CrossRef]

88. Verma, O.N.; Jha, P.A.; Singh, P.; Jha, P.K.; Singh, P. Influence of iso-valent “Sm” double substitution on the ionic conductivity of $\text{La}_{0.9}\text{Sr}_{0.1}\text{Al}_{0.9}\text{Mg}_{0.1}\text{O}_{3-\delta}$ ceramic system. *Mater. Chem. Phys.* **2020**, *241*, 122345. [[CrossRef](#)]
89. Villas-Boas, L.A.; Goulart, C.A.; De Souza, D.P.F. Desenvolvimento microestrutural e mobilidade de ions oxigênio em perovskitas do tipo LaAlO_3 dopadas com Sr, Ba e Ca. *Rev. Mater.* **2020**, *25*, e-12801. [[CrossRef](#)]
90. Villas-Boas, L.A.; Goulart, C.A.; De Souza, D.P.F. Effects of Sr and Mn co-doping on microstructural evolution and electrical properties of LaAlO_3 . *Process. Appl. Ceram.* **2019**, *13*, 333–341. [[CrossRef](#)]
91. Zvonareva, I.; Fu, X.-Z.; Medvedev, D.; Shao, Z. Electrochemistry and energy conversion features of protonic ceramic cells with mixed ionic-electronic electrolytes. *Energy Environ. Sci.* **2022**, *15*, 439–465. [[CrossRef](#)]
92. Tietz, F. Thermal expansion of SOFC materials. *Ionics* **1999**, *5*, 129–139. [[CrossRef](#)]
93. Nguyen, T.L.; Dokiya, M. Electrical conductivity, thermal expansion and reaction of $(\text{La}, \text{Sr})(\text{Ga}, \text{Mg})\text{O}_3$ and $(\text{La}, \text{Sr})\text{AlO}_3$ system. *Solid State Ion.* **2000**, *132*, 217–226. [[CrossRef](#)]
94. Venâncio, S.A.; de Miranda, P.E.V. Direct utilization of carbonaceous fuels in multifunctional SOFC anodes for the electrosynthesis of chemicals or the generation of electricity. *Int. J. Hydrogen Energy* **2017**, *42*, 13927–13938. [[CrossRef](#)]
95. Huang, K.; Tichy, R.S.; Goodenough, J.B. Superior perovskite oxide-ion conductor; strontium- and magnesium-doped LaGaO_3 : I, phase relationships and electrical properties. *J. Am. Ceram. Soc.* **1998**, *81*, 2565–2575. [[CrossRef](#)]
96. Chang, J.; Lee, H.-W.; Kang, S.-J.L. Low-temperature pressureless sintering of Sr- and Mg-doped lanthanum gallate ceramics by sintering atmosphere control. *J. Am. Ceram. Soc.* **2009**, *92*, 927–930. [[CrossRef](#)]
97. Moure, A.; Castro, A.; Tartaj, J.; Moure, C. Single-phase ceramics with $\text{La}_{1-x}\text{Sr}_x\text{Ga}_{1-y}\text{Mg}_y\text{O}_{3-\delta}$ composition from precursors obtained by mechanosynthesis. *J. Power Sources* **2009**, *188*, 489–497. [[CrossRef](#)]
98. Domingues, E.M.; Gonçalves, P.; Figueiredo, F.M. Synthesis of nanopowders of the aluminum-substituted lanthanum gallate solid electrolyte by mechanochemical route. *Solid State Sci.* **2012**, *14*, 820–827. [[CrossRef](#)]
99. Lee, D.; Han, J.-H.; Chun, Y.; Song, R.-H.; Shin, D.R. Preparation and characterization of strontium and magnesium doped lanthanum gallates as the electrolyte for IT-SOFC. *J. Power Sources* **2007**, *166*, 35–40. [[CrossRef](#)]
100. Huang, K.; Goodenough, J.B. Wet chemical synthesis of Sr- and Mg-doped LaGaO_3 , a perovskite-type oxide-ion conductor. *J. Solid State Chem.* **1998**, *136*, 274–283. [[CrossRef](#)]
101. Colomer, M.T.; Kilner, J.A. Ni-doped lanthanum gallate perovskites: Synthesis and structural, microstructural, and electrical characterization. *Solid State Ion.* **2011**, *182*, 76–81. [[CrossRef](#)]
102. Kuncewicz-Kupczyk, W.; Kobertz, D.; Miller, M.; Singheiser, L.; Hilpert, K. Vaporization of Sr- and Mg-doped lanthanum gallate and implications for solid oxide fuel cells. *J. Electrochem. Soc.* **2001**, *148*, E276–E281. [[CrossRef](#)]
103. Cho, P.-S.; Park, S.-Y.; Cho, Y.H.; Kim, S.-J.; Kang, Y.C.; Mori, T.; Lee, J.-H. Preparation of LSGM powders for low temperature sintering. *Solid State Ion.* **2009**, *180*, 788–791. [[CrossRef](#)]
104. Chae, N.S.; Park, K.S.; Yoon, Y.S.; Yoo, I.S.; Kim, J.S.; Yoon, H.H. Sr- and Mg-doped LaGaO_3 powder synthesis by carbonate coprecipitation. *Colloids Surf. A Physicochem. Eng. Asp.* **2008**, *313–314*, 154–157. [[CrossRef](#)]
105. Shi, M.; Xu, Y.; Liu, A.; Liu, N.; Wang, C.; Majewski, P.; Aldinger, F. Synthesis and characterization of Sr- and Mg-doped lanthanum gallate electrolyte materials prepared via the Pechini method. *Mater. Chem. Phys.* **2009**, *114*, 43–46. [[CrossRef](#)]
106. Cong, L.; He, T.; Ji, Y.; Guan, P.; Huang, Y.; Su, W. Synthesis and characterization of IT-electrolyte with perovskite structure $\text{La}_{0.8}\text{Sr}_{0.2}\text{Ga}_{0.85}\text{Mg}_{0.15}\text{O}_{3-\delta}$ by glycine-nitrate combustion method. *J. Alloys Compd.* **2003**, *348*, 325–331. [[CrossRef](#)]
107. Kumar, M.; Nesaraj, A.S.; Raj, I.A.; Pattabiraman, R. Synthesis and characterization of $\text{La}_{0.9}\text{Sr}_{0.1}\text{Ga}_{0.8}\text{Mg}_{0.2}\text{O}_{3-\delta}$ electrolyte for intermediate temperature solid oxide fuel cells (IT SOFC). *Ionics* **2004**, *10*, 93–98. [[CrossRef](#)]
108. Ishikawa, H.; Enoki, M.; Ishihara, T.; Akiyama, T. Combustion synthesis of doped lanthanum gallate as an electrolyte for solid oxide fuel cells. *Mater. Trans.* **2006**, *47*, 149–155. [[CrossRef](#)]
109. Ha, S.B.; Cho, Y.H.; Ji, H.-I.; Lee, J.-H.; Kang, Y.C.; Lee, J.-H. Low-temperature sintering and electrical properties of strontium- and magnesium-doped lanthanum gallate with V_2O_5 additive. *J. Power Sources* **2011**, *196*, 2971–2978. [[CrossRef](#)]
110. Ishikawa, H.; Enoki, M.; Ishihara, T.; Akiyama, T. Self-propagating high-temperature synthesis of $\text{La}(\text{Sr})\text{Ga}(\text{Mg})\text{O}_{3-\delta}$ for electrolyte of solid oxide fuel cells. *J. Alloys Compd.* **2007**, *430*, 246–251. [[CrossRef](#)]
111. Ishikawa, H.; Enoki, M.; Ishihara, T.; Akiyama, T. Mechanically activated self-propagating high-temperature synthesis of $\text{La}_{0.9}\text{Sr}_{0.1}\text{Ga}_{0.8}\text{Mg}_{0.2}\text{O}_{3-\delta}$ as an electrolyte for SOFC. *J. Alloys Compd.* **2009**, *488*, 238–242. [[CrossRef](#)]
112. Jung, D.S.; Koo, H.Y.; Jang, H.C.; Kim, J.H.; Cho, Y.H.; Lee, J.-H.; Kang, Y.C. Firing characteristics of $\text{La}_{0.8}\text{Sr}_{0.2}\text{Ga}_{0.8}\text{Mg}_{0.2}\text{O}_{3-\delta}$ electrolyte powders prepared by spray pyrolysis. *J. Alloys Compd.* **2009**, *487*, 693–697. [[CrossRef](#)]
113. Sammes, N.M.; Tompsett, G.A.; Phillips, R.J.; Cartner, A.M. Characterisation of doped-lanthanum gallates by X-ray diffraction and Raman spectroscopy. *Solid State Ion.* **1998**, *111*, 1–7. [[CrossRef](#)]
114. Yu, J.; Liu, H.; Chen, X.; Xing, J.; Yuan, B.; Wang, M.; Ma, W. Ionic conductivity and crystal structure of LSGM with different element mole ratios. *Fuel Cells* **2021**, *21*, 149–154. [[CrossRef](#)]
115. Batista, R.M.; Reis, S.L.; Muccillo, R.; Muccillo, E.N.S. Sintering evaluation of doped lanthanum gallate based on thermodilatometry. *Ceram. Int.* **2018**, *45*, 5218–5222. [[CrossRef](#)]
116. Lerch, M.; Boysen, H.; Hansen, T. High-temperature neutron scattering investigation of pure and doped lanthanum gallate. *J. Phys. Chem. Solids* **2001**, *62*, 445–455. [[CrossRef](#)]
117. Traina, K.; Henrist, C.; Vertruyen, B.; Cloots, R. Dense $\text{La}_{0.9}\text{Sr}_{0.1}\text{Ga}_{0.8}\text{Mg}_{0.2}\text{O}_{2.85}$ electrolyte for IT-SOFC’s: Sintering study and electrochemical characterization. *J. Alloys Compd.* **2011**, *509*, 1493–1500. [[CrossRef](#)]

118. Biswal, R.C.; Biswas, K. Novel way of phase stability of LSGM and its conductivity enhancement. *Int. J. Hydrogen Energy* **2015**, *40*, 509–518. [[CrossRef](#)]
119. Stevenson, J.W.; Armstrong, R.; McCready, D.E.; Pederson, L.R.; Weber, W.J. Processing and electrical properties of alkaline earth-doped lanthanum gallate. *J. Electrochem. Soc.* **1997**, *144*, 3613–3620. [[CrossRef](#)]
120. Hayashi, H.; Inaba, H.; Matsuyama, M.; Lan, N.G.; Dokiya, M.; Tagawa, H. Structural consideration on the ionic conductivity of perovskite-type oxides. *Solid State Ion.* **1999**, *122*, 1–15. [[CrossRef](#)]
121. Datta, P.; Majewski, P.; Aldinger, F. Thermal expansion behaviour of Sr- and Mg-doped LaGaO₃ solid electrolyte. *J. Eur. Ceram. Soc.* **2009**, *29*, 1463–1468. [[CrossRef](#)]
122. Yu, S.; Bi, H.; Sun, J.; Zhu, L.; Yu, H.; Lu, C.; Liu, X. Effect of grain size on the electrical properties of strontium and magnesium doped lanthanum gallate electrolytes. *J. Alloys Compd.* **2019**, *777*, 244–251. [[CrossRef](#)]
123. Zhang, Q.; Liu, W.J.; Wang, J.; Liu, D.; Sun, Z.H.C. Processing of perovskite La_{0.9}Sr_{0.1}Ga_{0.8}Mg_{0.2}O_{3-δ} electrolyte by glycine-nitrate combustion method. *Int. J. Hydrogen Energy* **2021**, *46*, 31362–31369. [[CrossRef](#)]
124. Liu, N.; Yuan, Y.P.; Majewski, P.; Aldinger, F. Synthesis of La_{0.85}Sr_{0.15}Ga_{0.85}Mg_{0.15}O_{2.85} materials for SOFC applications by acrylamide polymerization. *Mat. Res. Bull.* **2006**, *41*, 461–468. [[CrossRef](#)]
125. Shi, M.; Chen, M.; Zuo, R.; Xu, Y.; Su, H.; Wang, L.; Yu, T. Synthesis and characterization of La_{0.85}Sr_{0.15}Ga_{0.8}Mg_{0.2}O_{2.825} by glycine combustion method and EDTA combustion method. *Powder Technol.* **2010**, *204*, 188–193. [[CrossRef](#)]
126. Morales, M.; Roa, J.J.; Perez-Falcón, J.M.; Moure, A.; Tartaj, J.; Espiell, F.; Segarra, M. Correlation between electrical and mechanical properties in La_{1-x}Sr_xGa_{1-y}Mg_yO_{3-δ} ceramics used as electrolytes for solid oxide fuel cells. *J. Power Sources* **2014**, *246*, 918–925. [[CrossRef](#)]
127. Chen, T.-Y.; Fung, K.-Z. Synthesis of and densification of oxygen-conducting La_{0.8}Sr_{0.2}Ga_{0.8}Mg_{0.2}O_{2.8} nano powder prepared from a low temperature hydrothermal urea precipitation process. *J. Eur. Ceram. Soc.* **2008**, *28*, 803–810. [[CrossRef](#)]
128. Cristiani, C.; Zampori, L.; Latorrata, S.; Pelosato, R.; Dotelli, G.; Ruffo, R. Carbonate coprecipitation synthesis of Sr- and Mg-doped LaGaO₃. *Mater. Lett.* **2009**, *63*, 1892–1894. [[CrossRef](#)]
129. Kaleva, G.M.; Politova, E.D.; Mosunov, A.V.; Sadovskaya, N.V. Modified ion-conducting ceramics based on lanthanum gallate: Synthesis, structure, and properties. *Russ. J. Phys. Chem.* **2018**, *92*, 1138–1144. [[CrossRef](#)]
130. Wang, Y.; Zhou, D.F.; Chen, L.; Xie, S.K.; Liu, X.J.; Meng, J. Improvement in the sintering and electrical properties of strontium- and magnesium-doped lanthanum gallate by MoO₃ dopant. *J. Alloys Compd.* **2017**, *710*, 748–755. [[CrossRef](#)]
131. Ishii, K.; Matsunaga, C.; Munakata, F.; Uchikoshi, T. Effect of A-site ion non-stoichiometry on the chemical stability and electric conductivity of strontium and magnesium-doped lanthanum gallate. *J. Am. Ceram. Soc.* **2019**, *103*, 790–799. [[CrossRef](#)]
132. Wang, L.-S.; Li, C.-X.; Ma, K.; Zhang, S.-L.; Yang, G.-J.; Li, C.-J. Microstructure and electrochemical properties of La_{0.8}Sr_{0.2}Ga_{0.8}Mg_{0.2}O₃ thin film deposited by vacuum cold spray for solid oxide fuel cells. *ECS Trans.* **2017**, *78*, 405–412. [[CrossRef](#)]
133. Zhang, J.; Zhao, Y.; Qiao, J.; Sun, W.; Sun, K.; Wang, Z. An easily controllable flash sintering process for densification of electrolyte for application in solid oxide fuel cells. *Int. J. Hydrogen Energy* **2020**, *45*, 17824–17832. [[CrossRef](#)]
134. Savioli, J.; Watson, G.W. Defect chemistry of LaGaO₃ doped with divalent cations. *Solid State Ion.* **2022**, *374*, 115828. [[CrossRef](#)]
135. Rupp, G.M.; Glowacki, M.; Fleig, J. Electronic and ionic conductivity of La_{0.95}Sr_{0.05}Ga_{0.95}Mg_{0.05}O_{3-δ} (LSGM) single crystals. *J. Electrochem. Soc.* **2016**, *163*, F1189–F1197. [[CrossRef](#)]
136. Mariño, C.; Basbus, J.; Larralde, A.L.; Alonso, J.A.; Fernández-Díaz, M.T.; Troncoso, L. Structural, electrical characterization and oxygen-diffusion paths in LaSrGa_{1-x}Mg_xO_{4-δ} (x = 0.0–0.2) layered perovskites: An impedance spectroscopy and neutron diffraction study. *New J. Chem.* **2021**, *45*, 10248–10256. [[CrossRef](#)]
137. Li, Y.; Yi, H.; Xu, J.; Kuang, X. High oxide ion conductivity in the Bi³⁺ doped melilite LaSrGa₃O₇. *J. Alloys Compd.* **2018**, *740*, 143–147. [[CrossRef](#)]
138. Baskaran, S.; Lewinsohn, C.A.; Chou, Y.-S.; Qian, M.; Stevenson, J.W.; Armstrong, T.R. Mechanical properties of alkaline earth-doped lanthanum gallate. *J. Mater. Sci.* **1999**, *34*, 3913–3922. [[CrossRef](#)]
139. Shkerin, S.N.; Bronin, D.I.; Kovyazina, S.A.; Gorelov, V.P.; Kuzmin, A.V.; Martemyanova, Z.S.; Beresnev, S.M. Structure and phase transitions of (La,Sr)(Ga,Mg)O_{3-α} solid electrolyte. *Solid State Ion.* **2004**, *171*, 129–134. [[CrossRef](#)]
140. Wu, Y.-C.; Rao, C.-R. An investigation on the microstructural and electrical properties of La_{0.85}D_xSr_{0.15-x}Ga_{0.8}Mg_{0.2}O_{2.825} (D = Ba and Ca) electrolytes in solid oxide fuel cells. *Ceram. Int.* **2018**, *44*, 19706–19717. [[CrossRef](#)]
141. Nesaraj, A.S.; Kumar, M.; Arul Raj, I.; Radhakrishna, I.; Pattabiraman, R. Investigations on chemical interactions between alternate cathodes and lanthanum gallate electrolyte for intermediate temperature solid oxide fuel cell (ITSOFC). *J. Iran. Chem. Soc.* **2007**, *4*, 89–106. [[CrossRef](#)]
142. Garcia-Garcia, F.J.; Tang, Y.; Gotor, F.J.; Sayagués, M.J. Development by mechanochemistry of La_{0.8}Sr_{0.2}Ga_{0.8}Mg_{0.2}O_{2.8} electrolyte for SOFCs. *Materials* **2020**, *13*, 1366. [[CrossRef](#)] [[PubMed](#)]
143. Sydyknazar, S.; Cascos, V.; Troncoso, L.; Larralde, A.L.; Fernández-Díaz, M.T.; Alonso, J.A. Design, synthesis, structure and properties of Ba-doped derivatives of SrCo_{0.95}Ru_{0.05}O_{3-δ} perovskite as cathode materials for SOFCs. *Materials* **2019**, *12*, 1957. [[CrossRef](#)] [[PubMed](#)]
144. Zhang, L.; Li, X.; Zhang, L.; Hongdongcai, H.; Xu, J.; Wang, L.; Long, W. Improved thermal expansion and electrochemical performance of La_{0.4}Sr_{0.6}Co_{0.9}Sb_{0.1}O_{3-δ}-Ce_{0.8}Sm_{0.2}O_{1.9} composite cathode for IT-SOFCs. *Solid State Sci.* **2019**, *91*, 126–132. [[CrossRef](#)]

145. Wang, S.; Jin, F.; Li, L.; Li, R.; Qu, B.; He, T. Stability, compatibility and performance improvement of $\text{SrCo}_{0.8}\text{Fe}_{0.1}\text{Nb}_{0.1}\text{O}_{3-\delta}$ perovskite as a cathode for intermediate-temperature solid oxide fuel cells. *Int. J. Hydrogen Energy* **2017**, *42*, 4465–4477. [CrossRef]
146. Yang, X.; Han, X.; He, T.; Du, Y. Enhanced stability of $\text{BaCoO}_{3-\delta}$ using doping process as a cathode material for IT-SOFCs. *ECS Trans.* **2017**, *78*, 543–550. [CrossRef]
147. Niu, B.; Lu, C.; Yi, W.; Luo, S.; Li, X.; Zhong, X.; Zhao, X.; Xu, B. In-situ growth of nanoparticles-decorated double perovskite electrode materials for symmetrical solid oxide cells. *Appl. Catal. B Environ.* **2020**, *270*, 118842. [CrossRef]
148. Tarancón, A.; Peña-Martínez, J.; Marrero-López, D.; Morata, A.; Ruiz-Morales, J.; Núñez, P. Stability, chemical compatibility and electrochemical performance of $\text{GdBaCo}_2\text{O}_{5+x}$ layered perovskite as a cathode for intermediate temperature solid oxide fuel cells. *Solid State Ion.* **2008**, *179*, 2372–2378. [CrossRef]
149. Zhou, Q.; Qu, L.; Zhang, T.; He, Y.; Zhao, C.; Wang, M.; Wei, T.; Zhang, Y. Preparation and electrochemical properties of an La-doped $\text{Pr}_2\text{Ni}_{0.85}\text{Cu}_{0.1}\text{Al}_{0.05}\text{O}_{4+\delta}$ cathode material for an IT-SOFC. *J. Alloys Compd.* **2020**, *824*, 153967. [CrossRef]
150. Chen, T.; Zhou, Y.; Yuan, C.; Liu, M.; Meng, X.; Zhan, Z.; Xia, C.; Wang, S. Impregnated $\text{Nd}_2\text{NiO}_{4+\delta}$ -scandia stabilized zirconia composite cathode for intermediate-temperature solid oxide fuel cells. *J. Power Sources* **2014**, *269*, 812–817. [CrossRef]
151. Pikalova, E.Y.; Medvedev, D.A.; Khasanov, A.F. Structure, stability, and thermomechanical properties of Ca-substituted $\text{Pr}_2\text{NiO}_{4+\delta}$. *Phys. Solid State* **2017**, *59*, 694–702. [CrossRef]
152. Pikalova, E.; Kolchugin, A.; Bogdanovich, N.; Medvedev, D.; Lyagaeva, J.; Vedmid', L.; Ananyev, M.; Plaksin, S.; Farlenkov, A. Suitability of $\text{Pr}_{2-x}\text{Ca}_x\text{NiO}_{4+\delta}$ as cathode materials for electrochemical devices based on oxygen ion and proton conducting solid state electrolytes. *Int. J. Hydrogen Energy* **2020**, *42*, 4465–4477. [CrossRef]
153. Skutina, L.; Filonova, E.; Medvedev, D.; Maignan, A. Undoped Sr_2MMoO_6 double perovskite molybdates (M = Ni, Mg, Fe) as promising anode materials for solid oxide fuel cells. *Materials* **2021**, *14*, 1715. [CrossRef] [PubMed]
154. Zhang, X.; Ohara, S.; Mukai, K.; Fukui, T.; Yoshida, H.; Nishimura, M.; Inagaki, T.; Miura, K. Ni-SDC cermet anode for medium-temperature solid oxide fuel cell with lanthanum gallate electrolyte. *J. Power Sources* **1999**, *83*, 170–177. [CrossRef]
155. Huang, K.; Goodenough, J.B. A solid oxide fuel cell based on Sr- and Mg-doped LaGaO_3 electrolyte: The role of a rare-earth oxide buffer. *J. Alloys Compd.* **2000**, *303–304*, 454–464. [CrossRef]
156. Kim, K.; Kim, B.; Son, J.; Kim, J.; Lee, H.; Lee, J.; Moon, J. Characterization of the electrode and electrolyte interfaces of LSGM-based SOFCs. *Solid State Ion.* **2006**, *177*, 2155–2158. [CrossRef]
157. Eba, H.; Anzai, C.; Ootsuka, S. Observation of cation diffusion and phase formation between solid oxide layers of lanthanum gallate-based fuel cells. *Mater. Trans.* **2018**, *59*, 244–250. [CrossRef]
158. Zhang, X.; Ohara, S.; Okawa, H.; Maric, R.; Fukui, T. Interactions of a $\text{La}_{0.9}\text{Sr}_{0.1}\text{Ga}_{0.8}\text{Mg}_{0.2}\text{O}_{3-\delta}$ electrolyte with Fe_2O_3 , Co_2O_3 and NiO anode materials. *Solid State Ion.* **2001**, *139*, 145–152. [CrossRef]
159. Du, Y.; Sammes, N.M. Interactions and compatibilities of LSGM electrolyte and LSCM anode. *ECS Proc. Vol.* **2005**, *2005–2007*, 1127–1136. [CrossRef]
160. Niu, B.; Jin, F.; Liu, J.; Zhang, Y.; Jiang, P.; Feng, T.; Xu, B.; He, T. Highly carbon- and sulfur-tolerant $\text{Sr}_2\text{TiMoO}_{6-\delta}$ double perovskite anode for solid oxide fuel cells. *Int. J. Hydrogen Energy* **2019**, *44*, 20404–20415. [CrossRef]
161. Dos Santos-Gómez, L.; León-Reina, L.; Porras-Vázquez, J.M.; Losilla, E.R.; Marrero-López, D. Chemical stability and compatibility of double perovskite anode materials for SOFCs. *Solid State Ion.* **2013**, *239*, 1–7. [CrossRef]
162. Filonova, E.A.; Dmitriev, A.S. Physicochemical properties of potential cathode $\text{La}_{1-x}\text{Ba}_x\text{Mn}_{1-y}\text{Cr}_y\text{O}_3$ and anode $\text{Sr}_2\text{NiMoO}_6$ materials for solid-oxide fuel cells. *Eurasian Chem.-Technol. J.* **2012**, *14*, 139–145. [CrossRef]
163. Filonova, E.A.; Gilev, A.R.; Skutina, L.S.; Vylkov, A.I.; Kuznetsov, D.K.; Shur, V.Y. Double $\text{Sr}_2\text{Ni}_{1-x}\text{Mg}_x\text{MoO}_6$ perovskites ($x = 0, 0.25$) as perspective anode materials for LaGaO_3 -based solid oxide fuel cells. *Solid State Ion.* **2018**, *314*, 112–118. [CrossRef]
164. Filonova, E.A.; Dmitriev, A.S.; Pikalov, P.S.; Medvedev, D.A.; Pikalova, E.Y. The structural and electrical properties of $\text{Sr}_2\text{Ni}_{0.75}\text{Mg}_{0.25}\text{MoO}_6$ and its compatibility with solid state electrolytes. *Solid State Ion.* **2014**, *262*, 365–369. [CrossRef]
165. Takano, S.; Shin-mura, K.; Niwa, E.; Hashimoto, T.; Sasaku, K. Chemical compatibility of $\text{Sr}_2\text{MgMoO}_{6-\delta}$ with representative electrolyte materials and interlayer materials for solid oxide fuel cells. *J. Ceram. Soc. Japan* **2018**, *126*, 482–487. [CrossRef]
166. Filonova, E.A.; Dmitriev, A.S. Crystal structure and thermal properties of $\text{Sr}_2\text{ZnMoO}_6$. *Inorg. Mater.* **2014**, *49*, 602–605. [CrossRef]
167. Xie, Z.; Zhao, H.; Du, Z.; Chen, T.; Chen, N. Electrical, chemical, and electrochemical properties of double perovskite oxides $\text{Sr}_2\text{Mg}_{1-x}\text{Ni}_x\text{MoO}_{6-\delta}$ as anode materials for solid oxide fuel cells. *J. Phys. Chem. C* **2014**, *118*, 18853–18860. [CrossRef]
168. Marrero-López, D.; Peña-Martínez, J.; Ruiz-Morales, J.C.; Gabás, M.; Núñez, P.; Aranda, M.A.G.; Ramos-Barrado, J.R. Redox behaviour, chemical compatibility and electrochemical performance of $\text{Sr}_2\text{MgMoO}_{6-\delta}$ as SOFC anode. *Solid State Ion.* **2010**, *180*, 1672–1682. [CrossRef]
169. Kumar, S.; Chakraborty, A.; Kobi, S.; Gopalan, P.; Prasanna, T.R.S. Phase formation between $\text{La}(\text{Sr})\text{Ga}(\text{Mg})\text{O}_3$ and $\text{Ce}(\text{La})\text{O}_2$ for solid oxide fuel cell applications. *J. Amer. Ceram. Soc.* **2022**, *105*, 3625–3635. [CrossRef]
170. Wang, J.Q.; Zhou, D.F.; Gao, J.Q.; Sun, H.R.; Zhu, X.F.; Meng, J. Effect of A/B-Site Non-stoichiometry on the structure and properties of $\text{La}_{0.9}\text{Sr}_{0.1}\text{Ga}_{0.9}\text{Mg}_{0.1}\text{O}_{3-\delta}$ solid electrolyte in intermediate-temperature solid oxide fuel cells. *ChemElectroChem* **2018**, *5*, 665–673. [CrossRef]
171. Hwang, K.-J.; Jang, M.; Kim, M.K.; Lee, S.H.; Shin, T.H. Effective buffer layer thickness of La-doped CeO_2 for high durability and performance on $\text{La}_{0.9}\text{Sr}_{0.1}\text{Ga}_{0.8}\text{Mg}_{0.2}\text{O}_{3-\delta}$ electrolyte supported type solid oxide fuel cells. *J. Eur. Ceram. Soc.* **2021**, *41*, 2674–2681. [CrossRef]

172. Zhu, T.; Troiani, H.E.; Mogni, L.V.; Han, M.; Barnett, S.A. Ni-Substituted Sr(Ti,Fe)O₃ SOFC anodes: Achieving high performance via metal alloy nanoparticle exsolution. *Joule* **2018**, *2*, 478–496. [[CrossRef](#)]
173. Huang, K.; Tichy, R.S.; Goodenough, J.B.; Milliken, C. Superior perovskite oxide-ion conductor; strontium- and magnesium-doped LaGaO₃: III. Performance tests of single ceramic fuel cells. *J. Am. Ceram. Soc.* **1998**, *81*, 2581–2585. [[CrossRef](#)]
174. Fukui, T.; Ohara, S.; Murata, K.; Yoshida, H.; Miura, K.; Inagaki, T. Performance of intermediate temperature solid oxide fuel cells with La(Sr)Ga(Mg)O₃ electrolyte film. *J. Power Sources* **2002**, *106*, 142–145. [[CrossRef](#)]
175. Matsuda, M.; Ohara, O.; Murata, K.; Ohara, S.; Fukui, T.; Miyake, M. Electrophoretic fabrication and cell performance of dense Sr- and Mg-doped LaGaO₃-based electrolyte films. *Electrochem. Solid State Lett.* **2003**, *6*, A140–A143. [[CrossRef](#)]
176. Bozza, F.; Polini, R.; Traversa, E. High performance anode-supported intermediate temperature solid oxide fuel cells (IT-SOFCs) with La_{0.8}Sr_{0.2}Ga_{0.8}Mg_{0.2}O_{3-δ} electrolyte films prepared by electrophoretic deposition. *Electrochem. Commun.* **2009**, *11*, 1680–1683. [[CrossRef](#)]
177. Huang, K.; Wan, J.; Goodenough, J.B. Increasing power density of LSGM-based solid oxide fuel cells using new anode materials. *J. Electrochem. Soc.* **2001**, *148*, A788–A794. [[CrossRef](#)]
178. Bi, Z.; Yi, B.; Wang, Z.; Dong, Y.; Wu, H.; She, Y.; Cheng, M. A high-performance anode-supported SOFC with LDC-LSGM bilayer electrolytes. *Electrochem. Solid State Lett.* **2004**, *7*, A105–A107. [[CrossRef](#)]
179. Bi, Z.; Dong, Y.; Cheng, M.; Yi, B. Behavior of lanthanum-doped ceria and Sr-, Mg-doped LaGaO₃ electrolytes in an anode-supported solid oxide fuel cell with a La_{0.6}Sr_{0.4}CoO₃ cathode. *J. Power Sources* **2006**, *161*, 34–39. [[CrossRef](#)]
180. Wang, W.; Yang, Z.; Wang, H.; Ma, G.; Gao, W.; Zhou, Z. Desirable performance of intermediate-temperature solid oxide fuel cell with an anode-supported La_{0.9}Sr_{0.1}Ga_{0.8}Mg_{0.2}O_{3-δ} electrolyte membrane. *J. Power Sources* **2011**, *196*, 3539–3543. [[CrossRef](#)]
181. Ju, Y.W.; Eto, H.; Inagaki, T.; Ida, S.; Ishihara, T. Preparation of Ni-Fe bimetallic porous anode support for solid oxide fuel cells using LaGaO₃ based electrolyte film with high power density. *J. Power Sources* **2010**, *195*, 6294–6300. [[CrossRef](#)]
182. Lin, Y.B.; Barnett, S.A. Co-firing of anode-supported SOFCs with thin La_{0.9}Sr_{0.1}Ga_{0.8}Mg_{0.2}O_{3-δ} electrolytes. *Electrochem. Solid State Lett.* **2006**, *9*, A285–A288. [[CrossRef](#)]
183. Guo, W.; Liu, J.; Zhang, Y. Electrical and stability performance of anode-supported solid oxide fuel cells with strontium- and magnesium-doped lanthanum gallate thin electrolyte. *Electrochim. Acta* **2008**, *53*, 4420–4427. [[CrossRef](#)]
184. Liu, Y.-X.; Wang, S.-F.; Hsu, Y.-F.; Yeh, W.-Y. Solid oxide fuel cells incorporating doped lanthanum gallate films deposited by radio-frequency magnetron sputtering at various Ar/O₂ ratios and annealing conditions. *Surf. Coat. Technol.* **2018**, *344*, 507–513. [[CrossRef](#)]
185. Wang, Y.-P.; Gao, J.-T.; Li, J.-H.; Li, C.-J.; Li, C.-X. Preparation of bulk-like La_{0.8}Sr_{0.2}Ga_{0.8}Mg_{0.2}O_{3-δ} coatings for porous metal-supported solid oxide fuel cells via plasma spraying at increased particle temperatures. *Int. J. Hydrogen Energy* **2021**, *46*, 32655–32664. [[CrossRef](#)]
186. Wei, T.; Ji, Y.; Meng, X.; Zhang, Y. Sr₂NiMoO_{6-δ} as anode material for LaGaO₃-based solid oxide fuel cell. *Electrochem. Commun.* **2008**, *10*, 1369–1372. [[CrossRef](#)]
187. Gilev, A.R.; Kiselev, E.A.; Cherepanov, V.A. Performance of the lanthanum gallate based solid oxide fuel cells with the La_{2-x}Ca_xNi_{1-y}Fe_yO_{4+δ} cathodes and Sr₂Ni_{0.75}Mg_{0.25}MoO_{6-δ} anode. *Solid State Ion.* **2019**, *339*, 115001. [[CrossRef](#)]
188. Ma, L.; Wang, Y.; Li, W.; Guan, B.; Qi, H.; Tian, H.; Zhou, L.; De Santiago, H.A.; Liu, X. Redox-stable symmetrical solid oxide fuel cells with exceptionally high performance enabled by electrode/electrolyte diffuse interface. *J. Power Sources* **2021**, *488*, 229458. [[CrossRef](#)]
189. Gao, J.; Meng, X.; Luo, T.; Wu, H.; Zhan, Z. Symmetrical solid oxide fuel cells fabricated by phase inversion tape casting with impregnated SrFe_{0.75}Mo_{0.25}O_{3-δ} (SFMO) electrodes. *Int. J. Hydrogen Energy* **2017**, *42*, 18499–18503. [[CrossRef](#)]
190. He, W.; Wu, X.; Dong, F.; Ni, M. A novel layered perovskite electrode for symmetrical solid oxide fuel cells: PrBa(Fe_{0.8}Sc_{0.2})₂O_{5+δ}. *J. Power Sources* **2017**, *363*, 16–19. [[CrossRef](#)]
191. Liu, J.; Lei, Y.; Li, Y.; Gao, J.; Han, D.; Zhan, W.; Huang, F.; Wang, S. Infiltrated Sr₂Fe_{1.5}Mo_{0.5}O₆/La_{0.9}Sr_{0.1}Ga_{0.8}Mg_{0.2}O₃ electrodes towards high performance symmetrical solid oxide fuel cells fabricated by an ultra-fast and time-saving procedure. *Electrochem. Commun.* **2017**, *78*, 6–10. [[CrossRef](#)]
192. Lu, X.; Yang, Y.; Ding, Y.; Chen, Y.; Gu, Q.; Tian, D.; Yu, W.; Lin, B. Mo-doped Pr_{0.6}Sr_{0.4}Fe_{0.8}Ni_{0.2}O_{3-δ} as potential electrodes for intermediate-temperature symmetrical solid oxide fuel cells. *Electrochim. Acta* **2017**, *227*, 33–40. [[CrossRef](#)]
193. Zhao, L.; Chen, K.; Liu, Y.; He, B. A novel layered perovskite as symmetric electrode for direct hydrocarbon solid oxide fuel cells. *J. Power Sources* **2017**, *342*, 313–319. [[CrossRef](#)]
194. Bian, L.; Duan, C.; Wang, L.; Zhu, L.; O’Hayre, R.; Chou, K.-C. Electrochemical performance and stability of La_{0.5}Sr_{0.5}Fe_{0.9}Nb_{0.1}O_{3-δ} symmetric electrode for solid oxide fuel cells. *J. Power Sources* **2018**, *399*, 398–405. [[CrossRef](#)]
195. Niu, B.; Jin, F.; Feng, T.; Zhang, L.; Zhang, Y.; He, T. A-site deficient (La_{0.6}Sr_{0.4})_{1-x}Co_{0.2}Fe_{0.6}Nb_{0.2}O_{3-δ} symmetrical electrode materials for solid oxide fuel cells. *Electrochim. Acta* **2018**, *270*, 174–182. [[CrossRef](#)]
196. Niu, B.; Jin, F.; Zhang, L.; Shen, P.; He, T. Performance of double perovskite symmetrical electrode materials Sr₂TiFe_{1-x}Mo_xO_{6-δ} (x = 0.1, 0.2) for solid oxide fuel cells. *Electrochim. Acta* **2018**, *263*, 217–227. [[CrossRef](#)]
197. Gou, M.; Ren, R.; Sun, W.; Xu, C.; Meng, X.; Wang, Z.; Qiao, J.; Sun, K. Nb-doped Sr₂Fe_{1.5}Mo_{0.5}O_{6-δ} electrode with enhanced stability and electrochemical performance for symmetrical solid oxide fuel cells. *Ceram. Int.* **2019**, *45*, 15696–15704. [[CrossRef](#)]
198. Wu, Y.-C.; Huang, W.-H. Processing improvement and performance analysis of La_{0.85}Sr_{0.15}Ga_{0.8}Mg_{0.2}O_{2.825} electrolyte-supported fuel cells. *Ceram. Int.* **2017**, *43*, S729–S738. [[CrossRef](#)]

199. Gao, K.; Liu, X.; Wang, Z.; Xiong, Y. A $\text{Sm}_{0.2}\text{Ce}_{0.8}\text{O}_{1.9}$ (SDC) interlayer method to prevent the elemental interdiffusion between $\text{Sm}_{0.5}\text{Sr}_{0.5}\text{CoO}_{3-\delta}$ (SSC) cathode and $\text{La}_{0.8}\text{Sr}_{0.2}\text{Ga}_{0.8}\text{Mg}_{0.2}\text{O}_{3-\delta}$ (LSGM) electrolyte. *Int. J. Hydrogen Energy* **2017**, *42*, 19170–19177. [[CrossRef](#)]
200. Xu, S.; Lin, X.; Ge, B.; Ai, D.; Ma, J.; Peng, Z. Microstructure and electrical conductivity of $\text{La}_{0.9}\text{Sr}_{0.1}\text{Ga}_{0.8}\text{Mg}_{0.2}\text{O}_{2.85}\text{-Ce}_{0.8}\text{Gd}_{0.2}\text{O}_{1.9}$ composite electrolytes for SOFCs. *Int. J. Appl. Ceram. Technol.* **2019**, *16*, 108–118. [[CrossRef](#)]
201. Abubaker, O.A.; Singh, K.; Thangadurai, V. Investigating the effect of Cu-doping on the electrochemical properties of perovskite-type $\text{Ba}_{0.5}\text{Sr}_{0.5}\text{Fe}_{1-x}\text{Cu}_x\text{O}_{3-\delta}$ ($0 \leq x \leq 0.20$) cathodes. *J. Power Sources* **2020**, *451*, 227777. [[CrossRef](#)]
202. Hong, G.; Kim, T.W.; Kwak, M.J.; Song, J.; Choi, Y.; Woo, S.-K.; Han, M.H.; Cho, C.H.; Kim, S.-D. Composite electrodes of Ti-doped $\text{SrFeO}_{3-\delta}$ and LSGMZ electrolytes as both the anode and cathode in symmetric solid oxide fuel cells. *J. Alloys Compd.* **2020**, *846*, 156154. [[CrossRef](#)]
203. Lee, S.; Kim, S.; Choi, S.; Shin, J.; Kim, G. A Nano-Structured SOFC Composite cathode prepared via infiltration of $\text{La}_{0.5}\text{Ba}_{0.25}\text{Sr}_{0.25}\text{Co}_{0.8}\text{Fe}_{0.2}\text{O}_{3-\delta}$ into $\text{La}_{0.9}\text{Sr}_{0.1}\text{Ga}_{0.8}\text{Mg}_{0.2}\text{O}_{3-\delta}$ for extended triple-phase boundary area. *J. Electrochem. Soc.* **2019**, *166*, F805–F809. [[CrossRef](#)]
204. Fujimoto, T.G.; Reis, S.L.; dos Santos Muccillo, E.N. Influence of yttria-stabilized zirconia on microstructure and electrical properties of doped lanthanum gallate. *Mater. Res.* **2019**, *22*, 20190043. [[CrossRef](#)]
205. Malik, Y.T.; Noviyanti, A.R.; Syarif, D.G. Lowered sintering temperature on synthesis of $\text{La}_{9.33}\text{Si}_6\text{O}_{26}$ (LSO)– $\text{La}_{0.8}\text{Sr}_{0.2}\text{Ga}_{0.8}\text{Mg}_{0.2}\text{O}_{2.55}$ (LSGM) electrolyte composite and the electrical performance on $\text{La}_{0.7}\text{Ca}_{0.3}\text{MnO}_3$ (LCM) cathode. *J. Kim. Sains Apl.* **2018**, *21*, 205–210. [[CrossRef](#)]
206. Lin, X.P.; Zhong, H.T.; Chen, X.; Ge, B.; Ai, D.S. Preparation and property of LSGM-carbonate composite electrolyte for low temperature solid oxide fuel cell. *Solid State Phenom.* **2018**, *281*, 754–760. [[CrossRef](#)]
207. Wang, S.-F.; Lu, H.-C.; Hsu, Y.-F.; Jasinski, P. High-performance anode-supported solid oxide fuel cells with co-fired $\text{Sm}_{0.2}\text{Ce}_{0.8}\text{O}_{2-\delta}/\text{La}_{0.8}\text{Sr}_{0.2}\text{Ga}_{0.8}\text{Mg}_{0.2}\text{O}_{3-\delta}/\text{Sm}_{0.2}\text{Ce}_{0.8}\text{O}_{2-\delta}$ sandwiched electrolyte. *Int. J. Hydrogen Energy* **2022**, *47*, 5429–5438. [[CrossRef](#)]
208. Noviyanti, A.R.; Malik, Y.T.; Rahayu, I.; Eddy, D.R.; Pratomo, U. Electrochemical properties of $\text{La}_{9.33}\text{Si}_6\text{O}_{26}$ (LSO)– $\text{La}_{0.8}\text{Sr}_{0.2}\text{Ga}_{0.8}\text{Mg}_{0.2}\text{O}_{2.55}$ (LSGM) electrolyte over NiO and $\text{La}_{0.1}\text{Ca}_{0.9}\text{MnO}_3$ (LCM) electrodes. *Mat. Res. Exp.* **2021**, *8*, 115505. [[CrossRef](#)]
209. Pandey, R.; Singh, P.; Singh, A.K.; Singh, P. Polyol-mediated synthesis of $\text{La}_{0.9}\text{Sr}_{0.1}\text{Ga}_{0.8}\text{Mg}_{0.2}\text{O}_{2.85}\text{-Ce}_{0.85}\text{Sm}_{0.15}\text{O}_{1.925}$ composite electrolyte for IT-SOFCs. *Mater. Today Proc.* **2020**, *49*, 3071–3075. [[CrossRef](#)]
210. Chen, L.; Zhou, D.F.; Wang, Y.; Zhu, X.F.; Meng, J. Enhanced sintering of $\text{Ce}_{0.8}\text{Nd}_{0.2}\text{O}_{2-\delta}\text{-La}_{0.8}\text{Sr}_{0.2}\text{Ga}_{0.8}\text{Mg}_{0.2}\text{O}_{3-\delta}$ using CoO as a sintering aid. *Ceram. Int.* **2017**, *43*, 3583–3589. [[CrossRef](#)]
211. Glisenti, A.; Bedon, A.; Carollo, G.; Savaniu, C.; Irvine, J.T.S. Reversible, all-perovskite SOFCs based on La, Sr gallates. *Int. J. Hydrogen Energy* **2020**, *45*, 29155–29165. [[CrossRef](#)]
212. Kwon, Y.; Kang, S.; Bae, J. Development of a $\text{PrBaMn}_2\text{O}_{5+\delta}\text{-La}_{0.8}\text{Sr}_{0.2}\text{Ga}_{0.85}\text{Mg}_{0.15}\text{O}_{3-\delta}$ composite electrode by scaffold infiltration for reversible solid oxide fuel cell applications. *Int. J. Hydrogen Energy* **2020**, *45*, 1748–1758. [[CrossRef](#)]
213. Tan, Z.; Ishihara, T. Reversible operation of tubular type solid oxide fuel cells using LaGaO_3 electrolyte porous layer on dense film prepared by dip-coating method. *J. Electrochem. Soc.* **2017**, *164*, F1690–F1696. [[CrossRef](#)]
214. Tan, Z.; Ishihara, T. Redox stability of tubular solid oxide cell using LaGaO_3 electrolyte film prepared by dip-coating. *ECS Trans.* **2021**, *103*, 1685–1693. [[CrossRef](#)]
215. Tan, Z.; Song, J.T.; Takagaki, A.; Ishihara, T. Infiltration of cerium into a NiO–YSZ tubular substrate for solid oxide reversible cells using a LSGM electrolyte film. *J. Mater. Chem. A* **2021**, *9*, 1530–1540. [[CrossRef](#)]